

1 **Advanced Methods for Analyzing In-Situ Observations of Magnetic Reconnection**

2

3 H. Hasegawa^{1,*}, M.R. Argall², N. Aunai³, R. Bandyopadhyay⁴, N. Bessho^{5,6}, I.J. Cohen⁷,
4 R.E. Denton⁸, J.C. Dorelli⁶, J. Egedal⁹, S.A. Fuselier^{10,11}, P. Garnier¹², V. Génot¹², D.B.
5 Graham^{13,*}, K.J. Hwang¹⁰, Y.V. Khotyaintsev¹³, D.B. Korovinskiy¹⁴, B. Lavraud^{12,23}, Q.
6 Lenouvel¹², T.C. Li⁸, Y.-H. Liu⁸, B. Michotte de Welle³, T.K.M. Nakamura^{14,24}, D.S.
7 Payne¹⁵, S.M. Petrinec¹⁶, Y. Qi¹⁷, A.C. Rager⁶, P.H. Reiff¹⁸, J.M. Schroeder⁹, J.R.
8 Shuster², M.I. Sitnov⁷, G.K. Stephens⁷, M. Swisdak¹⁵, A.M. Tian¹⁹, R.B. Torbert^{20,21}, K.J.
9 Trattner¹⁷, S. Zenitani^{14,22}

10

11 First and corresponding author E-mail: hase@stp.isas.jaxa.jp

12 Second corresponding author E-mail: dgraham@irfu.se

13

14 ¹ Institute of Space and Astronautical Science, Japan Aerospace Exploration Agency,
15 Sagamihara, Kanagawa 252-5210, Japan

16 ² Space Science Center, Institute for the Study of Earth, Oceans, and Space, University of
17 New Hampshire, Durham, NH 03824, USA

18 ³ CNRS, Ecole polytechnique, Sorbonne Université, Université Paris Sud, Observatoire
19 de Paris, Institut Polytechnique de Paris, Université Paris-Saclay, PSL Research
20 University, Laboratoire de Physique des Plasmas, Palaiseau, France

21 ⁴ Department of Astrophysical Sciences, Princeton University, Princeton, NJ 08544, USA

22 ⁵ Department of Astronomy, University of Maryland, College Park, Maryland 20742,
23 USA

24 ⁶ Heliophysics Science Division, NASA Goddard Space Flight Center, Greenbelt,
25 Maryland 20771, USA

26 ⁷ Applied Physics Laboratory, The Johns Hopkins University, Laurel, MD, USA

27 ⁸ Department of Physics and Astronomy, Dartmouth College, Hanover, NH, USA

28 ⁹ Department of Physics, University of Wisconsin-Madison, Madison, Wisconsin 53706,
29 USA

30 ¹⁰ Southwest Research Institute, San Antonio, TX, USA

31 ¹¹ University of Texas at San Antonio, San Antonio, TX, USA

32 ¹² Institut de Recherche en Astrophysique et Planétologie, CNRS, Université Paul
33 Sabatier, CNES, Toulouse, France

34 ¹³ Swedish Institute of Space Physics, Uppsala, Sweden

35 ¹⁴ Space Research Institute, Austrian Academy of Sciences, Graz, Austria

36 ¹⁵ Institute for Research in Electronics and Applied Physics, University of Maryland,

37 College Park, MD, USA
38 ¹⁶ Lockheed Martin ATC, Palo Alto, CA, USA
39 ¹⁷ Laboratory for Atmospheric and Space Physics, University of Colorado, Boulder, CO,
40 USA
41 ¹⁸ Rice Space Institute, Rice University, Houston, Texas, USA
42 ¹⁹ Shandong Key Laboratory of Optical Astronomy and Solar-Terrestrial Environment,
43 School of Space Science and Physics, Institute of Space Sciences, Shandong University,
44 Weihai, Shandong 264209, People's Republic of China
45 ²⁰ Southwest Research Institute, Durham, NH, USA
46 ²¹ Physics Department, University of New Hampshire, Durham, NH, USA
47 ²² Research Center for Urban Safety and Security, Kobe University, Kobe 657-8501,
48 Japan
49 ²³ Laboratoire d'Astrophysique de Bordeaux, Université Bordeaux, CNRS, Pessac,
50 France
51 ²⁴ Krimgen LLC, Hiroshima 732-0828, Japan

52

53 **Abstract**

54 There is ample evidence for magnetic reconnection in the solar system, but it is a
55 nontrivial task to visualize, to determine the proper approaches and frames to study, and
56 in turn to elucidate the physical processes at work in reconnection regions from in-situ
57 measurements of plasma particles and electromagnetic fields. Here an overview is given
58 of a variety of single- and multi-spacecraft data analysis techniques that are key to
59 revealing the context of in-situ observations of magnetic reconnection in space and for
60 detecting and analyzing the diffusion regions where ions and/or electrons are
61 demagnetized. We focus on recent advances in the era of the Magnetospheric Multiscale
62 mission, which has made electron-scale, multi-point measurements of magnetic
63 reconnection in and around Earth's magnetosphere.

64

65 **Keywords:** magnetic reconnection, data analysis techniques, in-situ measurements,
66 magnetosphere, electron diffusion region

67

68 **Contents**

- 69 1 Introduction
70 2 Region and Current Sheet Identification
71 2.1 Automated Burst System
72 2.2 Scientist-in-the-Loop

73	2.3 Ground Loop System
74	2.4 Machine Learning-Based Region Identification
75	2.5 Automated Region Classification Based on 3D Particle Velocity Distributions
76	3 Methods for Context
77	3.1 Large-Scale Context
78	3.1.1 Maximum Magnetic Shear Model
79	3.1.2 Event-Specific Global MHD Modeling
80	3.1.3 Data-Mining Approach to Reconstruction of the Global Reconnection
81	Structure
82	3.1.4 Global 3D Structure of the Magnetosheath using In Situ Measurements:
83	Application to Magnetic Field Draping
84	3.2 Coordinate System, Frame Velocity, and Spacecraft Trajectory Estimation
85	3.2.1 Dimensionality and Coordinate Systems
86	3.2.2 Velocity of the Magnetic Structure
87	3.2.3 Spacecraft Trajectory Estimation
88	3.3 Methods for Reconstructing 2D/3D Structures
89	3.3.1 Field Reconstruction Using Quadratic Expansion
90	3.3.2 3D Empirical Reconstruction Using Stochastic Optimization Method
91	3.3.3 2D Reconstruction of Reconnection Events Assisted by Simulation
92	3.3.4 Grad-Shafranov and Electron Magnetohydrodynamics Reconstruction
93	3.3.5 3D Field Reconstruction Using Modified Radial Basis Functions
94	4 Detection and Analysis of In-Situ Observations of the Diffusion Regions
95	4.1 Diffusion Region Identification
96	4.1.1 Plasma-Frame Dissipation Measure
97	4.1.2 Agyrotropy
98	4.1.3 Pressure-Strain Interaction in Reconnection Diffusion Region
99	4.1.4 Electron Vorticity Indicative of the EDR
100	4.1.5 Magnetic Flux Transport (MFT) Method
101	4.1.6 Electron Diffusion Region Detection with Machine Learning Methods
102	4.1.7 Magnetic Nulls
103	4.2 Analysis Methods for the Electron Diffusion Region
104	4.2.1 Estimation of Anomalous Resistivity, Viscosity, and Diffusion
105	4.2.2 Evaluation of Terms in the Electron Vlasov Equation
106	4.2.3 Non-Maxwellianity
107	4.2.4 Kinetic Entropy
108	4.3 Reconnection Electric Field Estimation

109 4.3.1 Extracting EM from Multiple Crescents in Electron Velocity Distributions
110 4.3.2 Remote Sensing at the Reconnection Separatrix Boundary
111 4.3.3 Separatrix Angle Related to Reconnection Rate
112 5 Summary and Outlook
113 Appendix A The MMS “Quarter Moments” Data Product
114 Acknowledgements
115 Compliance with Ethical Standards
116 References
117 Appendix B Tables summarizing methods (attached at the end)
118

119 1 Introduction

120 Magnetic reconnection in space generally occurs in highly tenuous plasma
121 environments, and hence it has been difficult or almost impossible for remote sensing
122 instruments to take an image of the reconnection region, except for the solar atmosphere
123 and corona for which the column density is sufficiently high (note also an attempt to
124 observe reconnection in Earth’s magnetotail by energetic neutral atom emissions
125 (McComas et al. 2011)). The study of reconnection in space therefore has relied on in-
126 situ measurements by space probes of electromagnetic fields and charged particles
127 (Paschmann et al. 2013). Magnetohydrodynamic (MHD) aspects of reconnection were
128 extensively investigated in 1980s through 1990s by methods based on the MHD theory
129 (Sonnerup et al. 1995; Paschmann and Sonnerup 2008; and references therein).

130 A number of single- and multi-spacecraft data analysis techniques for understanding
131 reconnection and other space phenomena have been developed in the era of ESA’s Cluster
132 mission (e.g., Escoubet et al. 1997), which was launched in 2000 and focused mostly on
133 MHD- and ion-scale processes in and outside the Earth’s magnetosphere (Paschmann et
134 al. 2005). These methods were thoroughly summarized in the literature (Paschmann and
135 Daly 1998, 2008), and thus will not be covered here. The present paper focuses on recent
136 developments since then and on methods specifically for analyzing in-situ measurements
137 of magnetic reconnection in space, and in particular those developed for the state-of-the-
138 art Magnetospheric Multiscale (MMS) mission (Burch et al. 2016a), which has been
139 making electron- or sub-ion-scale (high spatial- and temporal-resolution) measurements
140 of key geospace regions. Applications presented are thus almost exclusively related to in-
141 situ observations of reconnection in and around Earth’s magnetosphere. Nonetheless,
142 many of the methods summarized in this review can be used for the analysis of in-situ
143 measurements in other regions of the solar system, and are possibly applicable to
144 laboratory plasmas.

145 The analysis of a magnetic reconnection event recorded by in-situ measurements may
146 proceed as follows: (1) identification of electric current sheets or localized plasma bulk
147 flows where reconnection may occur, which are intermittent in time series data, (2)
148 understanding the large-scale and local context of the in-situ observations based on
149 upstream solar wind and geomagnetic field conditions, coordinate system estimation, and
150 reconstruction of peripheral plasma and field structures, and (3) detection and analysis of
151 microscopic regions key to the reconnection process, such as the diffusion and energy
152 conversion regions. Therefore, the present paper is organized in the order of such analysis
153 step.

154 We do not intend this paper to be a manual for or an exhaustive review of the methods,
155 such as the books in the Cluster era (Paschmann and Daly 1998, 2008), since this is one
156 of a series of the chapters in a book that summarizes the results from magnetic
157 reconnection studies in the MMS era. Instead, this review presents a range of prior
158 applications of the methods, so that it could be used by the community to decide whether
159 some of the methods is appropriate for their research. For a general overview of magnetic
160 reconnection as a plasma physical process and primary scientific results from the MMS
161 mission, many of which were obtained by use of either of the methods discussed in this
162 review, see Chapter 1 of this issue, Hwang et al. (2023), and Oka et al. (2023).

163 In section 2, an overview is given of methods for identifying plasma regions and
164 current sheets in and around the magnetosphere from in-situ measurements. Section 3
165 presents a variety of methods for both large-scale and local contexts, including estimation
166 of the coordinate system and frame velocity, and reconstruction of multi-dimensional
167 field structures. Section 4 focuses on in-situ data analysis methods to identify and analyze
168 the central region of magnetic reconnection, called the diffusion regions, where ions
169 and/or electrons are demagnetized and the magnetic topology changes. Section 5 gives a
170 brief summary and outlook. In Appendix B we provide, as a quick user guide, tables
171 (Tables 1-7) that summarize for each method (1) required input data, (2) output, (3)
172 fundamental theory, concept, or technique(s) that underlies the method, (4) model or
173 underlying assumption(s), (5) relevant references, etc.

174 Magnetic reconnection inherently involves multi-dimensional structures and often
175 occurs in highly nonuniform environments, as in the case at the magnetopause with
176 substantial jumps across the current sheet in the plasma density, temperature, and
177 magnetic field intensity. Thus, analysis methods assuming a uniform or weakly
178 nonuniform background, such as wave analysis methods (e.g., Narita 2017), are not
179 covered.

180

181 **2 Region and Current Sheet Identification**

182 Each new satellite mission pushes the boundaries of what is known and what is
183 possible, often seeking to study physical processes that have never been directly observed
184 *in situ*. Science teams typically identify regions of interest where the processes are likely
185 to occur, features in the data that highlight the processes, and data triggers to increase the
186 data rate when the processes are thought to occur. Magnetic reconnection is known to
187 occur in thin current sheets often located at transitions between regions, as seen at the
188 dayside magnetopause and in the nightside magnetotail. This has led to the assignment of
189 regions of interest that define where the MMS spacecraft may encounter reconnection,
190 parameters that identify where reconnection is likely to occur, and data management
191 systems [the Automated Burst System (ABS), the Scientist-in-the-Loop (SITL), and the
192 Ground Loop System (GLS)] to capture the right type of data. This section reviews the
193 ways in which MMS locates, identifies, and captures reconnecting current sheets. A few
194 methods based on machine learning for automated identification of regions surrounding
195 the magnetosphere are also reviewed.

196

197 **2.1 Automated Burst System**

198 Prior to MMS, observations of the electron diffusion region (EDR), where electrons
199 are demagnetized and magnetic energy is converted to electron kinetic energy, had been
200 enigmatic, with few direct observations (Nagai et al. 2011, 2013; Scudder et al. 2012;
201 Tang et al. 2013; Oka et al. 2016). This was because spacecraft lacked the spatial and
202 temporal resolution to resolve electron-scale dynamics. MMS has overcome these
203 limitations by having four spacecraft in a tetrahedron configuration at unmatched spatial
204 scales and sampling rates. Since launch, MMS has identified more than 50 EDRs (see
205 Webster et al. (2018), Lenouvel et al. (2021), and Genestreti et al. (2022) for partial lists)
206 and greatly expanded our knowledge of what catalyzes the global reconnection cycle
207 (Chapter 3.1 of this issue; Fuselier et al. 2024). The amount of data required to obtain this
208 success greatly exceeds the downlink allocations of the deep space network, which means
209 that the satellites require an automated way of selecting time intervals for high time
210 resolution burst data downlink, the ABS.

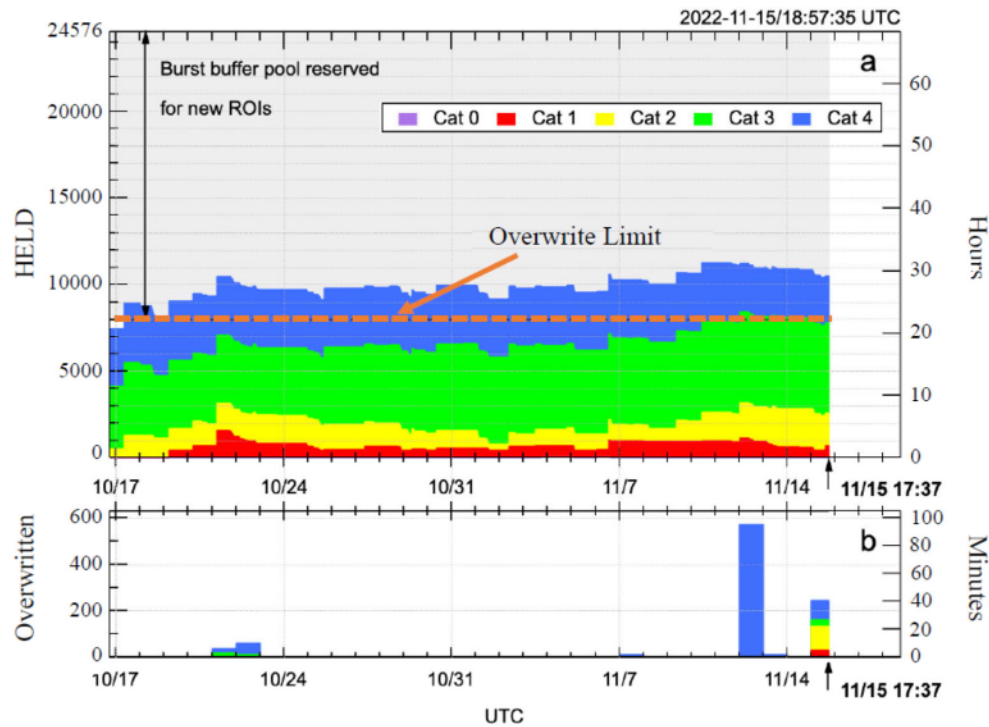
211 Figure 1a shows the amount of burst data held onboard MMS between 17 October
212 and 15 November, 2022. Data is categorized into Category 0 (purple), 1 (red), 2 (yellow),
213 3 (green), and 4 (blue) based on the active science objectives (see Table 1 in Argall et al.
214 (2020) for an example). Category 0 and Category 1 correspond to calibration and primary
215 science data, respectively, while Category 2-4 correspond to lower-priority science goals.
216 The orange dashed line indicates the threshold beyond which data will be overwritten, as

217 the remaining buffers are reserved for new regions of interest. Figure 1b shows the
218 amount of overwritten data in each category. Data classified into the lowest-priority
219 category (Category 4) are overwritten first, unless some memory cleanup activity takes
220 place, as on 15 November 2022. This figure demonstrates that MMS is able to store and
221 downlink all of its highest priority data and effectively manage low-priority data to both
222 achieve tertiary science objectives and make room for new data. Such categorization is
223 important for the burst memory management system to be effective.

224 In an ABS, trigger data numbers (TDNs) are calculated by applying a look-up table
225 of gains G_i and offsets O_i to each measured data quantity x_i to create a scalar value
226 that is a linear combination of the x_i (Baker et al. 2016; Fuselier et al. 2016):

$$227 \quad TDN = \sum_{i=0}^{N-1} G_i x_i + O_i. \quad (1)$$

228 When the TDNs exceed a threshold value, either the data are marked for downlink or the
229 satellite is triggered into burst mode. Missions such as WIND, THEMIS, Cluster,
230 STEREO have burst mode schemes that operate only when triggered. Some WIND and
231 THEMIS triggers used to detect plasma boundaries such as the magnetopause are
232 documented by Phan et al. (2015). Triggers used on STEREO for shock detection, their
233 evolution, and their efficacy are described by Jian et al. (2013). MMS has enough memory
234 to capture burst mode data at all times within its science region of interest. This is so that
235 the Scientist-in-the-Loop has a chance to review the low time resolution data and make
236 their own selections before the unselected burst data is erased from memory. The TDNs
237 are available publicly and the look-up tables of gains and offsets can be updated
238 depending on the active science objectives.



240 **Fig. 1** Burst memory buffers at risk of being overwritten. (a) Amount of Category 0
 241 (purple), 1 (red), 2 (yellow), 3 (green), and 4 (blue) stored or HELD onboard MMS,
 242 shown in terms of the number of burst buffers (left axis) and the corresponding hours of
 243 data (right axis). (b) The amount of overwritten data in terms of Category (color), memory
 244 buffers (left axis) and total time (right axis). Category 0 data are for special operations
 245 (e.g., calibration) or critical science data; selections are rare and are transmitted to ground
 246 as soon as the downlink is available, so no Category 0 buffers are present in the figure.
 247

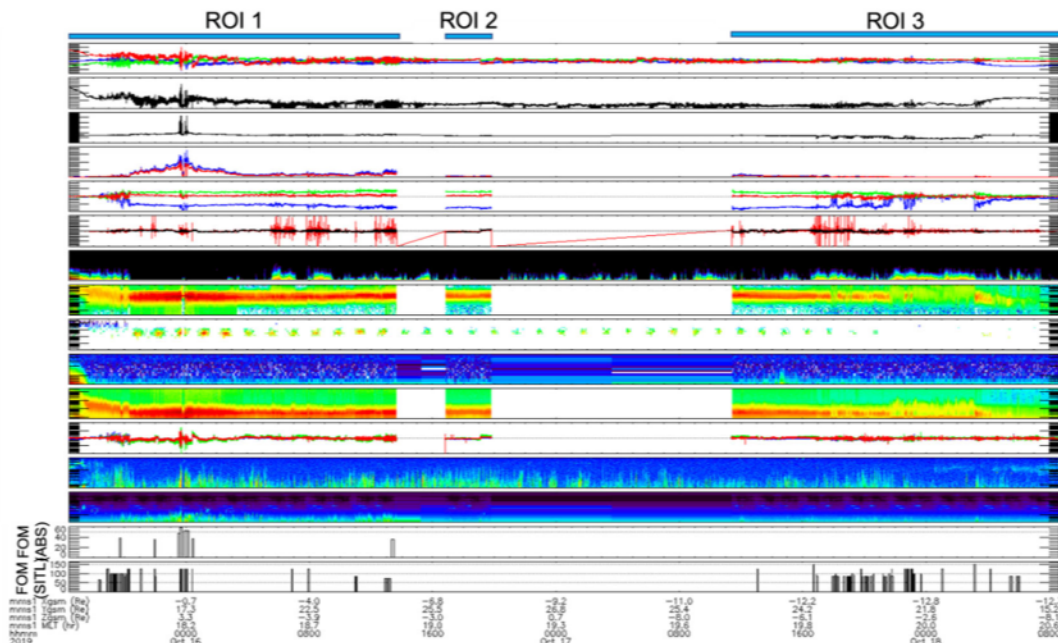
248 2.2 Scientist-in-the-Loop

249 The SITL is a role that is passed among the personnel on the MMS science team. The
 250 SITL scientist is responsible for manually selecting time intervals for burst data downlink
 251 by examining low time resolution data that is recorded simultaneously with the burst data
 252 and is downlinked at the end of each orbit. The SITL is guided by the mission-level
 253 science objectives, which are assigned a priority of 1-4 (Category 1-4) and a range of
 254 Figure-of-Merit values. The SITL assigns a Figure-of-Merit value to time intervals that
 255 fit the science objectives and the corresponding burst data is downlinked in priority-order.

256 Figure 2 shows a typical view of the data that the SITL scientist sees when using an
 257 interactive tool called “EVA” to make burst data selections (see Argall et al. (2020) for
 258 more details). Labels and scales have been removed on purpose except for the bottom two
 259 panels, which show the ABS and SITL selections, respectively. Note that while the SITL

260 scientist selects most of the intervals selected by the ABS, the SITL makes more
261 selections (vertical bars in the bottom panels) – a tedious process that could be alleviated,
262 in part, by automated selection models. This is where the Ground Loop System (GLS)
263 comes into play.

264



265 **Fig. 2** Data that the SITL uses to make selections. The SITL views data from the regions
266 of interest, ROI 1, 2, and 3, as it becomes available, and uses a tool to interact with the
267 plot, make selections, and submit them to the science data center. Quantities and scales
268 are purposefully not shown except for the ABS (second to last panel) and SITL (last panel)
269 selections. Note that while the SITL basically selected the same intervals (vertical bars)
270 as the ABS, the SITL selected many more.

271

272 **2.3 Ground Loop System**

273 The GLS is designed to be a system of machine learning (ML) or empirical models
274 that automate the event classification process using all of the data available to the SITL
275 (much more than what is available to the ABS). Data available to the SITL is of restricted
276 use because its quality is lower than of the science-quality (Level-2) data freely available
277 to the public (Baker et al. 2016). Thus, ML models trained on SITL data may not perform
278 as well when applied to Level-2 data, and vice versa. Argall et al. (2020) implemented
279 the first GLS ML model for automated burst selections. Their model aimed to automate
280 the SITL scientist's top priority – to select magnetopause crossings. Selecting
281 magnetopause crossings was important because EDRs are not resolved in the low-

resolution data available to the SITL; however, EDRs occur in reconnection events at the magnetopause and the magnetopause is easily identifiable in the SITL data.

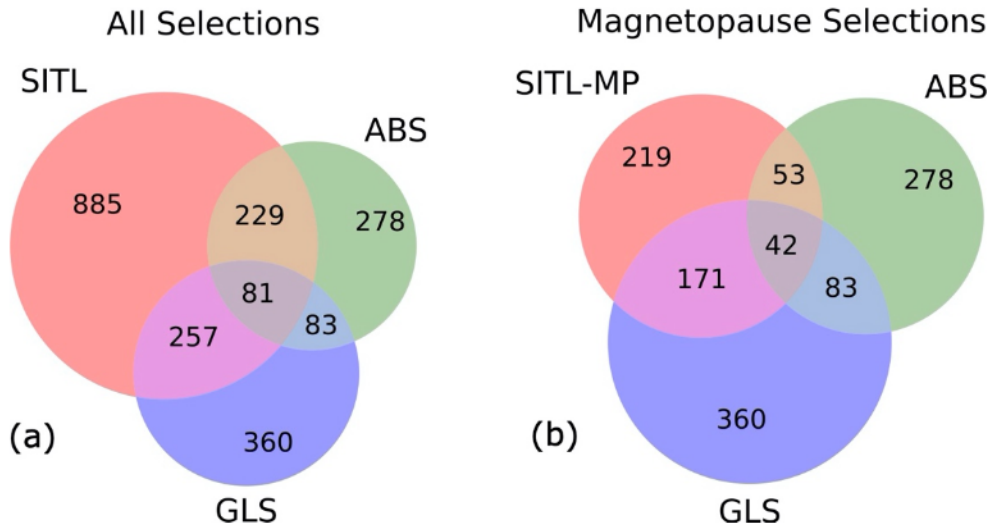


Fig. 3 The GLS and ABS are complementary systems that make selections of high interest to the SITL. (a) Comparison of all selections; the SITL selects a significant number of selections made by both the GLS (71%) and ABS (64%). (b) Comparison of selections designated as magnetopause (MP) crossings by the SITL. In both cases, there is little overlap between the GLS and ABS. Adapted from Argall et al. (2020).

Figure 3a is a Venn diagram showing the overlap of SITL, ABS, and GLS selections using all selections made between 19 October 2019 and 25 March 2020. The SITL selects 71% of all GLS selections and 64% of all ABS selections, indicating that the ABS and GLS are making good selections. Figure 3b is the same format, but includes only those selections that were designated magnetopause crossings by the SITL. The GLS selects 78% ($171/219$) of all magnetopause crossings selected by the SITL. The other 22% of selections include intervals that were magnetopause-like (i.e., flux transfer events, reconnection jets), but were not specifically called magnetopause crossings by the SITL. This indicates that the GLS was effective at what it was designed to do. In both cases, the ABS and GLS had little overlap in selections – they are complementary systems that provide helpful information to the SITL.

The GLS was designed in such a way that new supervised ML models could be trained easily by searching and parsing the human-readable string SITL scientists assign to each of their selections. (A suggestion to future missions that wish to implement a similar system is to have a defined set of keywords to identify similar events.) These ML models could be implemented simultaneously in a hierarchical structure to automate science

307 campaigns (Figure 8 in Argall et al. (2020)). The ground-level for the hierarchical
308 campaigns is to implement region identifiers.

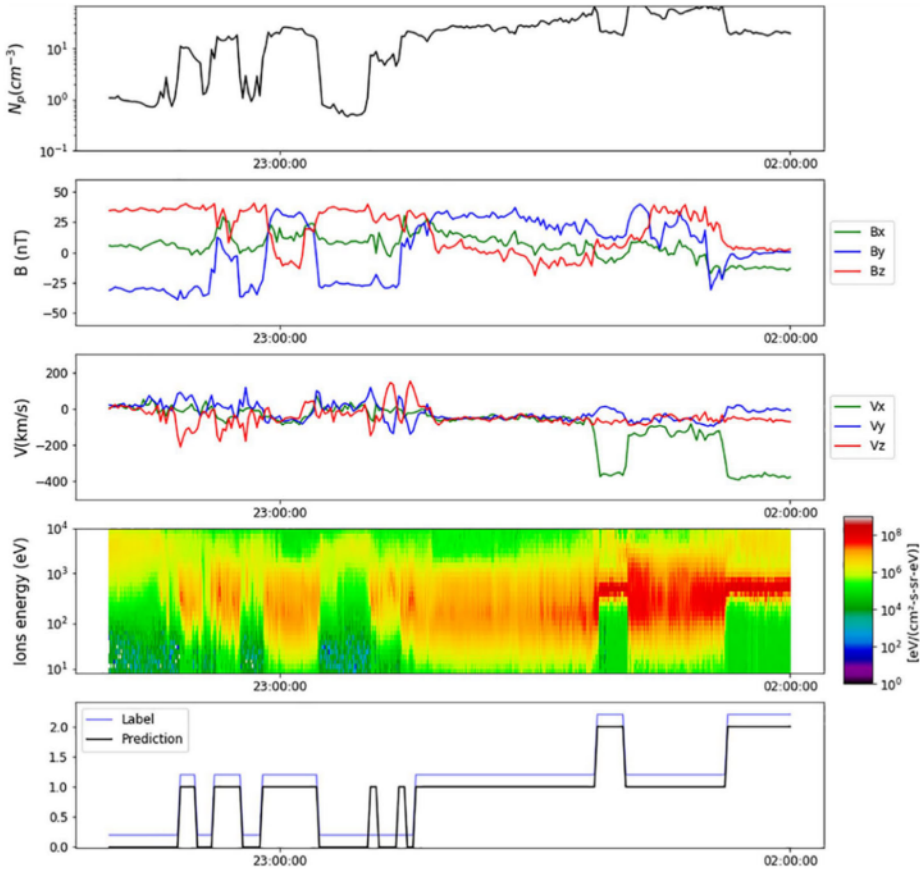
309

310 **2.4 Machine Learning-Based Region Identification**

311 The selection of intervals of interest is first facilitated by the ability to identify key
312 regions of the near-Earth environment. While historically identification of regions and
313 boundaries was done through visual inspection of data, recent work has shown that
314 modern methods relying on ML are very efficient. Novel methods are increasingly needed
315 as the amount of data available nowadays precludes scientists from visually mining
316 numerous and huge datasets accumulated over many different missions, sometimes over
317 decades. Such a method was recently implemented by Nguyen et al. (2022a) and applied
318 to statistical analysis and interpretation of the location and shape of the Earth's
319 magnetopause (Nguyen et al. 2022b,c,d).

320 The identification of three key near-Earth regions, the magnetosphere, the
321 magnetosheath, and the solar wind, was made based on an automatic classification
322 method that uses in situ data (magnetic field and ion moments) from multiple spacecraft.
323 The classification was performed with the so-called Gradient Boosting algorithm
324 (Friedman 2001). While not offering as much flexibility as deep learning methods, this
325 algorithm, based on the iterative fit of the residuals obtained by the successive training
326 and predictions made by decision trees, has been recognized to perform well on complex,
327 eventually imbalanced classification problems (Brown and Mues 2012). Furthermore, it
328 typically needs much less labeled data and is much lighter to train than deep neural
329 networks. The prediction of the algorithm is shown to outperform routines based on
330 manually set thresholds. Data from 11 different spacecraft (THEMIS, ARTEMIS, Cluster,
331 one Double Star (TC-1), and one MMS spacecraft) were analyzed for a total of 83
332 cumulated years. A total of 15,062 magnetopause crossings and 17,227 bow shock
333 crossings were identified. An example automated identification is illustrated in Figure 4
334 for an outbound orbit of the MMS mission. It highlights excellent agreement between
335 label data and the method identification of the main regions and boundaries during this
336 pass. The code is available online (Table 1 in Appendix B) and the datasets can easily be
337 enhanced for future use by the community.

338



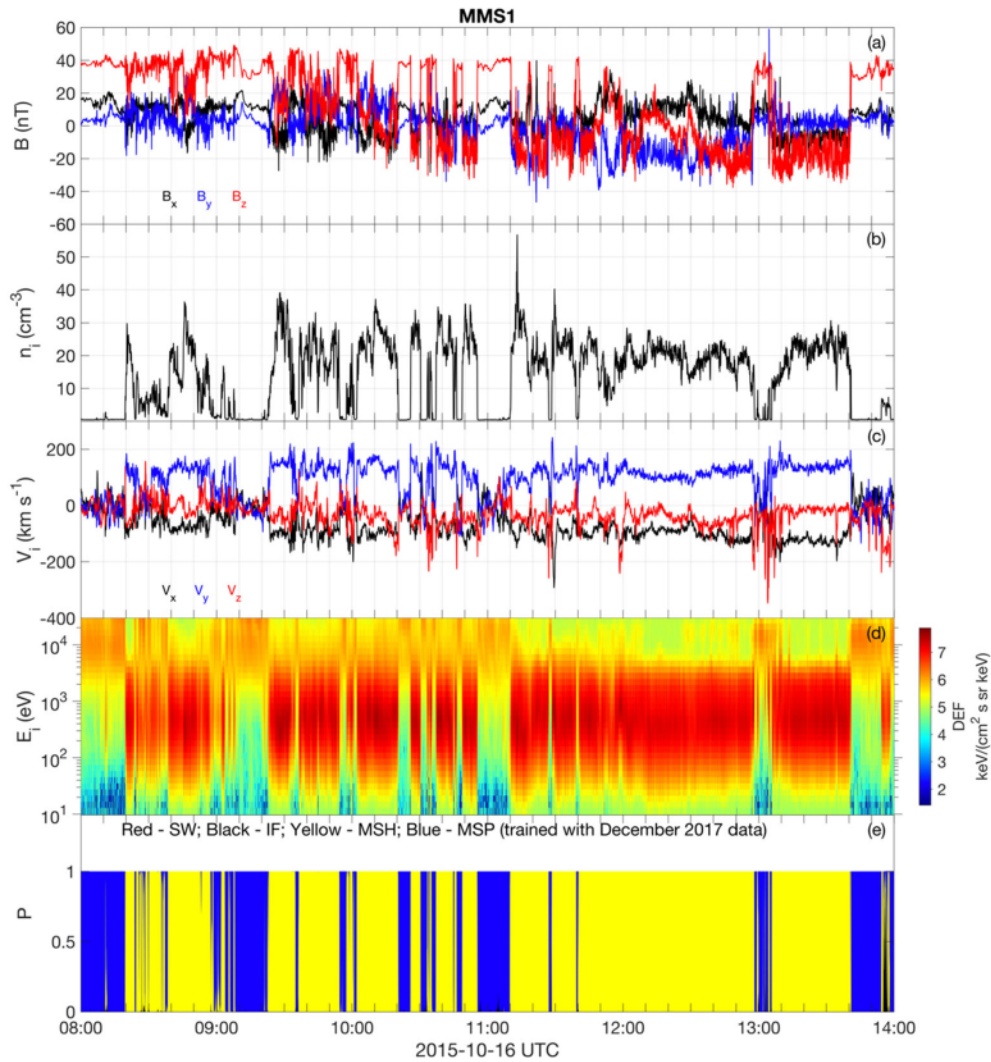
339
 340 **Fig. 4** MMS observations on 31 December 2015 (adapted from Nguyen et al. (2022a)).
 341 The top to fourth panels show the ion density, magnetic field, ion velocity in geocentric
 342 solar magnetospheric (GSM) coordinates, and omnidirectional differential energy fluxes
 343 of ions. The bottom panel shows the evolution of the label (blue), intentionally shifted for
 344 visual inspection, and the prediction made by the ML algorithm (black), in which “0”
 345 means the magnetosphere, “1” the magnetosheath, and “2” the solar wind.
 346

347 **2.5 Automated Region Classification Based on 3D Particle Velocity Distributions**

348 Vast amounts of data produced by space missions make it difficult for scientists to
 349 identify interesting events manually, and automatic data classification methods can be
 350 convenient. Below we describe one approach that allows us to classify three-dimensional
 351 (3D) ion energy distribution samples according to the plasma regions (Olshevsky et al.
 352 2021). The classified data can then be used for statistical studies and identifying
 353 boundaries, such as bow shocks and the magnetopause, where reconnection may occur.
 354 We will focus on the dayside magnetosphere and will define the following regions: solar
 355 wind (SW), ion foreshock (IF), magnetosheath (MSH), and magnetosphere (MSP), all of
 356 which have a distinct signature in ion velocity distribution functions (VDFs). A training
 357 dataset representing “clean” samples (i.e., excluding boundaries) of the ion distributions

358 was selected from the above four regions, and was used to train a convolutional neural
 359 network classifier (Maturana and Scherer 2015) by a supervised ML approach. The
 360 classifier is then applied to ion distributions (other than the training dataset) and assigns
 361 a probability of each distribution belonging to one of the four classes.

362



363

364 **Fig. 5** Example of plasma region classification of MMS data on 16 October 2015. The
 365 panels from top to bottom show (a) the magnetic field, (b) plasma density, (c) ion velocity,
 366 (d) ion energy spectrum, and (e) the probabilities provided by the classifier.

367

368 To illustrate the method, we show in Figure 5 MMS observations during a 6-hour
 369 interval on 16 October 2015 that contains multiple magnetopause crossings (transitions
 370 between MSH and MSP). The crossing at 13:06 UT contains an encounter with the EDR
 371 at the site of magnetic reconnection (Burch et al., 2016b). The MSP intervals are

characterized by the northward magnetic field (B_z dominant), low density and plasma flow, and increased ion flux at energies above 10 keV. The MSH intervals are, on the contrary, characterized by high density, fast plasma flow ($V_y \sim 150$ km/s), and ion flux peaking at ~ 0.3 keV. The bottom panel shows the results of the neural network classifier; one can see that both the MSP (blue) and MSH (yellow) regions have been correctly classified except for boundary layers between the two regions.

Plasma regions can be identified using plasma moments and electromagnetic fields, as illustrated above and in several other ML approaches including the one introduced in section 2.4 (Nguyen et al. 2022a; Cheng et al. 2022). However, ion VDFs contain more information than the moments of the distribution, having a unique footprint for each plasma region and thus possibly improving the reliability of classification. Trained scientists use plots of ion data for visual region classification. As it is difficult to visualize the time series of 3D VDFs, they would normally reduce the full 3D measurements in some way, for example, to omni-directional energy-time spectrograms (e.g., Figure 5d) where all look directions are summed up.

Another helpful representation is the angle-angle (azimuth-polar angle) plots of phase space densities (PSDs) for a specific energy channel. The approach to the classification by Olshevsky et al. (2021), in its essence, is based on image recognition of such plots. One recognizes each of specific footprints in such images corresponding to different regions. During a human inspection, only a small number of energies can generally be analyzed simultaneously. ML has no such limitation, and can analyze all the data simultaneously. Thus, a 3D image recognition is performed, in which a data cube composed of a stack of 32 (number of energy channels for MMS Fast Plasma Investigation (FPI) Dual Ion Spectrometers (DIS) (Pollock et al. 2016)) angle-angle plots is analyzed. This approach is enabled by the homogeneous dataset provided by DIS in fast mode, i.e., the numbers of angular bins and the energy ranges are fixed (except for the special solar wind mode), and thus there is no need to reduce or resample the data.

The results for classification can be used in many different ways. One use is to define times when MMS is in a particular plasma region, for example, in a pristine magnetosheath (e.g., Svennsson et al. 2023). Another use is to analyze the probabilities' time series to identify the boundaries between the different plasma regions. For example, by analyzing the transition between the SW/IF and MSH, Lalti et al. (2022) identified ~ 3000 bow shock crossings by MMS. Similarly, magnetopause crossings can be identified from the transitions between the MSH and MSP classes. Another potential application is to use the probabilities (Figure 5e) to quantify plasma mixing in boundary layers, which, for example, can occur in Kelvin-Helmholtz vortices (Settino et al. 2022).

408 As a final remark, we note that the method as described is based solely on the
409 classification of individual ion VDFs, and can be further extended to ingest the
410 information on time evolution and/or other data (e.g., magnetic field, spacecraft position,
411 etc.), which can enable an even more robust classification.

412

413 **3 Methods for Context**

414 Reconnection regions on kinetic scales (of order 1-500 km) are much smaller than the
415 size of the geospace or the magnetosphere (of order 10^5 km) and are localized in space
416 and often in time. It is thus important to understand a large-scale context and boundary
417 conditions of in-situ observations by spacecraft of reconnection-related phenomena and
418 the geometry and structures around the observing spacecraft. This section gives an
419 overview of methods for revealing such contexts.

420 **3.1 Large-Scale Context**

421 **3.1.1 Maximum Magnetic Shear Model**

422 The maximum magnetic shear model can predict the location on an empirical model
423 magnetopause where the magnetic shear across the magnetopause current sheet is large
424 or maximized, which is a plausible location of magnetopause reconnection, for
425 interplanetary magnetic field (IMF) and geomagnetic dipole tilt conditions given as input
426 (Trattner et al. 2021 and references therein). It was originally developed as a product of a
427 polar cusp study using data from the NASA Polar satellite. The study determined the
428 dayside magnetopause reconnection location (Trattner et al. 2007) for southward IMF
429 conditions by using time-of-flight characteristics of cusp ions and the low-velocity cutoff
430 method originally developed by Onsager et al. (1990, 1991) for the magnetotail
431 reconnection location.

432 Figure 6 shows the general geometry of the low-velocity cutoff method that is used
433 to estimate the dayside magnetopause reconnection location from cusp observations.
434 Shown are the geomagnetic field lines (green), the reconnection location at the
435 magnetopause (X), the satellite position in the cusp (Θ), the ionospheric magnetic mirror
436 point on the cusp field line (M), and the orbit path of a satellite passing through the cusp
437 (red curve). A cusp-traversing satellite simultaneously observes slower magnetosheath
438 ions that arrive from the site of magnetopause reconnection (incident ion beam) and faster
439 magnetosheath ions that reached the ionospheric mirror point and returned to the high-
440 altitude cusp-traversing satellite (mirrored ion beam).

441 The color inlay of Figure 6, centered along the cusp field line, shows an H^+ velocity
442 distribution acquired by the TIMAS (Toroidal Imaging Mass Angle Spectrometer)
443 instrument (Shelley et al. 1995) on board Polar in the cusp on 20 October 1997 from

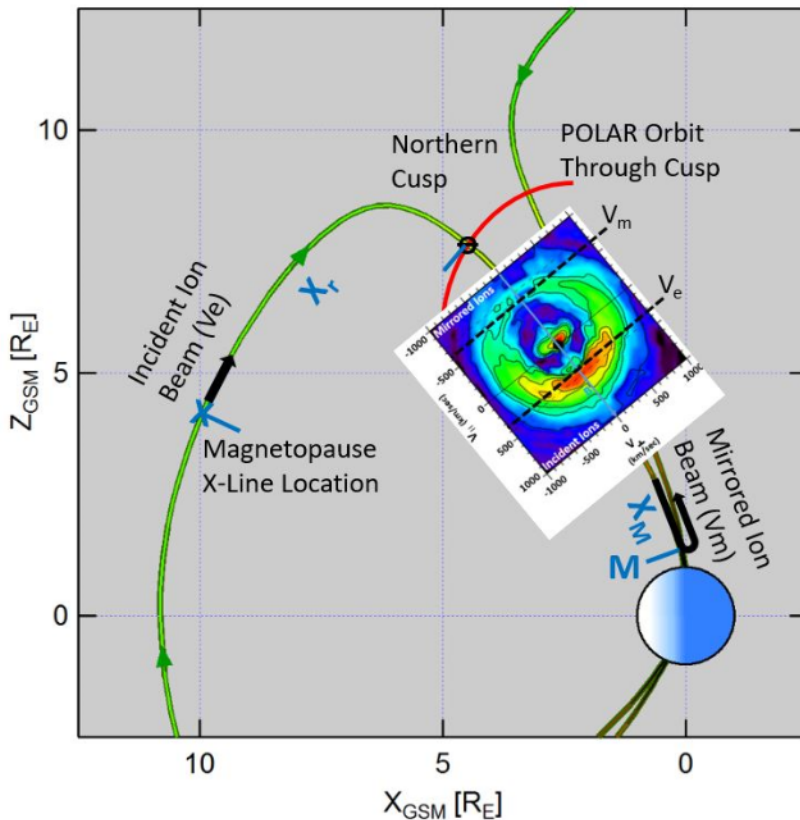
444 14:05:59 to 14:06:11 UT. The H^+ distribution is presented in magnetic field-aligned
 445 coordinates after removing the effect of the H^+ bulk flow transverse to the magnetic field,
 446 and shows the incident magnetosheath ions injected at the location of magnetopause
 447 reconnection in addition to the mirrored ions that returned from the ionospheric mirror
 448 points.

449 The distance X_r along the field line between a satellite in the cusp and the
 450 magnetopause reconnection site can be computed by

451
$$X_r/X_m = 2 V_e / (V_m - V_e), \quad (2)$$

452 derived from equating the flight times of the incident and mirrored ion beams. Here V_e
 453 and V_m are the cutoff velocities of the incident and mirrored beams, respectively, and X_m
 454 is the distance between the satellite and the mirror point (Figure 6). To determine the
 455 cutoff velocities, the peaks of the ion beams are fit with Gaussian distributions. The cutoff
 456 velocities are defined at the low-speed side of the peaks where the ion flux is $1/e$ of the
 457 peak flux (e.g., Fuselier et al. 2000; Trattner et al. 2007, 2005). The low velocity cutoffs
 458 are marked with black dashed lines in the color inlay of Figure 6.

459



460

461 **Fig. 6** Schematic of the northern cusp region with the Polar satellite simultaneously
 462 observing incident ions on newly opened magnetic field lines which originate at the

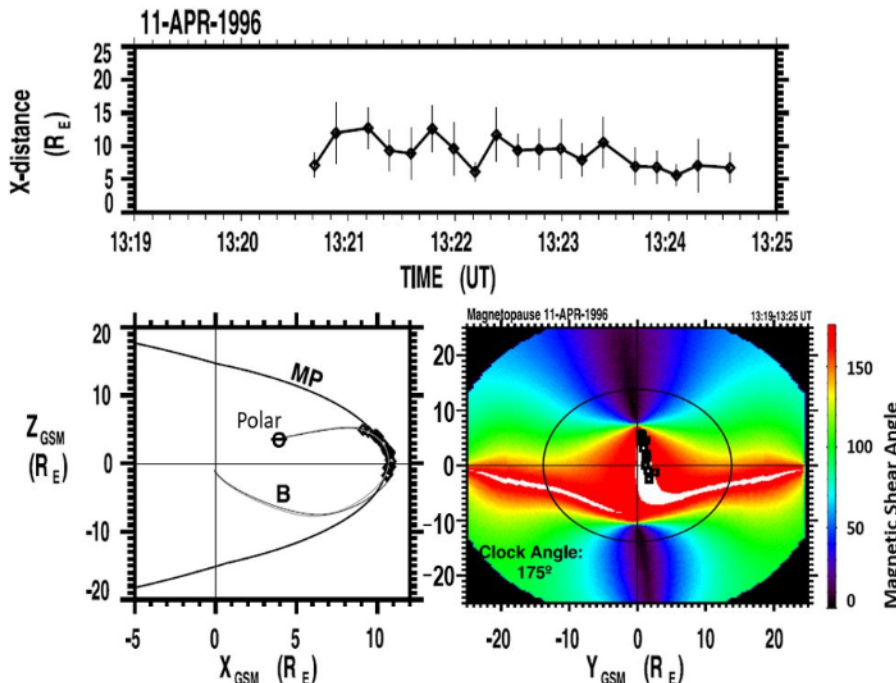
463 magnetopause reconnection location and mirrored ions returning from the ionosphere.
 464 The color distribution function shows the cutoff velocities V_e and V_m of the incident and
 465 mirrored ion beams, respectively.

466

467 To determine X_m , the geomagnetic field line at the satellite position in the cusp is
 468 traced down to the ionospheric mirror point by using the T96 model (Tsyganenko 1995).
 469 The model field line is also used to trace the calculated distance X_r back to the
 470 reconnection location on the magnetopause. These end points of the field line traces mark
 471 the location of dayside magnetopause reconnection where the magnetosheath plasma
 472 enters the magnetosphere (e.g., Fuselier et al. 2000; Trattner et al. 2007, 2012, 2021).

473 Figure 7 (top panel) shows the distance to the reconnection site derived from Eq. (2)
 474 versus the Polar/TIMAS observation time during the cusp crossing on 11 April 1996. The
 475 distance to the reconnection site ranges from about 6 to 12 R_E , which is most likely caused
 476 by changes in the satellite local time position. The uncertainties in the distance calculation
 477 are determined by those in measuring the low-velocity cutoff velocities. It is defined as
 478 1/2 the difference between the velocity at the peak and the low-velocity cutoff (Fuselier
 479 et al. 2000; Trattner et al. 2007).

480



481

482 **Fig. 7** The distance to the magnetopause reconnection site from the cusp position of the
 483 Polar satellite on 11 April 1996 (top panel). The location of the magnetopause
 484 reconnection site as seen from dawn (bottom left panel). The magnetopause magnetic

485 shear angle with the reconnection site location (black squares) as seen from the Sun for
486 the 11 April 1996 Polar cusp crossing (bottom right panel).

487

488 The lower left panel of Figure 7 shows the magnetopause shape as viewed from dawn.
489 Starting at the cusp location of the Polar satellite (Θ), the distance to the reconnection site
490 is traced along the T96 model geomagnetic field lines to the magnetopause where their
491 end points are marked with black diamonds.

492 The lower right panel of Figure 7 shows the plot of magnetic shear angle on the
493 magnetopause for the Polar cusp crossings. The shear angles are estimated by using the
494 T96 model (internal field) together with the Kobel and Flückiger (1994) magnetosheath
495 magnetic field draping model (external field), merged at the dayside ellipsoidal
496 magnetopause shape of the Sibeck et al. (1991) model (e.g., Trattner et al. 2007, 2021).
497 In the magnetic shear angle plot, the red areas represent the magnetopause antiparallel
498 reconnection region with magnetic shear angles $>160^\circ$. The white areas in the shear angle
499 plots represent regions where the model magnetic fields are within 3° of being exactly
500 antiparallel. The black circle represents the terminator plane at the magnetopause with the
501 black squares showing the plasma entry points at the magnetopause, the end points of the
502 cusp field line traces.

503 Because of the southward IMF conditions (IMF clock angle of 175°), the antiparallel
504 reconnection region (red) covers most of the dayside magnetopause with the white
505 regions for the highest magnetic shear shifted to the southern hemisphere due to the tilt
506 of Earth's magnetic dipole. An exception is the dusk region close to local noon where the
507 field-line trace points are also located.

508 The maximum magnetic shear model has been tested and validated for IMF conditions
509 with $|B_x|/B < 0.7$ (e.g., Trattner et al. 2017). The model predicts long continuous X-
510 lines that extend over the dayside magnetopause (e.g., Fuselier et al. 2002; Phan et al.
511 2006; Trattner et al. 2007; Dunlop et al. 2011; Trattner et al. 2021). For dominant IMF
512 B_y conditions, the model merges a component reconnection tilted X-line near the
513 subsolar magnetopause with the two branches of the antiparallel reconnection regions,
514 starting at the cusps and continuing towards the magnetotail along the flanks. The model
515 was expanded to northward IMF conditions using observations by Trenchi et al. (2008,
516 2009) and confirming the existence of a dayside X-line down to an IMF clock angle of
517 50° (see also Gosling et al. 1990; Trattner et al. 2017). It highlighted the importance of
518 antiparallel reconnection in constraining the location of the component reconnection line
519 (Trattner et al. 2018).

520 The maximum magnetic shear model shows anomalies for dominant IMF B_x conditions

521 ($|B_x|/B > 0.7$) which are the result of the limitations of the IMF draping models used to
522 determine the magnetopause magnetic shear. As shown by Michotte de Welle (2022),
523 using a global three-dimensional and exclusively data driven model for the magnetopause
524 magnetic shear, the local magnetic shear can differ significantly from the magnetic shear
525 determined from the currently used numerical models (section 3.1.4), causing the
526 anomalies in predicting the location of the dayside X-line. In addition, large
527 magnetopause surveys (Trattner et al., 2007, 2017, 2021), comparing observed X-line
528 locations with the predicted locations from the maximum magnetic shear model, also
529 showed anomalies for events at the spring and fall equinoxes, specifically for events with
530 IMF clock angles around 120 and 240 degrees, respectively. The fact that the equinox
531 anomalies occur for specific narrow parameter ranges points to a currently unknown
532 effect influencing the location of the magnetopause X-line under these conditions.

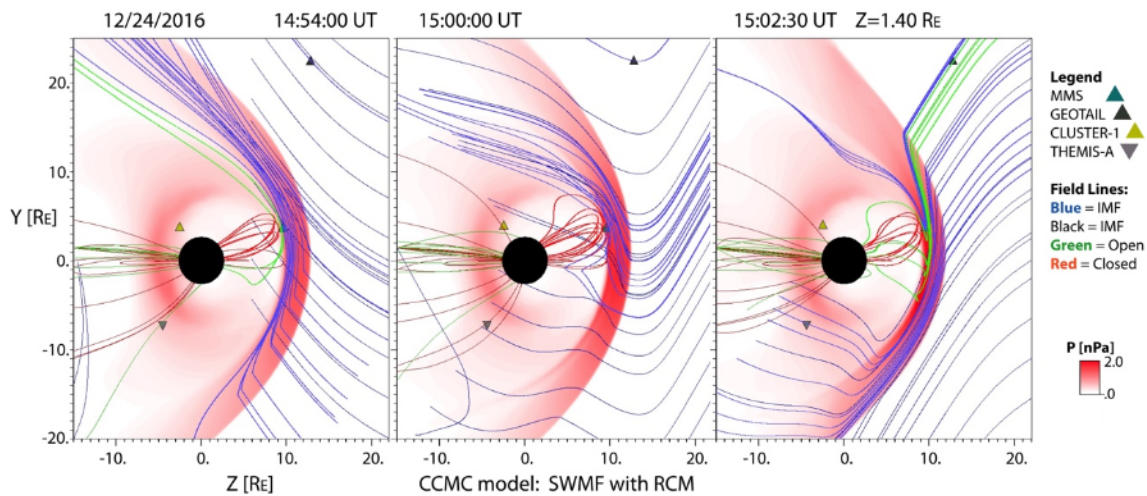
533 **3.1.2 Event-Specific Global MHD Modeling**

534 Global MHD models for simulating the solar wind-magnetosphere interaction can be
535 used to provide an important large-scale context and connectivity information to assist in
536 interpreting electron-scale observations of MMS. Runs on demand are readily requested
537 through the Community Coordinated Modeling Center (CCMC) (Table 2 in Appendix B).
538 Reiff and coauthors have now run the “SWMF” (Space Weather Modeling Framework)
539 model (BATS-R-US with “Rice Convection Model” (RCM)) (Toth et al. 2005; see also
540 Chapter 5.2 of this issue) for twelve instances where MMS observed crescent-shaped
541 electron velocity distributions (sections 4.1.6 and 4.3.1), both in the dayside
542 magnetopause region and in the tail (Reiff et al. 2018; Marshall et al. 2020, 2022). In each
543 case, the SWMF model placed an X-line (or its neighboring separatrix sheet) within 1 R_E
544 and 2 minutes of the time of the MMS encounter.

545 MHD models that include RCM (e.g., SWMF) appear to do a better job in predicting
546 the location of the reconnection sites in the tail. For example, the model predicted that
547 MMS should be at the lobe-plasma sheet boundary layer interface near the X-line for an
548 event on 23 June 2015 (Figure 5A,B in Reiff et al. (2016)). It also predicted that the X-
549 line for that event would be patchy across the tail (Figure 5B in Reiff et al. (2016)). For a
550 11 July 2017 substorm event, the model not only accurately predicted the near-earth
551 neutral line location but also predicted a huge plasmoid which was observed by MMS
552 (Torbert et al. 2018; Reiff et al. 2018). See Chapter 3.1, Figure 3.7 of this issue (Fuselier
553 et al. 2023) for comparison images for that event of CCMC versus other global MHD
554 models such as GGCM (Geospace General Circulation Model) (Raeder et al. 2017) and
555 LFM (Lyon-Fedder-Mobarry model) (Lyon et al. 2004).

556 CCMC models have also been helpful in determining the time for field line

557 reconfiguration, stretching and distortion for dayside events (Reiff et al. 2018). In a recent
 558 study, the location of the dayside X-line on 24 December 2016 moved dramatically as a
 559 result of a change in the Y-component of the IMF, with the model predicting not only
 560 reconnection at MMS but also connection of the Geotail spacecraft in the magnetosheath
 561 to the open field line on which MMS was situated (Figure 8). The Geotail data showed
 562 O⁺ fluxes just a few minutes after the model predicted a connection to the northern polar
 563 cap and a close conjunction with MMS.
 564



565 **Fig. 8** Evolution of the magnetic field line topology and spacecraft locations for an
 566 MMS dayside magnetopause reconnection event on 24 December 2016. Field lines are
 567 traced from MMS and from Geotail, and from other start locations. At time 14:54 UT,
 568 MMS was predicted by the SWMF model to be near the X-line, and on open field lines
 569 (green) connected to the southern cusp. Then the IMF B_y changed sign, and at 15:20:30
 570 UT, both MMS and Geotail were predicted to be on open field lines (green) connected to
 571 the northern polar cap, and their mapped field lines passed less than a half R_E (R_E : Earth
 572 radius) apart at the magnetopause. About a minute after the predicted connection, Geotail
 573 started observing O⁺ presumably from the magnetosphere, evidence of that connection.
 574
 575

576 In another study, an X-line that appears locally quite two-dimensional shows a
 577 dramatic difference in connection to the northern and southern ionospheres by field lines
 578 quite close on either side of the X-line, and electron fluxes correspondingly show a
 579 dramatic change in pitch angle (Marshall et al. 2022).

580 MHD models have also been run with embedded Particle-In-Cell (PIC) simulations,
 581 to overcome the inherent limitations of the MHD in reproducing kinetic-scale physics,
 582 e.g., MHD-EPIC (Chen et al. 2020). A recent CCMC workshop had dozens of

583 presentations on linking CCMC models to solar, interplanetary, PIC and
584 ionosphere/atmosphere models, many using open source modules
585 [<https://ccmc.gsfc.nasa.gov/ccmc-workshops/ccmc-2022-workshop/>].

586

587 **3.1.3 Data-Mining Approach to Reconstruction of the Global Reconnection 588 Structure**

589 The major problem in the global empirical reconstruction of the magnetosphere is
590 data paucity: At any moment the huge volume of the magnetosphere ($\gtrsim 10^5 R_E^3$) is
591 usually probed by less than a dozen spacecraft (e.g., Sitnov et al. 2020). In the past 15
592 years, it has been understood that this sparse data problem can be resolved or at least
593 substantially mitigated due to the recurrent nature of the main space weather actors,
594 storms and substorms. The storm occurrence depends on their intensity, as well as the
595 strength and phase of the solar cycle. For medium intensity storms the recurrence period
596 is about two weeks (Reyes et al. 2021). The recurrence time of periodic substorms is 2–4
597 h, while other substorm types have longer recurrence times depending on solar wind
598 conditions (Borovsky and Yakymenko 2017). As a result, the historical records of
599 spaceborne magnetometer observations can be organized using a multi-dimensional state-
600 space, formed from the global storm and substorm activity indices and the solar wind
601 input parameter. This allows the magnetic field for the event of interest to be reconstructed
602 from its nearest neighbors in this state-space and not only from observations during the
603 event. A specific data-mining (DM) technique leveraging this repeatability, the k-Nearest
604 Neighbor (kNN) classifier (Wettschereck et al. 1997; Sitnov et al. 2008), combined with
605 flexible and extensible magnetic field architectures (Tsyganenko and Sitnov 2007,
606 Stephens et al., 2019), helped organize multi-decade archives of spaceborne
607 magnetometer data to reconstruct storms (Tsyganenko and Sitnov 2007; Sitnov et al.
608 2008) and substorms (Stephens et al. 2019; Sitnov et al. 2019; hereafter referred to as
609 SST19 model). The DM approach outlined in Figure 9 can be summarized as follows:

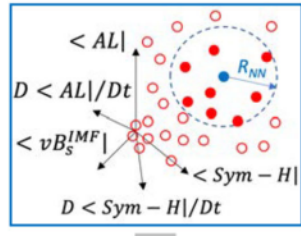
610 (a) First, a big database of historical magnetometer measurements (8.6 million points in
611 the work by Stephens et al. (2023)) is mined in a global parameter state-space
612 consisting of averaged values of the solar wind induced electric field $u_{sw} B_s^{IMF}$ (u_{sw}
613 is the solar wind velocity and B_s^{IMF} is the southward interplanetary magnetic field:
614 $B_s^{IMF} = -B_z^{IMF}$ when $B_z^{IMF} < 0$ and $B_s^{IMF} = 0$ otherwise, where B_z^{IMF} is the
615 north-south component of the IMF in GSM coordinates), the averaged *Sym-H* and *AL*
616 (geomagnetic activity) indices, and the *Sym-H* and *AL* time derivatives. The mining
617 procedure selects a small subset of moments at present but mostly in the past (red
618 circles in Figure 9a), for which these global parameters are close to the event of

619 interest in the state space (blue circle in Figure 9a). Events in this subset are called
620 the nearest neighbors.

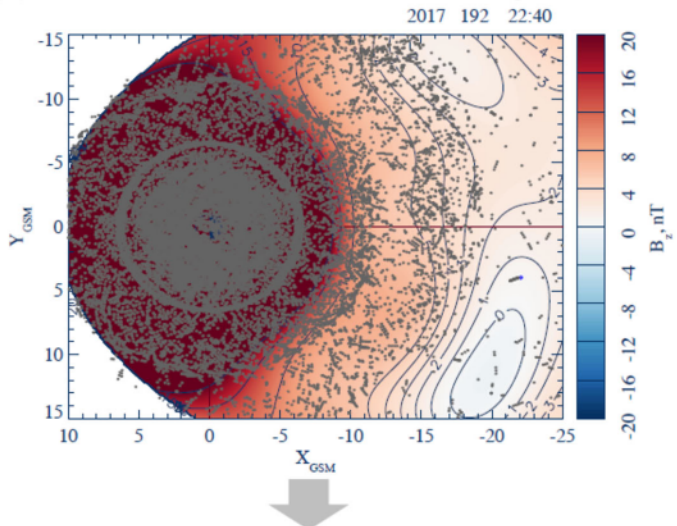
- 621 (b) The resulting subset of the magnetic field database (gray dots in Figure 9b), which is
622 much larger than the handful of actual satellites available at that moment, is used to
623 fit the free parameters of a very flexible magnetic field architecture ($\sim 10^3$ free
624 parameters) and to reveal details of the magnetosphere such as the formation of new
625 X-lines (at the earthward part of the $B_z = 0$ isocontour in Figure 9b).
- 626 (c) The obtained empirical model allows one to reconstruct a detailed 3D magnetic field
627 structure, as is shown in Figure 9c for the 11 July 2017 MMS EDR event (Torbert et
628 al. 2018).

629

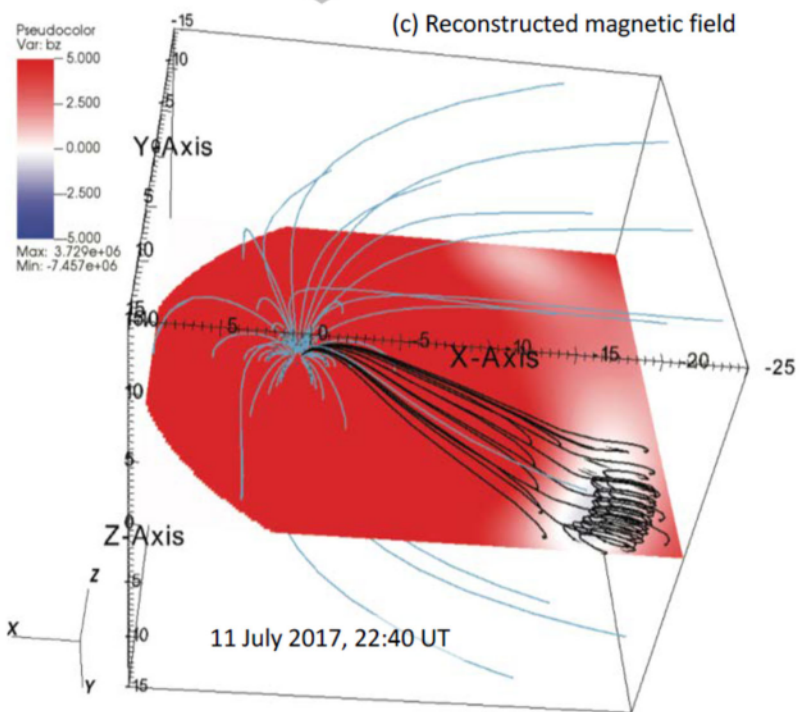
(a) Mining data in the global parameter space (kNN algorithm)



(b) kNN subset of the database to fit the magnetic field model



(c) Reconstructed magnetic field



630

631 **Fig. 9** The kNN DM method outline (Sitnov et al. 2021): (a) selecting nearest neighbors
632 for the event of interest (blue circle) in the 5D global parameter state-space; (b) finding

the corresponding subset in the magnetic field database (gray dots overplotted on the color-coded equatorial B_z distribution) and using it to fit the magnetic field model and to yield 2D magnetic field distributions (here the equatorial slice) as well as (c) 3D magnetic field distributions. The example shown here is for the 11 July 2017 MMS EDR event (Torbert et al. 2018)) with the color-coded equatorial B_z (in nT, saturated at 5 nT for better visualization) and a few sample field lines. Panels (a) and (b) are adapted from Sitnov et al. (2019).

640

The magnetospheric state shown in Figure 9a is characterized using geomagnetic indices and solar wind conditions. It can be described by a 5-D state-space vector, $\mathbf{G}(t) = (G_1, \dots, G_5)$, formed from the geomagnetic storm index (*Sym-H*), substorm index (*AL*), their time derivatives, and the solar wind electric field parameter ($u_{sw}B_s^{IMF}$). Most recently (Stephens et al., 2023), the *Sym-H* and *AL* indices have been replaced by the *SMR* and *SML* indices provided by the SuperMag project (Gjerloev 2012). The global binning parameters $G_{1-5}(t)$ are normalized by their standard deviations, smoothed over storm or substorm scales, and sampled at a 5-min cadence, as is detailed in Stephens and Sitnov (2021). Including the time derivatives of these activity indices allows the DM procedure to differentiate between storm and substorm phases as well to capture memory effects of the magnetosphere as a dynamic system (Sitnov et al. 2001). The space magnetometer archive contains data from 22 satellites (including four MMS probes) spanning the years 1995–2020 resulting in 8,649,672 magnetic field measurements after being averaged over 5 or 15 min time windows (Stephens et al. 2023).

Every query moment in time $t = t_q$ corresponds to a particular point in the 5-D state-space, $\mathbf{G}_{(q)} = \mathbf{G}(t_q)$. Its k_{NN} nearest neighbors (NNs) will be other points, $\mathbf{G}_{(i)}$, in close proximity to it: $R_i = |\mathbf{G}_{(i)} - \mathbf{G}_{(q)}| < R_{NN}$ (in the Euclidean metric). The specific choice of k_{NN} (and hence R_{NN}), is determined by a balance between over- and under-fitting. Stephens and Sitnov (2021) found the optimal number to be $k_{NN} = 32,000$, corresponding to ~1% of the total database (~ 10^7 sampling cases). The resulting set is composed of a very small number (~1–10) of real (available at the moment of interest) and a much larger number (~ 10^5) of virtual (from other events in the database) satellites.

The large number of NNs provided by such synthetic satellite observations enables the use of new magnetic field architectures (Tsyganenko and Sitnov 2007; Stephens et al. 2019), which differ from classical empirical models with custom-tailored modules (e.g., Tsyganenko and Sitnov 2005) by utilizing regular basis function expansions for the major magnetospheric current systems. In particular, the equatorial current system, which was previously described by ring and tail current modules, is now described by two

expansions representing arbitrary current distributions of thick and thin current sheets with different thicknesses. This architecture accounts for the multiscale structure of the tail current sheet with an ion-scale thin current sheet (TCS), with a thickness D_{TCS} , forming inside a much thicker current sheet, with a thickness $D \gg D_{TCS}$, during the substorm growth phase and then decaying during the expansion phase (e.g., Sergeev et al. 2011). The independence of the current sheet expansions is provided by the constraint $D_{TCS} < D_0 < D$, where D_0 is the ad hoc parameter $\sim 1R_E$. The proper reconstruction of substorms also requires a flexible description of the field-aligned currents, which is provided in the SST19 model using a set of distorted conical modules (Tsyganenko 1991) distributed in latitude and local time, as is discussed in more detail in Sitnov et al. (2017).

To improve the reconstructions, while fitting the magnetic field model with the NN subset, the spacecraft data were additionally weighted: in the real space, to mitigate the inhomogeneity of their radial distribution (Tsyganenko and Sitnov 2007), and in the state-space, to reduce the uncertainty and bias toward weaker activity regions (Sitnov et al. 2020; Stephens et al. 2020).

The SST19 model successfully describes the TCS buildup during the substorm growth phase and its decay during the expansion phase accompanied by the formation of the substorm current wedge (McPherron et al. 1973). It also identifies X-lines in the tail (Sitnov et al. 2019), which match in-situ MMS observations (Stephens et al. 2023), as is described in more detail in Chapter 3.1 of this issue (Fuselier et al. 2023). The model has been extensively validated using both in-situ observations (Sitnov et al. 2019; Stephens et al. 2019, 2020, 2023) and uncertainty quantification using DM binning statistics (Sitnov et al. 2019; Stephens et al. 2023).

692

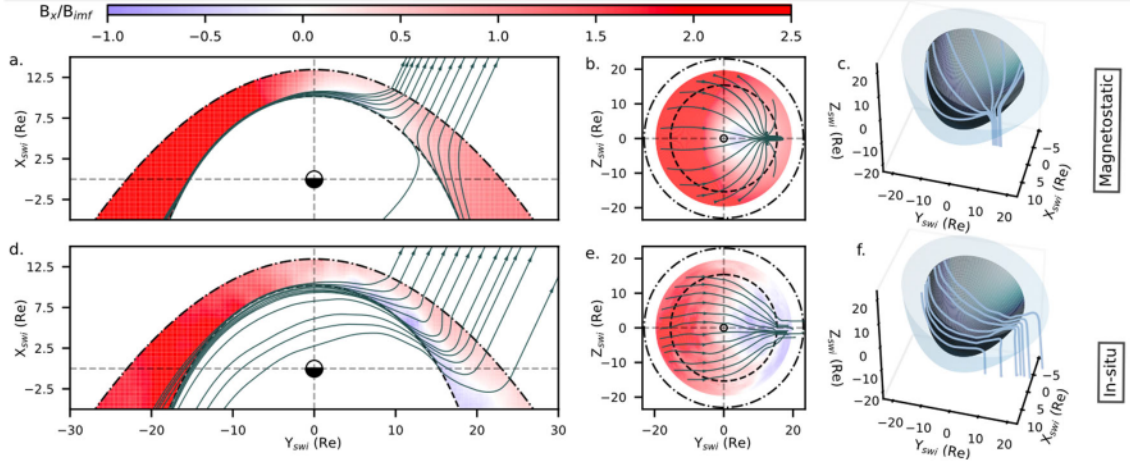
693 **3.1.4 Global 3D Structure of the Magnetosheath Using In Situ Measurements: 694 Application to Magnetic Field Draping**

695

The dynamics of the Earth's magnetosphere and its coupling to the solar wind importantly depends on how the solar wind interacts at the bow shock and, in particular, on how the plasma is decelerated, heated and deflected there and on how the interplanetary magnetic field drapes around the magnetospheric obstacle in the magnetosheath. The specific structure of the draping, in particular, plays a major role for the reconnection of magnetic field lines at the magnetopause. Magnetic field draping was thus the focus of a study by Michotte de Welle et al. (2022) that permits, based on large-scale statistics of in situ spacecraft measurements, to reconstruct the global 3D structure of the magnetosheath.

705 Magnetic field draping is a fairly well understood concept, resulting from the frozen-
706 in condition ruling the evolution of magnetized plasmas on large scales. However, our
707 knowledge of the 3D global draping structure in the Earth's magnetosheath is very limited
708 and is mostly described by analytical and numerical models. Michotte de Welle et al. have
709 recently succeeded in reconstructing the 3D structure of the magnetic draping over the
710 whole dayside of the magnetosphere, using only in situ observations, and as a function of
711 the IMF orientation. Two decades of data from Cluster, Double Star, THEMIS and MMS
712 missions have been used for that purpose. The measurements made in the magnetosheath
713 were extracted automatically using a Gradient Boosting Classifier trained to classify
714 magnetosphere, magnetosheath and solar wind data points (Nguyen et al. 2022a). About
715 50 million measurements were extracted and then associated with a causal solar wind and
716 IMF conditions from OMNI data using a solar wind propagation method (Safrankova et
717 al. 2002). The position of each data point relative to the bow shock and the magnetopause
718 at the time of the measurement is then estimated using a Gradient Boosting Regression
719 model of the boundaries, parameterized with solar wind and IMF conditions. All points
720 are then repositioned between a standard bow shock and magnetopause boundary,
721 determined for average solar wind conditions, and rotated into the solar wind
722 interplanetary (SWI) magnetic field coordinate system (Zhang et al. 2019) in which the
723 upstream IMF direction is parallel to the XY plane. This last step is crucial to ensure each
724 point falls in the right sector of the magnetosheath (quasi-parallel or quasi-perpendicular
725 bow shock sides) with respect to its causal IMF. Magnetic field lines are then integrated
726 with a standard ordinary differential equation integrator, using at each step the weighted
727 average of the k-Nearest Neighbor magnetic field measurements close to the current
728 iteration step position (with k=45000).

729



730 **Fig. 10** From left to right: representation of the magnetic field lines in the XY (left), YZ
 731 (middle) planes and in 3D (right) as predicted by the KF94 magnetostatic model (top
 732 panels) or reconstructed from in situ data (bottom panels). On the four leftmost panels,
 733 the color codes the value of the B_x component of the magnetic field. Coordinates are from
 734 the SWI system.

735

736 The bottom three panels of Figure 10 show the obtained draping in the XY and YZ
 737 planes of the SWI coordinate system and in 3D on the rightmost panel. As a comparison,
 738 the top three panels show, for the same points of view, the draping obtained with the
 739 magnetostatic model of Kobel and Fluckiger (1994) (referred to as the KF94 model). In
 740 this configuration, the represented data is the subset of all measurements for which the
 741 associated IMF cone angle falls between 20° and 30° from the Sun-Earth axis. The figure
 742 reveals that the observed draping is fundamentally different from the modeled one. In the
 743 modeled draping, the magnetic field appears to diverge as it approaches the magnetopause
 744 in the region downstream of the quasi-parallel bow shock. This is the result of the only
 745 two constraints imposed by the model to the magnetic field. Indeed, on the one hand, the
 746 magnetic field in the quasi-parallel (positive Y) region is mostly conserved as it crosses
 747 the bow shock. On the other hand, the field must be tangential to the magnetopause. While
 748 these two constraints also apply in reality (if one neglects magnetopause reconnection as
 749 a first approximation), magnetic flux is also bound to the plasma as it flows upstream of
 750 the bow shock and circumvents the magnetopause in the magnetosheath. In other words,
 751 fluid elements connected to a magnetic flux tube entering the quasi-parallel region must
 752 remain connected to those that entered earlier on the quasi-perpendicular bow shock
 753 (negative Y) side. The considerable slowing down of the flow in the subsolar region
 754 forces all field lines entering in the quasi-parallel magnetosheath to head to the dayside

755 where the flux piles up, rather than diverge partly to the nightside as the magnetostatic
756 model predicts. This large-scale kink in magnetic field lines is thus associated with a
757 macroscopic current sheet at mid-depth of the quasi-parallel side of the magnetosheath,
758 an effect that is not seen with the vacuum magnetostatic model. The main consequence is
759 that for this range of IMF cone angles, a large part of the magnetopause on the quasi-
760 parallel region sees a magnetic shear that is vastly different from that predicted using the
761 KF94 model, potentially adding difficulties to the maximum shear angle reconnection
762 model in that cone angle regime.

763 Interestingly, when the IMF becomes quasi-radial (B_x dominant), in practice when
764 the cone angle is less than about 12° , magnetically connected solar wind elements are so
765 far apart along the Sun-Earth line that by the time fluid elements arrive on the quasi-
766 parallel side of the bow shock, connected fluid elements entered in the subsolar region
767 have long ago re-accelerated and joined the nightside of the system. As a result, field lines
768 are not kinked anymore and rather diverge on the magnetopause, which coincidentally
769 qualitatively agrees with the vacuum magnetostatic model prediction (Michotte de Welle
770 et al. 2022). For IMF cone angles larger than 45° , i.e., field lines arriving rather
771 perpendicular to the Sun-Earth axis, the draping is also found to qualitatively match that
772 predicted by the KF94 model.

773 This study was limited to the reconstruction of the field line draping. The method is
774 precise enough to reconstruct the overall dependency of the magnetic topological
775 properties on the IMF orientation. Local and detailed quantitative properties of the field
776 such as its divergence-free character cannot be ensured, although on average $|\nabla \cdot \mathbf{B}|$ is
777 on the order of $0.01B_{\text{IMF}}/R_E$, where B_{IMF} is the upstream field intensity and Earth's
778 radius R_E is comparable to the scale of field variations. Similar analysis can be made to
779 reconstruct the global distribution of any physical quantities, providing the capability to
780 reconstruct the global 3D structure of the solar wind–dayside magnetosphere interaction
781 globally. The amount of data now available and modern statistical learning methods will
782 prove useful to understand how physical parameters distribute on and around critical
783 regions such as the magnetopause for various upstream conditions, which is a topic of on-
784 going work.

785

786 **3.2 Coordinate System, Frame Velocity, and Spacecraft Trajectory Estimation**

787 Current sheets where reconnection may occur are never strictly stationary, their local
788 normal direction can be highly variable in space and time, and the X-line, possibly
789 embedded in those current sheets, may be moving, depending on the external conditions
790 and instabilities excited in the current sheets. It is thus indispensable, for each current

sheet crossing or reconnection event, to be able to obtain a proper coordinate system and frame velocity of the current sheet structure or reconnection regions. In this section, we briefly review various methods to estimate the characteristic orientations and motion of the structures from in-situ measurements.

3.2.1 Dimensionality and Coordinate Systems

Here we review methods for estimating the dimensionality and coordinate systems of magnetic or plasma structures in space from in-situ data. Since an overview was given by Sonnerup et al. (2006a) and Shi et al. (2019) on various single- and multi-spacecraft analysis methods for estimating the orientation and motion of plasma discontinuities (one-dimensional (1D) structures, such as planar current sheets), we focus only on recent developments.

Minimum Directional Derivative In Minimum Directional Derivative (MDD) analysis, a multi-spacecraft method applicable to four-spacecraft measurements at any instant of the magnetic (or any vector) field, one takes the gradient of the magnetic field vector, multiplies the resulting matrix by its transpose, and then solves for the eigenvectors of the resulting matrix, finding time-dependent maximum, intermediate, and minimum gradient eigenvalues, λ_{\max} , λ_{int} , and λ_{\min} , which represent the squared gradient in the respective time-dependent directions, $\hat{\mathbf{e}}_n$, $\hat{\mathbf{e}}_l$, and $\hat{\mathbf{e}}_m$, respectively (Shi et al. 2005, 2019) (alternatively, the eigenvalues can be defined as the square root of these quantities, proportional to the gradient in the respective directions). If $\lambda_{\max} \gg \lambda_{\text{int}}, \lambda_{\min}$, the system is roughly one dimensional with variation mainly in the maximum gradient ($\hat{\mathbf{e}}_n$) direction. If $\lambda_{\max}, \lambda_{\text{int}} \gg \lambda_{\min}$, the system is roughly two-dimensional (2D) with variation mainly in the maximum and intermediate gradient directions ($\hat{\mathbf{e}}_n$ and $\hat{\mathbf{e}}_l$, respectively). If all eigenvalues are comparable, the system is 3D with variation in all three directions, $\hat{\mathbf{e}}_n$, $\hat{\mathbf{e}}_l$, and $\hat{\mathbf{e}}_m$ (Shi et al. 2019). Rezeau et al. (2018) introduced dimensionality parameters that are useful for determining the dimensionality of the system, $D_{1D} = (\lambda_{\max} - \lambda_{\text{int}})/\lambda_{\max}$, $D_{2D} = (\lambda_{\text{int}} - \lambda_{\min})/\lambda_{\max}$, and $D_{3D} = \lambda_{\min}/\lambda_{\max}$; D_{1D} , D_{2D} , and D_{3D} quantify the degree to which the system is 1D, 2D, or 3D, respectively.

In practice, when studying magnetic reconnection events, λ_{\max} is often significantly greater than the other two eigenvalues in the vicinity of the current sheet (D_{1D} close to unity). However, the system can be somewhat two-dimensional if $\lambda_{\text{int}} \gg \lambda_{\min}$ so that the variation in the minimum gradient direction can be neglected relative to that in the other two directions, yielding a system that can be analyzed as quasi-2D. (Unfortunately, the minimum MDD eigenvalue direction is not always the M direction as defined below (Denton et al. 2016, 2018).) The coordinate system usually used to describe magnetic reconnection (the so-called LMN coordinate system) has the L direction in the direction

827 of the reconnecting magnetic field and the N direction normal to the current sheet; the M
828 direction completes the triad. Because λ_{\max} is often very large, the MDD maximum
829 gradient direction, $\hat{\mathbf{e}}_N$, found from the time dependent $\hat{\mathbf{e}}_n$ direction, is often the most
830 accurately determined direction in the system, and can usually be used to define the
831 normal direction across the current sheet. Then in order to define the reconnection
832 coordinate system, it remains to find one more direction.

833 **Hybrid Methods** Denton et al. (2016, 2018), studying the 16 October 2015
834 magnetopause reconnection event of Burch et al. (2016b), determined the L direction as
835 the maximum variance direction of Minimum Variance Analysis (MVA) (Sonnerup and
836 Cahill 1967; Sonnerup and Scheible 1998) of the magnetic field. This is reasonable seeing
837 as the reconnection magnetic field reverses across the current sheet, leading to large
838 variance. The M direction can be taken to be the direction of the cross product between
839 $\hat{\mathbf{e}}_N$, defined by MDD and $\hat{\mathbf{e}}_L$, defined by MVA, but if $\hat{\mathbf{e}}_N$ and $\hat{\mathbf{e}}_L$ are not exactly
840 orthogonal, a choice must be made to determine the N and L directions. For instance, one
841 could take $\hat{\mathbf{e}}_N = \hat{\mathbf{e}}_{N'}$, and find L from $\hat{\mathbf{e}}_L = \hat{\mathbf{e}}_M \times \hat{\mathbf{e}}_N$, which is what Denton et al. (2016)
842 did. Denton et al. (2018) proposed a hybrid method weighting the influence of $\hat{\mathbf{e}}_N$ and
843 $\hat{\mathbf{e}}_L$, based on the ratio of the maximum MDD eigenvalue to the maximum MVA
844 eigenvalue.

845 Genestreti et al. (2018) found that Denton et al.'s (2018) method did not work well
846 for the 11 July 2017 magnetotail reconnection event studied by Torbert et al. (2018).
847 Instead, Genestreti et al. used the maximum variance direction of MVAVe (Minimum
848 Variance Analysis of the electron bulk velocity \mathbf{u}_e) to determine the L direction. Large
849 variance in the velocity moments along the L direction are expected since the
850 reconnection outflow will be along that direction. (Another possibility is to use MVAE,
851 using the variance of the electric field.) Heuer et al. (2022) recently proposed a hybrid
852 system similar to that of Denton et al. (2018), except that $\hat{\mathbf{e}}_L$ is determined from MVAB
853 (MVA using the magnetic field) only when the spacecraft have a significant velocity
854 component across the current sheet in the frame of the magnetic structure. If the velocity
855 of the spacecraft relative to the magnetic structure is mostly in the L direction, they
856 recommend using MVAVe to determine $\hat{\mathbf{e}}_L$.

857 **Magnetic Configuration Analysis** Among the analysis methods that are enabled by four-
858 spacecraft measurements are those that allow the determination of the geometrical
859 properties of the magnetic field. Following the main ideas of the magnetic MDD (Shi et
860 al. 2005) and magnetic rotational analysis procedure (Shen et al. 2007), Fadanelli et al.
861 (2019) derived a new method named the “magnetic configuration analysis” (MCA). The
862 method in effect determines the main axes of the magnetic field rotation rate in space, in

a normalized fashion, and permits the categorization of magnetic field geometries in terms of planarity and elongation properties, for instance. MCA is thus designed to estimate the spatial scales on which the magnetic field varies locally and to determine the actual magnetic field shape and dimensionality from multi-spacecraft data. Case studies using MMS data showed that the method is capable of determining, for example, the planar and cigar shapes of structures such as current sheets and small flux ropes, respectively. An interesting property of such a method is that the determination is made very locally, at the scale of the inter-spacecraft separation, which is much smaller than that of the current sheet or flux rope itself.

Fadanelli et al. (2019) also statistically applied the MCA method to magnetic field observations in different near-Earth regions (magnetosphere, magnetosheath, and solar wind). The findings show that the magnetic field structure is typically elongated at small scales (cigar and blade shapes), is less frequently planar (pancake shapes generally associated with current sheets), but rarely shows an isotropic variance in the magnetic field rotation rate. The occurrence frequency of the type of magnetic geometries observed and, most importantly, their scale lengths, strongly depend on the region sampled and plasma β . Interestingly, the most invariant direction is statistically aligned with the electric current, suggesting that electromagnetic forces are fundamental in determining the magnetic field configuration at small scales.

882

883 **3.2.2 Velocity of the Magnetic Structure**

In addition to determining the coordinate system, it is beneficial to determine the velocity of the magnetic structure in order to determine a reference frame in which the magnetic structure is approximately time stationary (what Shi et al. (2019) call the “proper reference frame”). In homogeneous regions, such a velocity can be the $E \times B$ velocity or the ion velocity perpendicular to the background magnetic field for MHD-scale structures, and in ion diffusion regions (IDRs) the perpendicular components of the electron velocity can be used. A related approach, applicable to inhomogeneous regions, is deHoffmann-Teller (HT) analysis, which finds a frame with minimum electric field, and hence the frame in which ion or electron flows are roughly aligned with the spatially varying magnetic field (deHoffmann and Teller 1950; Khrabrov and Sonnerup 1998). However, these approaches are unreliable in the EDR.

Four spacecraft timing analysis (Dunlop and Woodward 1998), which assumes that the spatial structure varies in only one direction, can yield the velocity component along that direction, namely, the velocity normal to the plane along which spatial gradient is

negligible. However, results may vary depending on the input quantity used. Minimum Faraday residue analysis (MFR) is another approach to get the normal velocity of MHD discontinuities from single-spacecraft data (Terasawa et al. 1996; Khrabrov and Sonnerup 1998).

Shi et al. (2006) introduced the Spatio-Temporal Difference (STD) method, which solves for the structure velocity from the convection equation for steady magnetic structures ($\partial \mathbf{B} / \partial t = 0$)

$$\frac{d\mathbf{B}}{dt} = (\mathbf{V}_{sc} \cdot \nabla) \mathbf{B} = -(\mathbf{V}_{str} \cdot \nabla) \mathbf{B}, \quad (3)$$

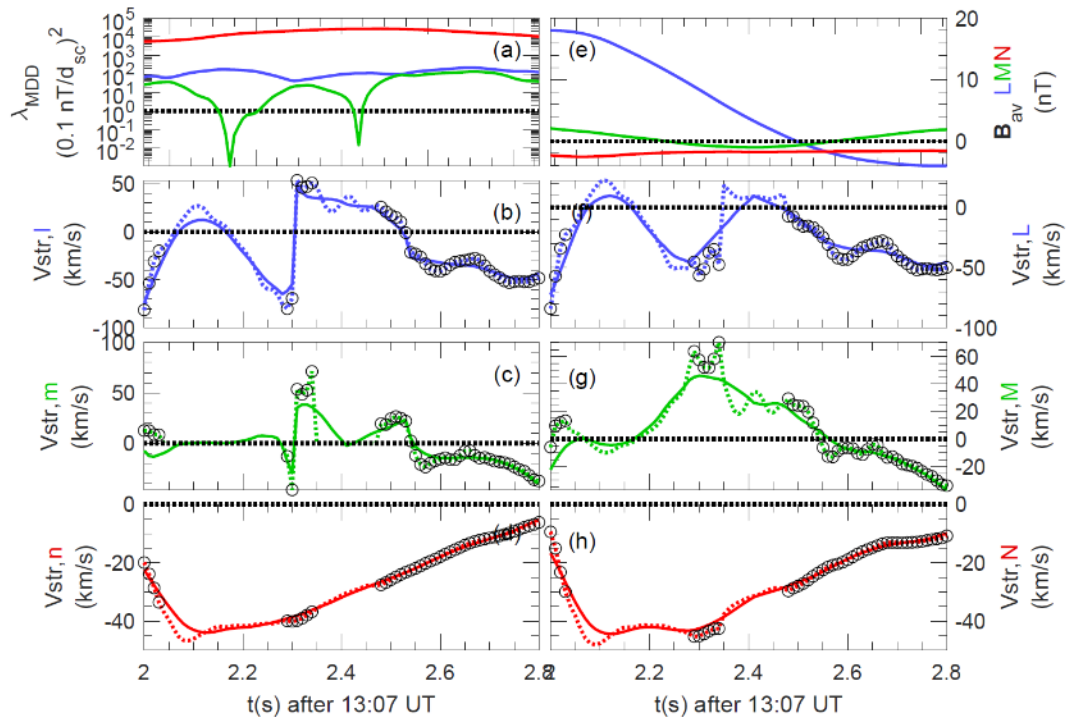
using instantaneous values of the magnetic gradient at one time, and a centered time step around that time for the total time derivative $d\mathbf{B}/dt$ observed by the spacecraft. Here \mathbf{V}_{sc} is the spacecraft velocity relative to the magnetic structure, and \mathbf{V}_{str} is the structure velocity relative to the spacecraft. Using Eq. (3) assumes that the velocity is constant on the spatial scale of the four spacecraft and on the time scale for motion across that spatial scale. However, in most cases, only one or at most two velocity components can be determined, because when the gradient is very small, the velocity component in that direction is unreliable (Shi et al. 2019; Denton et al. 2021). Here we examine the 16 October 2015 magnetopause reconnection event of Burch et al. (2016b) and introduce a modification of STD to get as much information as possible from STD.

Figure 11a shows the MDD eigenvalues normalized to $(0.1 \text{ nT}/d_{sc})^2$, where 0.1 nT is the maximum calibration error of the MMS magnetometers and d_{sc} is the average spacecraft spacing; $(0.1 \text{ nT}/d_{sc})^2$ represents a reasonable minimum value required for accuracy of the squared gradient. In Figure 11a, the maximum and intermediate eigenvalues are always well above this value, suggesting that they can be satisfactorily determined. However, where the minimum eigenvalue becomes significantly smaller than this value, the STD velocity component in that direction has unrealistically large values. Where all three normalized eigenvalues are significantly above unity, however, as sometimes happens for this event (like after $t = 2.5 \text{ s}$ in Figure 11a), we may be able to determine a three-dimensional velocity. For the calculations leading to Figure 11, we required that an eigenvalue be at least $20(0.1 \text{ nT}/d_{sc})^2$ in order to include the STD velocity component associated with that eigenvalue. (A large value was required to yield consistent velocities.) Otherwise, that component was set equal to zero. Figures 11b-d show the velocity components calculated in the time-dependent MDD intermediate, minimum, and maximum gradient directions, $\hat{\mathbf{e}}_L$, $\hat{\mathbf{e}}_M$, and $\hat{\mathbf{e}}_N$, respectively. In Figure 11c, the dotted green curve is the instantaneous STD velocity component for the MDD local minimum gradient ($\hat{\mathbf{e}}_m$) direction. Black circles mark the data points where all three

933 velocity components are determined, and at data points without black circles, the dotted
 934 green curves drop to zero.

935 Figures 11f–h show the resulting velocity in the fixed LMN coordinate system that
 936 was found using the hybrid method of Denton et al. (2018). The N direction agrees well
 937 with the instantaneous MDD $\hat{\mathbf{e}}_n$ direction, but the L direction is found from the direction
 938 of maximum variance of the magnetic field. Note that whereas the l and m components
 939 of the velocity reverse at $t = 2.3$ s in Figures 11b and 11c, the velocity components in the
 940 fixed L and M directions are well behaved in Figures 11f and 11g. Thus in Figure 11, we
 941 have calculated a three-dimensional structure velocity at the times indicated by the black
 942 circles. The velocity is less reliable at the other times because of the omission of the
 943 minimum gradient component.

944



945

946 **Fig. 11** STD analysis for the 16 Oct 2015 magnetopause reconnection event. (a) MDD
 947 eigenvalues, (b–d) STD structure velocity components in the local MDD gradient
 948 directions, $\hat{\mathbf{e}}_l$, $\hat{\mathbf{e}}_m$, and $\hat{\mathbf{e}}_n$ respectively, (e) magnetic field averaged over the four MMS
 949 spacecraft, (f–h) STD structure velocity in the fixed LMN coordinates. The dotted curves
 950 are the instantaneous velocities, and the solid curves are smoothed over a time scale of
 951 0.5 s.

952

953 Denton et al. (2021) used polynomial reconstruction (section 3.3.1) to track the

954 motion of the X-line, and the resulting velocity was in rough agreement with the STD
955 velocity in the LN plane for times for which the X line was less than two d_{sc} from the
956 centroid of the MMS spacecraft. Another approach is to match MMS observations to
957 simulation data in order to find a velocity though the simulation fields (Shuster et al.
958 2017; Nakamura et al. 2018b; Egedal et al. 2019; Schroeder et al. 2022; section 3.2.3).
959

960 3.2.3 Spacecraft Trajectory Estimation

961 MMS observations of a magnetotail EDR can be directly compared to 2D kinetic PIC
962 simulation, for determination of spacecraft trajectories in the event specific LN -plane. As
963 will be described in detail in Section 3.3.3, the trajectory of the MMS constellation further
964 allows for reconstruction of the MMS data in a 2D format, which can in turn be compared
965 against the simulation data. Note that these methods rely on spacecraft observations with
966 sufficient features to well constrain the trajectory. The MMS event considered here (10
967 August 2017) features strong electron pressure anisotropy followed by large electric field
968 gradients that indicate a path that closely follows a separatrix layer. For events that do not
969 exhibit such features, one may find difficulty in accurate determination of the spacecraft
970 trajectory.

971 **Spacecraft trajectory optimization** The spacecraft paths are found through a χ^2 -
972 optimization procedure, in which a penalty function made up of a sum of squared
973 deviations of spacecraft measurements from corresponding simulation quantities is
974 minimized, similar to that laid out in Egedal et al. (2019). However, some adjustments
975 are made to suit the MMS event at hand. Similarly to the previous method, PIC simulation
976 units are converted to physical MMS units using two parameters, the ratio of PIC to MMS
977 densities and the ratio of PIC to MMS temperatures. Once simulation units are converted,
978 a direct numerical optimization scheme to fit the spacecraft path is tractable.

979 To ensure a well-fit magnetic field profile the path is optimized in such a way that it
980 is constrained to be on PIC simulation contours that match the B_L values measured by
981 MMS1. This amounts to optimizing the MMS1 position along a unique simulation B_L
982 contour at each time point, reducing a 2D problem to a 1D problem and largely
983 simplifying the numerical method. The choice of MMS1 in optimizing the path is
984 arbitrary; one may choose any other spacecraft or use mean magnetic field value at the
985 centroid and can achieve near identical results. The event-specific LMN axes (section
986 3.2.1) combined with the converted simulation units allows for determination of the
987 spacecraft positions relative to MMS1 in the simulation LN -plane.

988 At each time point, a penalty function $h(r)$ is evaluated, where h is a sum of weighted
989 χ^2 -differences between spacecraft measurements and corresponding simulation data

990 parameterized by r , the distance along the given B_L contour that matches MMS1 data.
991 The signals included in the penalty function are all components of the electromagnetic
992 fields (except for $B_{L,MMS1}$), electron and ion flow velocities, parallel and perpendicular
993 electron pressures, and the ratio of parallel to perpendicular electron pressures. An
994 additional contribution to the penalty function, $g(r)$, penalizes solutions whose positions
995 r are too far away from that at the previous time step r_{previous} and ensures a continuous
996 trajectory. This contribution takes the exact form $g(r) = (r - r_{\text{previous}})^2 / \sigma_g^2$, where σ_g is
997 an adjustable weight to enforce a smooth trajectory.

998 The optimization problem is solved by stepping through time and taking the
999 MMS1 position to be the r -value corresponding to the minimum value of the penalty
1000 function. For further details of this method, see Supporting Information of
1001 Schroeder et al. (2022).

1002

1003 **3.3 Methods for Reconstructing 2D/3D Structures**

1004 **3.3.1 Field Reconstruction Using Quadratic Expansion**

1005 To understand the context of reconnection events, it is desirable to have a
1006 reconstruction of the magnetic field in the vicinity of the spacecraft. Without an explicit
1007 reconstruction, researchers map the location of the spacecraft by comparing the time
1008 series of \mathbf{B} to the nominal diffusion region picture seen in many 2D simulations (e.g., see
1009 Torbert et al. 2018), often using the LMN coordinate system as determined in different
1010 ways and described in section 3.2. MMS provides new measurements that allow
1011 reconstructions that depend only on the data and the vanishing divergence of the magnetic
1012 field. This is made possible because of: 1) the very high fidelity of the current density
1013 measurements using only particle data (Pollock et al. 2016; Phan et al. 2016); and 2) the
1014 very high accuracy of the magnetometers (Russell et al. 2016), assisted with independent
1015 measurements of the field magnitude by the Electron Drift Instrument (EDI) (Torbert et
1016 al. 2016b). Using a “modified” curlometer (see Dunlop et al. (1988) for the original
1017 method), which employs both temporal and spatial variations of \mathbf{B} to estimate the current
1018 density, Torbert et al. (2017) showed that the particle data matched the magnetic
1019 variations at the highest cadence available on MMS within an EDR, where the current
1020 density is far from uniform.

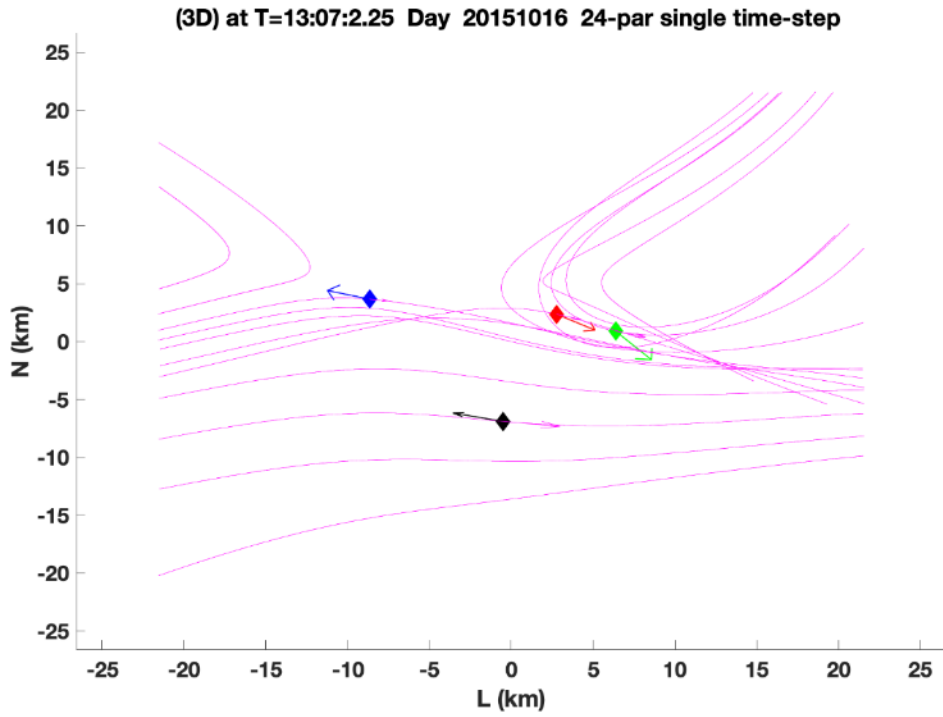
1021 If the current density \mathbf{j} from the particle measurements at four spacecraft locations is
1022 assumed correct, then one can extend the linear curlometer approximation (Dunlop et al.
1023 1988) to the second order and reconstruct the magnetic topology in the vicinity of the
1024 MMS tetrahedron to sense the locations of X-lines and the four spacecraft within the
1025 diffusion region. Torbert et al. (2020) implemented such a reconstruction, using a 24-

1026 parameter Taylor expansion around the barycenter of the tetrahedron. Given that there are
1027 24 knowns (3 components times 4 spacecraft measurements of \mathbf{B} and \mathbf{j}), this gives a
1028 solution for the field that exactly matches the data, with the divergence of \mathbf{B} zero
1029 everywhere. However, such an exact solution requires the addition of at least one cubic
1030 term in the expansion because of the constraint that the divergence of the current density,
1031 which in the expansion is computed from the curl of \mathbf{B} , must be zero (neglecting the
1032 displacement current for a nonrelativistic system). The measured current values almost
1033 never have this property, for the primary reason that they are taken at separated spatial
1034 locations where the current may be highly varying. Torbert et al. (2020) assumed that the
1035 second derivative in the MDD minimum gradient direction was zero, and arrived at an
1036 exact fit for spacecraft measurements of \mathbf{B} and \mathbf{j} by using a superposition of cubic terms
1037 weighted by the inverse of the coefficient required for each term.

1038 Given that MMS can measure the electron distribution and compute the current
1039 density every 30 ms (and sometimes every 7.5 ms (Rager et al. 2018; see also Appendix
1040 A)), a reconstruction can be computed for every such time step. As an example, such a
1041 reconstruction is given in Figure 12, for a time when the MMS constellation approached
1042 an EDR at the magnetopause on 16 October 2015, as reported by Burch et al. (2016b).
1043 The field is computed in a 3D cubic lattice, and the field lines are traced in this lattice.
1044 The field lines are then projected into the shown LN plane. The field topology is
1045 insensitive to the actual weighting of the 18 solutions using different cubic terms. Using
1046 such a reconstruction with synthetic data from simulation as input, Torbert et al. (2020)
1047 showed that these reconstructions are very representative of the simulation data within a
1048 volume whose linear extent is about twice that of the spacecraft tetrahedron.

1049 Denton et al. (2020) implemented a modification of this technique, using only
1050 quadratic terms, based on scaling arguments for the various terms and the concern that
1051 the exact solutions may lead to over-fitting of the data and show spurious X-lines when
1052 far from the tetrahedron. The number of terms in the expansion is reduced using estimates
1053 of their relative scaling, and the coefficients are then determined by a least-squares fitting
1054 procedure with an assumed weighting between the \mathbf{B} and \mathbf{j} values, depending on their
1055 accuracies. Although the data cannot exactly match the model for reasons described above,
1056 these reconstructions appear to give better results without false X-lines when sensing the
1057 presence of X-lines out further from the tetrahedron.

1058

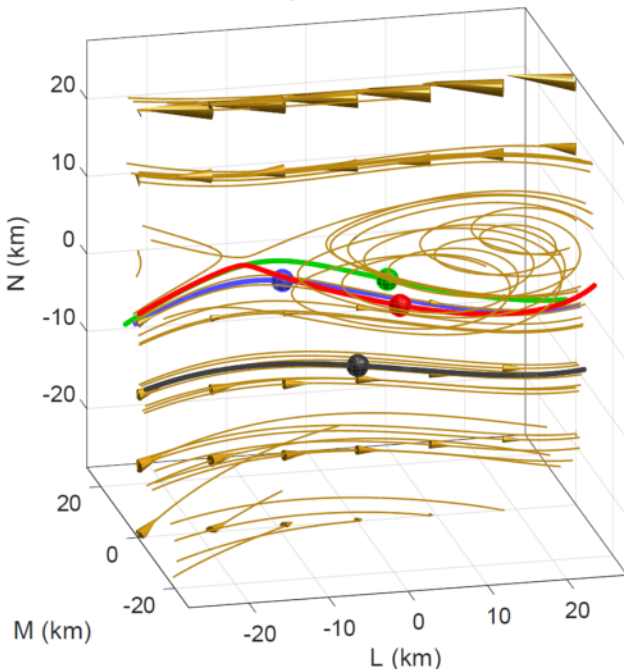


1059

1060 **Fig. 12** A reconstruction of the magnetic field lines as MMS approached an electron
 1061 diffusion region at 13:07:02.25 UT on 16 October 2015. The four MMS spacecraft
 1062 locations are colored diamonds: (black, red, green, blue) are the standard colors for
 1063 (MMS1, 2, 3, 4) respectively. The colored arrows show the projection of the electron flow
 1064 velocity into this LN plane. The purple arrows at each spacecraft show the direction of
 1065 the field and the lengths the relative magnitude of the magnetic field at that location.
 1066

1067 Figure 13 shows the reconstructed magnetic field close to the MMS spacecraft using
 1068 the reduced quadratic model of Denton et al. (2020) at the same time as that plotted in
 1069 Figure 12. Figure 13 shows some interesting features, the sheared field with an X-line
 1070 close to MMS4, the field line of MMS2 approaching the X-line even closer, and the tilt
 1071 of the magnetic island structure toward more positive L at more positive M , suggesting
 1072 that the invariant direction has an L component. Some features are possibly unrealistic.
 1073 For instance, the flux rope in the island might well be larger than Figure 13 suggests. Also,
 1074 some features of the reconstruction are sensitive to details of the reconstruction procedure,
 1075 such as the amount of smoothing and adjustment of the electron density (scaling of the
 1076 electron density from the particle instruments to better agree on average with the current
 1077 density from the curl of the magnetic field, as described by Denton et al. (2020)), so the
 1078 exact field line structure is not known. However, the reconstruction well shows the
 1079 positions of the MMS spacecraft relative to the X line.

1080

t = 2.25 s, Reconstruction B

1081

1082 **Fig. 13** Reduced quadratic reconstruction for 16 October 2015, 13:07:02.25 UT. The
 1083 black, red, green, and blue spheres and curves show the positions and magnetic field lines
 1084 passing through MMS1, 2, 3, and 4, respectively. The gold curves are other magnetic field
 1085 lines with the cones indicating the direction and magnitude.

1086

1087 Another approach to the over-fitting problem is to use the data at multiple times and
 1088 assume that the magnetic topology has not changed over this time interval. The
 1089 assumption is that the spacecraft are moving through a semi-stationary structure. After all,
 1090 this is the essence of what researchers have done in the past to draw cartoons of the
 1091 reconnection regions from time series data over much longer intervals. In producing a
 1092 data-based reconstruction, the velocity of the spacecraft relative to the structure is
 1093 required. This can be estimated from time-of-flight analysis or STD, or found from the
 1094 best fit to the data. The best fit method requires an iterative procedure. For example, for
 1095 the encounter of the EDR seen in Figure 12, Burch et al. (2016b) estimated that over an
 1096 interval of about 0.2s, the spacecraft were moving through the structure with $V_{sc,N} = 45$
 1097 km/s. For a multiple time-step reconstruction, a least-squares fit is required for the 72 data
 1098 elements (24 at 3 times around 13:07:02.25 UT) of the 24-parameter expansion. The
 1099 iterative solution produced a different velocity ($V_{sc,N} = 21$ km/s, while hardly moving in
 1100 the L direction with $V_{sc,L} = 1 \pm 5$ km/s). The reconstruction at an earlier time of
 1101 ~13:07:02.05 UT showed $V_{sc,N} = \sim 55$ km/s, closer to that determined by Burch et al.

1102 (2016b). Research is ongoing into the accuracy of the velocity determined in this way,
1103 but the multiple time-step solution appears to be more stable than the single one.

1104 A reduced quadratic reconstruction using the method of Denton et al. (2022) with
1105 multiple input times (as described above) yields a result similar to that in Figure 13,
1106 except that the field line passing through MMS2 wraps around the magnetic island (not
1107 shown). Differences in the path of this field line are not surprising considering that the
1108 field line passing through MMS2 comes very close to the X-line in Figure 13. A similar
1109 result is found with a complete quadratic reconstruction using the Denton et al. (2022)
1110 method (not shown).

1111

1112 **3.3.2 3D Empirical Reconstruction Using Stochastic Optimization Method**

1113 Zhu et al. (2022) developed a new model for empirical reconstruction of the 3D
1114 magnetic field and current density field using a stochastic optimization method called
1115 simultaneous perturbation stochastic approximation (SPSA) (e.g., Spall 1998; Zhu and
1116 Spall 2002; Spall 2003). The model employs an empirical approach by fitting the
1117 prescribed analytic functions for the magnetic field to the point-wise measurements from
1118 a constellation of spacecraft using physical constraints derived from a set of Maxwell
1119 equations. The fitness of the reconstruction is defined by a general loss function (G),
1120 which consists of both the differences between the model and in-situ measurements and
1121 the model deviations from linear or nonlinear physical constraints. While most
1122 applications of SPSA utilize loss functions that include only the differences between the
1123 modeled and measured quantities (e.g., Chin 1999; Spall 2003), the new model
1124 characterizes the physical robustness of the reconstructed fields. The SPSA approach also
1125 has an additional feature that the algorithm includes the effects of random measurement
1126 errors. Zhu et al. (2022) demonstrated this new model using MMS measurements of the
1127 magnetic field and current density ($\hat{\mathbf{B}}, \hat{\mathbf{j}}$) for the 11 July 2017 magnetotail EDR event
1128 (Torbert et al. 2018), which was previously explored by a least-squares method (e.g.,
1129 Denton et al. 2020; Torbert et al. 2020) introduced in section 3.3.1.

1130 The generalized loss function (G) used in this new empirical reconstruction model has
1131 the form of

$$1132 G = G_O + w_A \varepsilon_A G_A + w_B \varepsilon_B G_B + w_C \varepsilon_C G_C, \quad (4)$$

1133 where the components of the loss function (G_O, G_A, G_B, G_C) are defined as

$$1134 G_O = \frac{1}{12} \sum_{a=1}^4 \sum_{i=1}^3 [B_i(\mathbf{r}_a) - \hat{B}_{a,i}]^2, \quad (5)$$

$$1135 G_A = \frac{1}{12} \sum_{a=1}^4 \sum_{i=1}^3 [j_i(\mathbf{r}_a) - \hat{j}_{a,i}]^2, \quad (6)$$

$$1136 \quad G_B = \frac{1}{9} [\delta^2(\mathbf{r}_0) + \sum_{a=1}^4 \delta^2(\mathbf{r}_a) + \sum_{a=1}^4 \delta^2(\mathbf{r}_{Fa})] \text{ or } G_B^* = \frac{1}{5} [\delta^2(\mathbf{r}_0) + \sum_{a=1}^4 \delta^2(\mathbf{r}_a)],$$

1137 (7) and

$$1138 \quad G_C = \frac{1}{4} \sum_{a=1}^4 [\mu_0 \mathbf{j}(\mathbf{r}_{Fa}) \cdot (\Delta \mathbf{r}_{\beta\gamma} \times \Delta \mathbf{r}_{\beta\delta}) - (\bar{B}_{\beta\gamma} \cdot \Delta \mathbf{r}_{\beta\gamma} + \bar{B}_{\gamma\delta} \cdot \Delta \mathbf{r}_{\gamma\delta} + \bar{B}_{\delta\beta} \cdot \Delta \mathbf{r}_{\delta\beta})]^2.$$

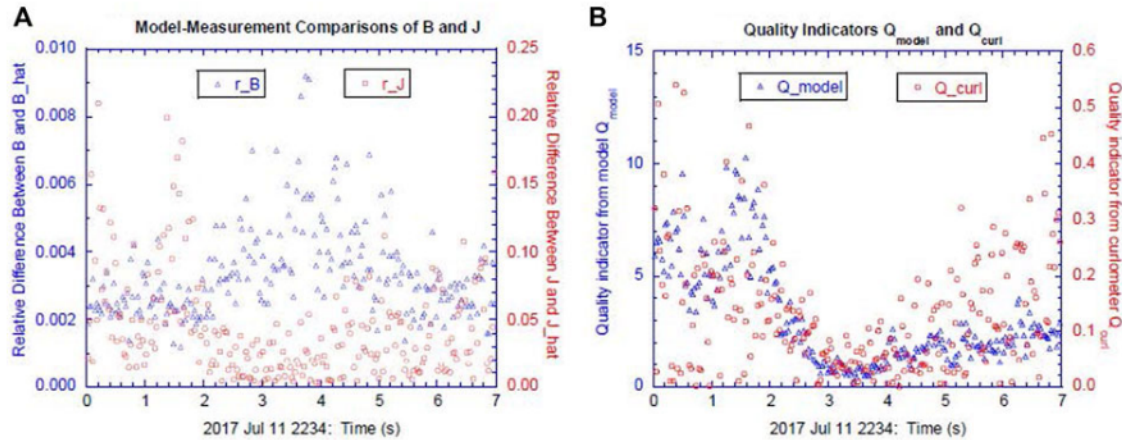
1139 (8)

Here, $\Delta\mathbf{r}_{\beta\gamma} = (\mathbf{r}_\gamma - \mathbf{r}_\beta)$ is the edge vector connecting the vertices \mathbf{r}_β and \mathbf{r}_γ and $\bar{\mathbf{B}}_{\beta\gamma} = (\hat{\mathbf{B}}_\beta + \hat{\mathbf{B}}_\gamma)$ is the mean magnetic field on the edge $\Delta\mathbf{r}_{\beta\gamma}$ calculated using the measured $\hat{\mathbf{B}}$ field by applying a linear approximation between the two spacecraft observations along that edge. G_O and G_A each comprises twelve terms and quantifies the model-measurement difference at each vertex of the tetrahedron (\mathbf{r}_a). G_B comprises nine physical constraints and requires minimization of $\delta^2(\mathbf{r}) = (\nabla \cdot \mathbf{B})^2$ at nine spatial points across the tetrahedron (i.e., the barycenter \mathbf{r}_0 , each of the four vertices \mathbf{r}_a , and the center of each of the four faces \mathbf{r}_{Fa}). The face centers can be disregarded by replacing G_B with G_B^* . G_C comprises four approximate physical constraints derived from applying Stokes' theorem to Ampere's law ($\mu_0 \iint_S \mathbf{j} \cdot d\mathbf{S} = \oint_C \hat{\mathbf{B}} \cdot dl$) on each of the four faces of the tetrahedron; the current density components normal to the tetrahedron faces ($\hat{\mathbf{j}}$) are derived from the curlometer method with the measured $\hat{\mathbf{B}}$. G_C results from minimizing the difference between $\hat{\mathbf{j}}$ and \mathbf{j} projecting onto the normal of each of the four tetrahedron faces. Specification of the weighting factors (w_A, w_B, w_C) in G determines which loss function components are included in the reconstruction. The scaling parameters ($\varepsilon_A, \varepsilon_B, \varepsilon_C$) are dependent on the spatial separations of the four spacecraft and are defined so that the different components of the loss function are of the same order of magnitude. The applied SPSA approach also determines the model parameters that minimize a dimensionless loss function that includes a random perturbation that captures the effects of measurement errors.

Zhu et al. (2022) validated the empirical reconstruction by introducing indices (γ_B, γ_j) defined as the normalized magnitude of the differences between the measured ($\hat{\mathbf{B}}, \hat{\mathbf{j}}$) and modeled (\mathbf{B}, \mathbf{j}) fields. These sets of indices (γ_B, γ_j), shown in Figure 14, provide a qualitative measure of the accuracy to the reconstructed fields. Additionally, a model quality indicator, Q_{model} , is introduced – based on the quality indicator Q_{curl} , which is a measure of the ratio $|\nabla \cdot \hat{\mathbf{B}}|/|\nabla \times \hat{\mathbf{B}}|$, introduced by Dunlop et al. (1988) – to provide a quantitative assessment of the robustness of the modeled field in terms of the physical property of $\nabla \cdot \mathbf{B} = 0$. These indices respectively represent the two sets of constraints applied to the model-measurement differences and the deviations of the model considered when designing the applied generalized loss function. Zhu et al. (2022) examined the

1170 error sources in the reconstructed fields previously noted by studies applying the
 1171 curlometer method and found that these curlometer-calculated errors in the current
 1172 density primarily arose from the application of the linear approximation to what is in
 1173 reality a nonlinear configuration of the 3D magnetic fields.

1174



1175 **Fig. 14** (a) Relative differences (γ_B, γ_j) and (b) quality indicators (Q_{model}, Q_{curl}) for a
 1176 sensitivity run with weighting factors w_B and w_C both set to 0. The very small relative
 1177 difference values ($\ll 1$) highlights that the empirical model results in a very good fit
 1178 between the modeled and measured fields at the prescribed spatial points.

1179

1180 3.3.3 2D Reconstruction of Reconnection Events Assisted by Simulation

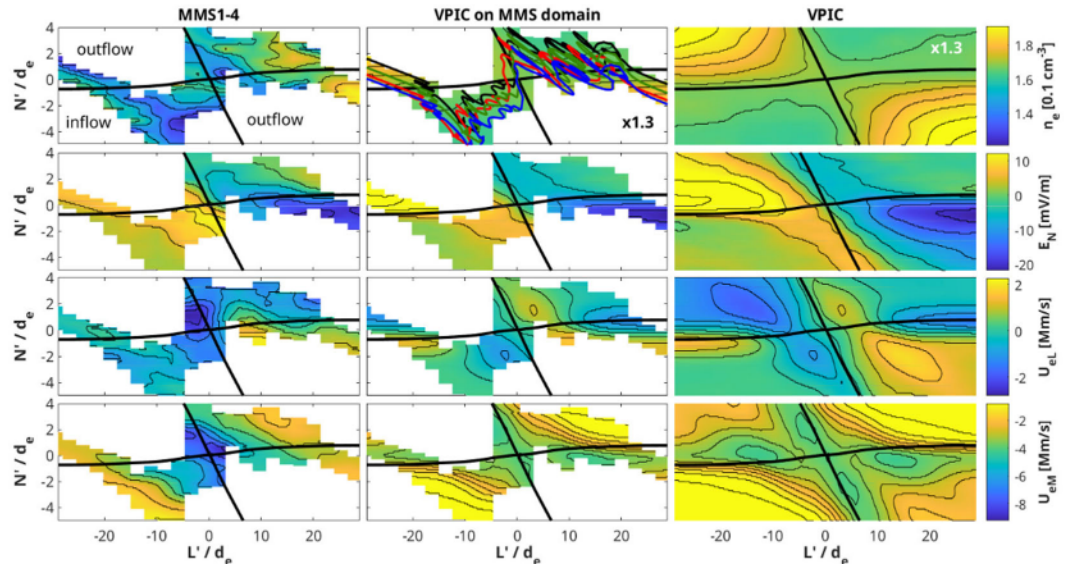
1181 For some spacecraft events a 2D reconstruction can shed light on physics of interest or
 1182 validate models. For an MMS magnetotail reconnection event (on 10 August 2017) shown
 1183 in this section, reconstruction allowed for revealing whether the time series of data is
 1184 consistent with a laminar 2D reconnection geometry or if 3D dynamics are required to
 1185 explain the observations. Here we present an interpolative method that assumes steady-
 1186 state reconnection. For the given event, it allows for reconstruction of a physical area
 1187 extending about $40d_e \times 10d_e$ (where $d_e = c/\omega_{pe}$ is the electron inertial length) around the x-
 1188 line, an area much larger than that allowed in methods that rely on Taylor expansion (section
 1189 3.3.1) or electron magnetohydrodynamics equations (section 3.3.4).

1190 For a given event, once one optimizes spacecraft trajectories parameterized in 2D space
 1191 and time, using the method as introduced in section 3.2.3, the MMS signals can be used to
 1192 construct 2D field maps, as shown in Figure 15. In the event considered here, the trajectories
 1193 closely follow the magnetic separatrix of the reconnection geometry (shown as the nearly
 1194 horizontal thick black curve in Figure 15). There it can be assumed that electron-scale
 1195 gradients are mostly perpendicular to the magnetic separatrix because electrons thermally
 1196 stream along the field lines. Therefore, a grid is defined to have cells elongated

1197 approximately parallel with the separatrix in order to capture variation in signals across the
 1198 topological boundary. To achieve this, the spacecraft trajectories are rotated clockwise by
 1199 an angle $\theta = 17^\circ$ to a coordinate system in which the magnetic separatrix followed by the
 1200 spacecraft becomes nearly horizontal. These rotated coordinates are defined as (L', N') ; the
 1201 L' -coordinate approximately represents the distance along the separatrix, and the N' -
 1202 coordinate approximately represents the distance perpendicular to the separatrix.

1203 Raw MMS data are then distributed spatially according to the optimized spacecraft
 1204 trajectories. Data are placed into spatial bins with lengths $\Delta L' \approx 2d_e$ and $\Delta N' \approx 0.08d_e$,
 1205 such that the aspect ratio of each cell is approximately 25. All bins through which neither
 1206 of the trajectories passes are left as empty cells (NaN values). Thus, each spatial grid cell
 1207 contains data values from all times when either of the MMS spacecraft paths falls within
 1208 its area. The final value for each cell is calculated by a simple average of all data values
 1209 contained in that cell.

1210



1211 **Fig. 15** The left column shows fields measured by MMS constructed into a 2D map
 1212 based on the spacecraft trajectory. The middle column shows PIC simulation data in the
 1213 same region of the reconnection geometry for comparison, while the right column shows
 1214 the simulation data plotted over the entire domain. Adapted from Schroeder et al. (2022).

1215

1216 The particle-in-cell data inherently fills out the entire 2D simulation domain (right
 1217 panels of Figure 15). However, to allow for direct comparison between the
 1218 measurement maps and simulation, the simulation data are binned and averaged on
 1219 the same grid as the spacecraft data (middle column of Figure 15). We note that $\nabla \cdot$
 1220 $\mathbf{B} = 0$ is not guaranteed by this method, because the spacecraft paths are found by the

1221 method discussed in section 3.2.3, so that the measured and thus reconstructed field
1222 values do not strictly agree with the simulation values.

1223

1224 **3.3.4 Grad-Shafranov and Electron Magnetohydrodynamics Reconstruction**

1225 Fundamental equations, such as a set of MHD equations, can be used to reconstruct
1226 steady, 2D structures around the path of an observing spacecraft from in-situ
1227 measurements of the electromagnetic field and plasma. In standard numerical simulations,
1228 a set of equations governing the system is solved as an initial value problem for studying
1229 temporal evolution of the system or physical quantities. This can be done by setting the
1230 initial and boundary conditions at every part of the simulation domain. On the other hand,
1231 the reconstruction as explained below solves a time-independent form of the governing
1232 equation(s) as a spatial initial value problem to get 2D field maps of physical quantities.
1233 This is possible by setting, based on the measurements, the initial conditions at points
1234 along the spacecraft path and solving the equation(s) for spatial development of the
1235 corresponding quantities. The first such method, Grad-Shafranov (GS) reconstruction
1236 technique, was introduced by Sonnerup and Guo (1996), and was further extended to
1237 include MHD (Sonnerup and Teh 2008) and Hall-MHD effects (Sonnerup and Teh 2009).
1238 An overview and reviews of these earlier types of reconstruction were given by Sonnerup
1239 et al. (2006b, 2008) and Hasegawa (2012). Here we describe more recent developments
1240 of the reconstruction techniques along the same line.

1241 For GS reconstruction schemes, in which 2D and steady structures are assumed, one
1242 needs to find a proper or comoving frame of reference in which the structure looks
1243 approximately time-independent, and a reconstruction plane that is perpendicular to the
1244 invariant axis (\hat{z}) along which the structure has negligible spatial gradients. The 2D maps
1245 of plasma and magnetic fields are recovered on that plane. From single spacecraft
1246 observations, the velocity of the proper frame (\mathbf{V}_{str}) can be obtained by the HT analysis
1247 (Khrabrov & Sonnerup 1998; section 3.2.2). If observations from four spacecraft are
1248 available, the STD method (Shi et al. 2006; section 3.2.2) can also be used to determine
1249 the velocity of the structure.

1250 The invariant axis (\hat{z}) can be determined by rotating one of the eigenvectors from
1251 Minimum Variance Analysis (MVA) (Sonnerup and Scheible 1998), taken as a trial
1252 invariant axis, by some angle until measured data points in the parameter plane of a field
1253 line invariant (such as the axial component of the magnetic field B_z and the transverse
1254 pressure $P_t = p + B_z^2/(2\mu_0)$ where p is the plasma pressure) versus partial vector
1255 potential A (out-of-plane component of the vector potential) are approximately expressed
1256 by a single curve, namely, an exponential or polynomial function: $B_z = B_z(A)$ and $P_t =$

1257 $P_t(A)$ (e.g., Hu and Sonnerup 2002). By ingesting multi-spacecraft data, the optimal axis
 1258 could also be found in such a way that the correlation coefficient between the
 1259 reconstructed magnetic fields based on one spacecraft data and the measured magnetic
 1260 fields from other spacecraft reaches the maximum value (Hasegawa et al. 2004). Using
 1261 magnetic field data from four-point measurements, the minimum gradient direction from
 1262 the MDD analysis can be taken as the invariant axis (Shi et al. 2005; section 3.2.1). In
 1263 some cases, the results of MDD and MVA can be combined to provide a reconstruction
 1264 coordinate system, in which not only the invariant axis (parallel to $\hat{\mathbf{e}}_M$) but also the L and
 1265 N axes are properly defined (Denton et al. 2016, 2018; Hasegawa et al. 2017; Tian et al.
 1266 2020; section 3.2.1). The x axis is defined as being antiparallel to the projection of the
 1267 structure velocity \mathbf{V}_{str} onto the plane perpendicular to the invariant axis ($\hat{\mathbf{z}}$), thus
 1268 representing the spacecraft path in the reconstruction (xy) plane. A right-handed
 1269 orthogonal system is formed by $\hat{\mathbf{y}} = \hat{\mathbf{z}} \times \hat{\mathbf{x}}$.

1270 **Grad-Shafranov Reconstruction with pressure anisotropy effects** In collisionless
 1271 plasma there can be pressure anisotropy, that is $p_{\perp} \neq p_{\parallel}$, where p_{\perp} and p_{\parallel} are the
 1272 thermal pressures perpendicular and parallel to the magnetic field, respectively. Taking
 1273 the effects of pressure anisotropy and field aligned flow into account, Sonnerup et al.
 1274 (2006b) derived a new GS equation by considering the double-polytropic energy laws
 1275 (Hau and Sonnerup 1993) $d\{p_{\perp}/(\rho B^{\gamma_{\perp}-1})\}/dt = 0$ and $d(p_{\parallel}B^{\gamma_{\parallel}-1}/\rho^{\gamma_{\parallel}})/dt = 0$,
 1276 where ρ is the mass density, B is the magnetic field strength, γ_{\perp} and γ_{\parallel} are polytropic
 1277 exponents, which can be inferred from observations. Different values of γ_{\perp} and γ_{\parallel}
 1278 represent different thermodynamic conditions (e.g., Hau et al. 2020). Chen and Hau
 1279 (2018) developed a GS code for anisotropic and field-aligned flow for the first time and
 1280 benchmarked it with an analytical model. The application of this code to a magnetopause
 1281 crossing event showed that the recovered magnetic islands inside the magnetopause had
 1282 larger widths than that from the GS reconstruction for isotropic plasma.

1283 There are also some space plasma structures with anisotropic pressure in quasi-static
 1284 equilibrium, such as mirror-mode structures and magnetospheric ultra-low frequency
 1285 compressional waves (drift mirror-mode wave). Tian et al. (2020) reconstructed the
 1286 magnetic field structure of the ultra-low frequency compressional wave by the GS method
 1287 including the pressure anisotropy effect. They call it the reduced GS-like method, because
 1288 the corresponding GS-like equation,

$$1289 \nabla \cdot [(1 - \alpha)\nabla A] = \mu_0 \rho \left[T_{\perp} \frac{dS_{\perp}}{dA} + T_{\parallel} \frac{dS_{\parallel}}{dA} - \frac{dH}{dA} \right] - B_z \frac{dC_z}{dA}, \quad (9)$$

1290 can be derived by removing terms containing the bulk velocity in the equations given by
 1291 Sonnerup et al. (2006b), which contain both the anisotropy and field-aligned flow effects.

1292 Here, $S_{\perp} = c_{v\perp} \cdot \ln(p_{\perp}/\rho B^{\gamma_{\perp}-1})$ and $S_{\parallel} = c_{v\parallel} \cdot \ln(p_{\parallel}B^{\gamma_{\parallel}-1}/\rho^{\gamma_{\parallel}})$ are the
 1293 perpendicular and parallel pseudo entropies, respectively, $H = [p_{\perp}/\{(\gamma_{\perp}-1)\rho\}] +$
 1294 $[\gamma_{\parallel}p_{\parallel}/\{(\gamma_{\parallel}-1)\rho\}]$ is the total enthalpy, $C_z = (1-\alpha)B_z$, $\alpha = (p_{\parallel} - p_{\perp})\mu_0/B^2$ is the
 1295 pressure anisotropy factor, μ_0 is the vacuum permeability, B_z is the magnetic field
 1296 component along the invariant axis, $c_{v\perp} = R/(\gamma_{\perp}-1)$ and $c_{v\parallel} = R/(\gamma_{\parallel}-1)$ with
 1297 the ordinary gas constant $R = c_{p\parallel} - c_{v\parallel}$. All of S_{\perp} , S_{\parallel} , H and C_z are field line
 1298 invariants and are functions of A only. Reduced auxiliary equations,

$$1299 \mathbf{MX}^T = \mathbf{Y}^T, \quad (10)$$

1300 are used to spatially advance quantities α , ρ , p_{\perp} , p_{\parallel} , B_z , B^2 and $\partial^2 A/\partial^2 y$ in y , along
 1301 with spatial integration of A and B_x . Here, the superscript T denotes the matrix
 1302 transpose, and \mathbf{M} is a 7×7 matrix expressed as follows:

$$1303 \mathbf{M} = \begin{bmatrix} \frac{c_{v\perp}}{p_{\perp}} & 0 & -\frac{c_{v\perp}}{\rho} & 0 & -\frac{R}{2B^2} & 0 & 0 \\ 0 & \frac{c_{v\parallel}}{p_{\parallel}} & -\frac{c_{p\parallel}}{\rho} & 0 & \frac{R}{2B^2} & 0 & 0 \\ \frac{c_{v\perp}}{R\rho} & \frac{c_{p\parallel}}{R\rho} & -\frac{(c_{v\perp}p_{\perp}+c_{p\parallel}p_{\parallel})}{R\rho^2} & 0 & 0 & 0 & 0 \\ 0 & 0 & 0 & 1-\alpha & 0 & -B_z & 0 \\ -1 & 1 & 0 & 0 & -\alpha & -B^2 & 0 \\ 0 & 0 & 0 & B_z & -0.5 & 0 & B_x \\ 0 & 0 & 0 & 0 & 0 & \frac{B_x}{\alpha-1} & 1 \end{bmatrix}, \quad (11)$$

$$1304 \mathbf{X} = [\frac{\partial p_{\perp}}{\partial y}, \frac{\partial p_{\parallel}}{\partial y}, \frac{\partial \rho}{\partial y}, \frac{\partial B_z}{\partial y}, \frac{\partial B^2}{\partial y}, \frac{\partial \alpha}{\partial y}, \frac{\partial^2 A}{\partial y^2}], \quad (12)$$

$$1305 \mathbf{Y} = [B_x \frac{dS_{\perp}}{dA}, B_x \frac{dS_{\parallel}}{dA}, B_x \frac{dH}{dA}, B_x \frac{dC_z}{dA}, B_y \frac{\partial B_x}{\partial x}, \frac{Q}{1-\alpha}], \quad (13)$$

1306 where Q in \mathbf{Y} is $\text{RHS} - \partial[(1-\alpha)\partial A/\partial x]/\partial x$, and RHS is the right-hand side quantity in
 1307 Eq (9). One difficulty in this method exists in determining the proper polytropic
 1308 exponents γ_{\perp} and γ_{\parallel} . Hau et al. (2020) inferred these parameters by using the measured
 1309 magnetosheath data, and recovered the 2D topology of a mirror-mode structure observed
 1310 in the magnetosheath.

1311 Aiming at reconstruction of anisotropic plasma structures, Teh (2019) developed
 1312 another simple extended GS equation. He did not use the double polytropic energy laws,
 1313 but assumed that parameters α , p_{\perp} , and p_{\parallel} are functions of the magnetic field strength
 1314 B only to derive a relatively simple GS-like equation. This assumption might not be valid.
 1315 Nevertheless, basic features of magnetic mirror-mode and flux rope with pressure
 1316 anisotropy were revealed by this extended GS solver (Teh 2019; Teh and Zenitani 2020).

1318 magnetohydrodynamics (EMHD) reconstruction is a single-spacecraft method for the
 1319 reconstruction of steady, 2D electromagnetic fields and electron streamlines in regions
 1320 where ions are fully demagnetized and thus electron dynamics dominates. It was
 1321 developed to recover the field geometry in and around the EDR of magnetic reconnection,
 1322 where electrons are demagnetized. The original version (Sonnerup et al., 2016) is based
 1323 on an inertia-less and time-independent form of the electron MHD equation (Kingsep et
 1324 al. 1990 and references therein) and assumes uniform electron density (electron
 1325 incompressibility) and temperature. A recent version incorporates electron inertia effects
 1326 in the streamline reconstruction, and the effects of nonuniform density and temperature
 1327 and a guide magnetic field component B_z in the reconnection region (Hasegawa et al.
 1328 2021). The density and temperature are, however, assumed to be preserved along the
 1329 magnetic field lines, because such assumptions are roughly satisfied around the EDR of
 1330 symmetric, antiparallel reconnection (Korovinskiy et al. 2020). These conditions are not
 1331 well satisfied for guide-field or asymmetric reconnection; therefore, further model
 1332 developments are needed. Nonetheless, under the above assumptions, the magnetic field
 1333 can be reconstructed by use of a Grad-Shafranov-type equation

$$\nabla^2 A = -\mu_0 j_z(A) = \mu_0 e n_e(A) u_{ez}(A). \quad (14)$$

1334 Reconstruction of the EDR requires some kind of dissipation term and, for antiparallel
 1335 reconnection, makes use of a term corresponding to the component of the divergence of
 1336 the electron pressure tensor \mathbf{P} in the direction $\hat{\mathbf{z}}$ of reconnection electric field (or X-
 1337 line) (see review by Hesse et al. (2011))

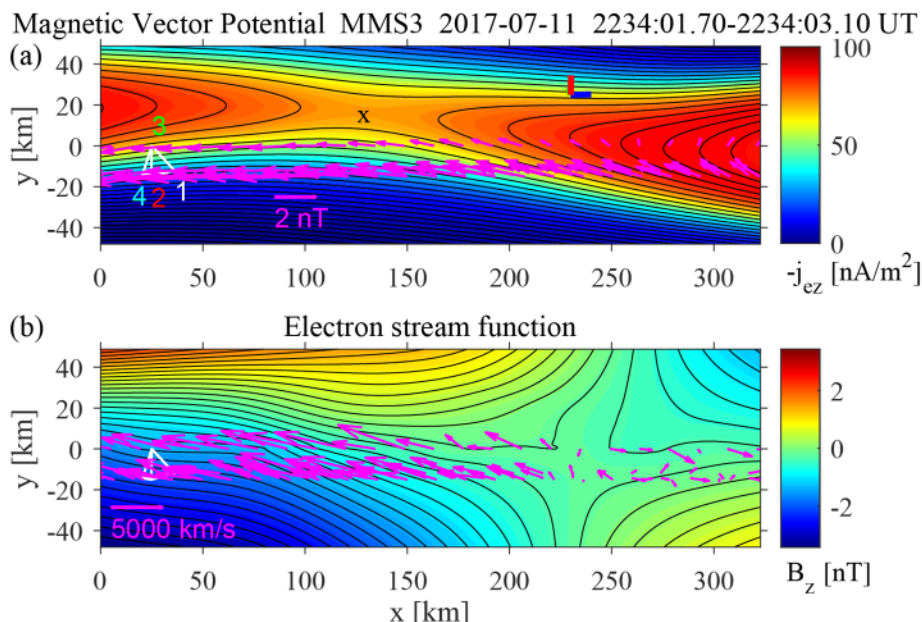
$$(\nabla \cdot \mathbf{P}) \cdot \hat{\mathbf{z}} = n_e \sqrt{2m_e k_B T_e} \frac{\partial u_{eL}}{\partial L}. \quad (15)$$

1338 In the case of guide-field reconnection, see Hasegawa et al. (2021) for some recipes. The
 1339 reconstruction is performed in the rest frame of magnetic field structures, as introduced
 1340 in the second paragraph of section 3.3.4.

1341 Figure 16 shows 2D maps of the magnetic field and electron streamlines from the
 1342 EMHD reconstruction with electron inertia effects for the magnetotail EDR event on 11
 1343 July 2017, first reported by Torbert et al. (2018). Magnetic field, electric field, and
 1344 electron moment data taken by the MMS3 spacecraft, which made the closest approach
 1345 to the X-line, are used to set the initial conditions on the x axis. The final frame velocity
 1346 was determined by a multi-spacecraft method (Hasegawa et al. 2017), in which the
 1347 correlation coefficient is maximized between the components of the magnetic fields and
 1348 electron velocities measured by the three spacecraft (MMS1, MMS2, and MMS4) not
 1349 used as input and those predicted from the maps along the spacecraft paths. The final z
 1350 axis was optimized by a method based on the y component of a time-independent and 2D
 1351

1353 form of Ampère's law, $-\partial B_z / \partial x = \mu_0 j_y$; when the z axis is properly chosen, this
 1354 relation approximately holds for the particle current density and magnetic field data taken
 1355 along the spacecraft path (x axis) (Hasegawa et al. 2019).

1356 Figure 16a shows a clear X-type magnetic field geometry, as seen in simulations. We
 1357 note that the information on the separatrix opening angle gained from the reconstructed
 1358 field map, as seen in Figure 16a, can be used to estimate the reconnection electric field
 1359 by a method explained in section 4.3.3. Figure 16b essentially shows expected patterns
 1360 of electron inflow and outflow and corresponding Hall magnetic fields B_z . Interestingly,
 1361 the electron stagnation point is displaced in the earthward (outflow) direction by $\sim 3d_e$
 1362 ($d_e \sim 27$ km/s) from the X-point, a new feature revealed by the reconstruction. The
 1363 method has also been successfully applied to an EDR of magnetopause reconnection
 1364 (Hasegawa et al. 2017) and an ion-scale magnetic flux rope in the magnetopause current
 1365 sheet (Hasegawa et al. 2023).



1367
 1368 **Fig. 16** 2D maps of the magnetic field (a) and electron streamlines (b) from the EMHD
 1369 reconstruction applied to data from the magnetotail EDR encounter by MMS3 on 11 July
 1370 2017. The arrows show the projection onto the reconstruction plane of the measured
 1371 magnetic fields (a) and electron velocities in the structure-rest frame (b). The axial current
 1372 density (a) and axial magnetic field component (b) are shown in color. The blue and red
 1373 bars in Figure 16 are the projection of the GSM x and z axes, respectively. Adapted from
 1374 Hasegawa et al. (2021).
 1375

1377 approach to the EMHD GS reconstruction of EDR is represented by the MMS-tailored
 1378 model, introduced by Korovinskiy et al. (2021). Adopting an assumption of steady-state
 1379 two-dimensional magnetoplasma configuration and assuming additionally the uniform
 1380 number density n , the problem is reduced to calculation of two quantities: the magnetic
 1381 potential A of the in-plane magnetic field and the out-of-plane magnetic field component
 1382 B_z . The out-of-plane component of Ampère's law makes the magnetic potential to obey
 1383 the equation,

$$1384 \quad \nabla^2 A = \mu_0 e n u_{ez}, \quad (16)$$

1385 where the right-hand side is represented, in general, by a function of two variables
 1386 (contrary to Eq. (14)). Then, with neglected ion current and $\partial/\partial z = 0$, the in-plane
 1387 components of Ampère's law reveal that the quantity $-B_z/(\mu_0 e)$ serves as a stream
 1388 function for the in-plane electron flow $n\mathbf{u}_{e\perp} = (nu_{ex}, nu_{ey})$: $\mu_0 e n u_{ex} = -\partial B_z / \partial y$
 1389 and $\mu_0 e n u_{ey} = +\partial B_z / \partial x$. With uniform number density, this yields the equation for
 1390 B_z ,

$$1391 \quad \nabla^2 B_z = \mu_0 e n (\partial u_{ey} / \partial x - \partial u_{ex} / \partial y) = Q. \quad (17)$$

1392 Here, the model function Q represents the contribution of the electron inertia and
 1393 anisotropy (see Eq. 14–16 of Korovinskiy et al. 2021).

1394 Since the Jacobian of a variable transform $(x, y) \rightarrow (A, B_z)$ may turn to zero or
 1395 infinity at a manifold of Lebesgue measure zero only (see Eq. 9 of Korovinskiy et al.
 1396 (2021)), the right-hand sides of Eqs. (16,17) can be considered as the functions of (A, B_z) .
 1397 Assuming that Cartesian coordinates correspond to the local co-moving LMN coordinate
 1398 system (e.g., Denton et al. 2018), where the x axis coincides with $\hat{\mathbf{e}}_L$ and the y axis
 1399 coincides with $\hat{\mathbf{e}}_N$, one can note that the stretched configuration of EDR, dictated by a
 1400 low reconnection rate $\varepsilon \sim 0.1$ (e.g., Liu et al. 2017), brings the ratio $\partial/\partial x \ll \partial/\partial y$. The
 1401 analogous scaling ratio $\partial/\partial B_z \ll \partial/\partial A$ (see, e.g., Eqs. 12 and 13 of Korovinskiy et al.
 1402 (2021)) is valid in the variable space (A, B_z) . Omitting the minor dependence on B_z , one
 1403 can consider the zeroth-order reconstruction model, where the model functions depend
 1404 on A only. This way Eq. (16) turns into the Grad-Shafranov equation (14) and in Eq.
 1405 (17) we have $Q = Q(A)$. Notably, under this equality the mathematical self-consistency
 1406 of the solution demands an extra term $\sim B_z$ on the right-hand side of Eq. (16); however,
 1407 the contribution of this term is found to be negligible (see Eq. 21 and Fig. 7 of
 1408 Korovinskiy et al. 2021), so it can be omitted.

1409 The model functions $u_{ez}(A)$ and $Q(A)$ are evaluated from the boundary conditions.
 1410 Particularly, the latter is calculated by using the data of the four MMS probes. Thus, the
 1411 reconstruction model development is completed and the only problem left is the solution
 1412 of the ill-posed problem, stated by Eq. (16,17), with the boundary conditions specified

1413 along the probe trajectory. In an approach discussed by Korovinskiy et al. (2020), the
1414 problem regularization was performed by utilizing the so-called boundary layer
1415 approximation (BLA) (Schlichting 1979). Namely, the second-order small terms
1416 $\partial^2/\partial x^2 \sim \varepsilon^2 \partial^2/\partial y^2$ are omitted, reducing the problem to the system of ordinary
1417 differential equations of the second order. To benefit from the simplicity of this method,
1418 the local LMN coordinate system must be accurately determined. Besides that, this
1419 method is less universal, as it is not applicable to EDR crossings in the direction normal
1420 to the current sheet.

1421 The described model, named ‘Model 2’ in Korovinskiy et al. (2021), was tested by
1422 reconstruction of the MMS event on 11 July 2017 (Torbert et al. 2018). The advantages
1423 of this model are the following. First, it does not depend on the out-of-plane electric field
1424 E_z , which is assumed to be constant, while in reality it may be considerably oscillating
1425 (see Fig. 2a in Korovinskiy et al. (2021)). The nonuniformity of E_z brings appreciable
1426 uncertainty to the reconstruction results obtained by utilizing Eq. (15), representing the
1427 approximation derived by Hesse et al. (1999) for the electron pressure anisotropy (see
1428 ‘Model 3’ of Korovinskiy et al. (2021)). Since this approximation is not used,
1429 reconstruction errors, which can appear due to its possible inaccuracy (see Fig. 2 in
1430 Korovinskiy et al. (2020), and the corresponding discussion), are also eliminated. Second,
1431 with BLA the model allows evaluation of the small terms B_y and u_{ey} , but these
1432 quantities do not affect other computations, particularly, the computation of B_z and u_{ex} .
1433 This property brings advantage when the translational symmetry of the configuration is
1434 corrupted, since in this case $\partial B_x/\partial z \neq 0$, and hence the formula $\mu_0 e n u_{ey} = \partial B_z/\partial x$,
1435 used in the two-dimensional models, fails.

1436 Thus, the major advantages of the discussed MMS-tailored technique consist in its
1437 comparative simplicity and increased accuracy due to the reduced sensitivity to violations
1438 of the ideal theoretical conditions. This is achieved at the expense of the lost universality,
1439 since the model requires current sheet crossing in the direction with a nonzero angle with
1440 respect to $\hat{\mathbf{e}}_N$ and multi-spacecraft data for evaluating the model function Q . The major
1441 disadvantage – the assumption of uniform number density, which limits the model
1442 applicability to the internal EDR – can be relaxed by substituting $n = n(A)$ in Eqs.
1443 12–16 of Korovinskiy et al. (2021). Another limitation is related to the adopted
1444 assumption of a not-too-small guide field value. For a case of small or zero guide field,
1445 the corresponding (rather straightforward) modifications are required; in particular, the
1446 symmetry considerations demand $Q = Q(A, B_z)$, while the zeroth-order model equation
1447 $j_{ez} = j_{ez}(A)$ stays unchanged. The extended compressible model and discussion of the
1448 ways to further improve the EMHD GS reconstruction technique can be found in

1449 Korovinskiy et al. (2023).

1450

1451 **3.3.5 3D Field Reconstruction Using Modified Radial Basis Functions**

1452 Another method for the reconstruction of 3D local magnetic field structures is based
1453 on the use of toroidal and poloidal magnetic potentials that are expressed as linear
1454 combinations of radial basis functions (e.g., Buhmann, 2003). In this approach, the
1455 magnetic field is represented by

1456
$$\mathbf{B} = \nabla \times \left(\frac{\psi_1}{r} \mathbf{r} \right) + \nabla \times \nabla \times (\psi_2 \mathbf{r}), \quad (18)$$

1457 where ψ_1 and ψ_2 are the toroidal and poloidal potentials, respectively. Instead of using
1458 orthogonal basis functions, the potentials are individually expanded into a series $\psi_j =$
1459 $\sum_i \alpha_{ji} \chi_i$ of a modified form of radial basis functions (Andreeva and Tsyganenko 2016;
1460 Tsyganenko and Andreeva 2016)

1461
$$\chi_i(\mathbf{r}; D, \mathbf{L}) = \left\{ \left(\frac{x - R_{i,x}}{L_x} \right)^2 + \left(\frac{y - R_{i,y}}{L_y} \right)^2 + \left(\frac{z - R_{i,z}}{L_z} \right)^2 + D^2 \right\}^{1/2}. \quad (19)$$

1462 Here, the vectors \mathbf{R}_i are coordinates of meshwork grid nodes, $\mathbf{L} = \{L_x, L_y, L_z\}$ a
1463 characteristic length set equal to the node separation along each axis, and D an
1464 adjustable regularization parameter. An advantage of the magnetic field thus defined is its
1465 divergence-free nature (Stern 1976). The expansion coefficients $\{\alpha_i\}$ can be determined
1466 by optimally fitting to magnetic field data taken by multiple spacecraft, such as Cluster
1467 and MMS, for a time interval.

1468 Chen et al. (2019) tested this technique for 2D and 3D model magnetic fields, and
1469 applied it to magnetic field data from the Cluster mission. The structure velocity relative
1470 to the spacecraft was treated as a hyper parameter, and was tuned by minimizing the
1471 average magnitude of an error vector field $\Delta \mathbf{B} \equiv \mathbf{B}_{\text{data}} - \mathbf{B}_{\text{rec}}$, where \mathbf{B}_{data} and \mathbf{B}_{rec}
1472 are the measured and reconstructed magnetic field vectors, respectively. Their study
1473 suggests that the method can be used to identify and investigate the properties of
1474 characteristic structures in 3D magnetic reconnection, including magnetic nulls (section
1475 4.1.7) and separator lines.

1476

1477 **4 Detection and Analysis of In-Situ Observations of the Diffusion Regions**

1478 This section mostly focuses on the methods for detecting and analyzing in-situ
1479 observations of the electron diffusion region (EDR). See Phan et al. (2005) for a brief
1480 review of in-situ observations and analysis of ion diffusion regions (IDRs) with effects of
1481 the Hall term in the generalized Ohm's law.

1482 **4.1 Diffusion Region Identification**

This section reviews several measures that can be used to identify the diffusion region or nearby regions. We stress that none of the following measures are uniquely non-zero or significant only in the diffusion region, and that none of them by themselves necessarily identify “dissipation” in the sense of an irreversible process, although some are conventionally called a dissipation measure or have been used to identify the region where a process leading to entropy increase may occur. Therefore, one should use these measures in the context of other measurements of the reconnection process to identify a candidate diffusion region; the candidate may or may not turn out to be an actual diffusion region after full quantitative analysis to make sure whether other reconnection and diffusion region signatures are observed.

4.1.1 Plasma-Frame Dissipation Measure

Since magnetic reconnection converts electromagnetic field energy to plasma kinetic energy, we expect the energy conversion rate $\mathbf{j} \cdot \mathbf{E}$ or its variants ($\mathbf{j}_i \cdot \mathbf{E}$ and $\mathbf{j}_e \cdot \mathbf{E}$) to be significant in magnetic reconnection. These quantities are important, but may not be useful to identify the EDR because they can be nonzero even in ideal regions (see Eq. (31) below).

One problem is that $\mathbf{j} \cdot \mathbf{E}$ is measured in the stationary or observer’s (laboratory) frame; if the EDR is moving, it might be better to evaluate $\mathbf{j} \cdot \mathbf{E}$ in a particular frame. Starting from this, we consider the energy conversion in a moving frame that travels at a velocity \mathbf{V}_r . In this reference frame, the electric current density and the electric field are given by

$$\mathbf{j}' = \mathbf{j}'(\mathbf{V}_r) = \mathbf{j} - \rho_c \mathbf{V}_r, \quad (20)$$

$$\mathbf{E}' = \mathbf{E}'(\mathbf{V}_r) = \mathbf{E} + \mathbf{V}_r \times \mathbf{B}, \quad (21)$$

where ρ_c is the charge density and the primed quantities denotes those in the moving frame. The energy conversion rate in the \mathbf{V}_r -moving frame yields

$$D_r = D(\mathbf{V}_r) \equiv \mathbf{j}' \cdot \mathbf{E}' = \mathbf{j} \cdot (\mathbf{E} + \mathbf{V}_r \times \mathbf{B}) - \rho_c (\mathbf{V}_r \cdot \mathbf{E}). \quad (22)$$

Here, the reference velocity is arbitrary, so we call Eq. (22) the frame-independent dissipation measure. Employing the electron fluid velocity as the reference velocity, we define the electron-frame dissipation measure $D_e = D(\mathbf{u}_e)$, and employing the ion fluid velocity, we obtain the ion-frame dissipation measure $D_i = D(\mathbf{u}_i)$.

Importantly, these measures are Galilean invariants, in other words, frame-independent. By using the Lorentz factor $\gamma_r = [1 - (V_r/c)^2]^{1/2}$, we obtain a Lorentz invariant form (Zenitani et al., 2011a)

$$D_r = \gamma_r [\mathbf{j} \cdot (\mathbf{E} + \mathbf{V}_r \times \mathbf{B}) - \rho_c (\mathbf{V}_r \cdot \mathbf{E})]. \quad (23)$$

It is seen that as long as we choose a unique reference velocity \mathbf{V}_r , Eq. (23) always gives the same result regardless of the observer’s velocity or direction.

Let us discuss properties of the dissipation measures. We focus on the nonrelativistic limit of $\gamma_r \rightarrow 1$ for simplicity. In a plasma, the charge density and the electric current density are

$$\rho_c = \sum_s q_s n_s, \quad \mathbf{j} = \sum_s q_s n_s \mathbf{u}_s, \quad (24)$$

where s denotes the plasma species. We consider a charge-weighted sum of Eq. (21)

$$\sum_s q_s n_s \mathbf{E}'(\mathbf{u}_s) = \rho_c \mathbf{E} + \mathbf{j} \times \mathbf{B}. \quad (25)$$

Applying $\mathbf{j} \cdot$ to both sides, and using Eq. (24), we obtain

$$\mathbf{j} \cdot \sum_s q_s n_s \mathbf{E}'(\mathbf{u}_s) = \rho_c \mathbf{j} \cdot \mathbf{E} = \rho_c (\sum_s q_s n_s \mathbf{u}_s) \cdot \mathbf{E}, \quad (26)$$

$$\sum_s q_s n_s (\mathbf{j} \cdot \mathbf{E}' - \rho_c \mathbf{u}_s \cdot \mathbf{E}) = 0. \quad (27)$$

This provides a useful relation

$$\sum_s q_s n_s D_s = 0. \quad (28)$$

Next we consider the relevance to resistive MHD. We define the MHD quantities,

$$\rho_{\text{mhd}} \equiv \sum_s m_s n_s, \quad \mathbf{u}_{\text{mhd}} \equiv \frac{\sum_s m_s n_s \mathbf{u}_s}{\sum_s m_s n_s} = \frac{\sum_s m_s n_s \mathbf{u}_s}{\rho_{\text{mhd}}}. \quad (29)$$

Since Eq. (22) only uses linear operators, we obtain

$$D_{\text{mhd}} = D(\mathbf{u}_{\text{mhd}}) = D\left(\frac{\sum_s m_s n_s \mathbf{u}_s}{\rho_{\text{mhd}}}\right) = \frac{\sum_s m_s n_s D(\mathbf{u}_s)}{\rho_{\text{mhd}}} = \frac{\sum_s m_s n_s D_s}{\rho_{\text{mhd}}}. \quad (30)$$

From the Ohm's law, we obtain the energy conversion rate

$$\mathbf{E} + \mathbf{u}_{\text{mhd}} \times \mathbf{B} = \eta \mathbf{j}, \quad \mathbf{j} \cdot \mathbf{E} = (\mathbf{j} \times \mathbf{B}) \cdot \mathbf{u}_{\text{mhd}} + \eta j^2. \quad (31)$$

Rearranging the MHD-frame dissipation $D_{\text{mhd}} = D(\mathbf{u}_{\text{mhd}})$, we immediately obtain from Eq. (22)

$$\mathbf{j} \cdot \mathbf{E} = (\mathbf{j} \times \mathbf{B} + \rho_c \mathbf{E}) \cdot \mathbf{u}_{\text{mhd}} + D_{\text{mhd}}. \quad (32)$$

In a quasineutral ion-electron plasma, from Eqs. (28) and (30), we obtain

$$D_{\text{mhd}} \approx D_i \approx D_e. \quad (33)$$

From Eqs. (31) and (32) and considering that ρ_c is negligible in MHD, we see that the D_{mhd} term ($\approx D_e$) plays the same role as the nonideal energy conversion rate ηj^2 .

PIC simulations have revealed that $D_e > 0$ marks a compact physically-significant region surrounding the X-line (Zenitani et al. 2011a). Although the resolution was limited and it was only partially evaluated, Zenitani et al. (2012) reported $D_e > 0$ during a magnetotail reconnection event observed by the Geotail spacecraft (Nagai et al. 2011). Recent observations by MMS unambiguously reported $D_e > 0$ near the EDR (Burch et al. 2016b; Phan et al. 2018; Torbert et al. 2018). Based on these results, it is fair to say that $D_e > 0$ is an important signature of the EDR.

We raise unsolved issues here. First, there is often a weakly negative region of $D_e < 0$ in the downstream side of the EDR, where the electrons outrun the $\mathbf{E} \times \mathbf{B}$ velocity (Karimabadi et al. 2007; Nakamura et al. 2018b; Pritchett 2001; Shay et al. 2007). We

1553 often see $D_e < 0$ at the jet termination region where the reconnected magnetic field is
1554 compressed (Payne et al. 2021), while $D_e \lesssim 0$ is also seen inside the elongated electron
1555 jet (Zenitani et al. 2011b). By clarifying the underlying mechanisms, we may be able to
1556 predict the negative amplitude of D_e . Second, one can split the electron-frame measure
1557 into its perpendicular and parallel contributions, $D_e = \mathbf{j}' \cdot \mathbf{E}' \approx \mathbf{j}_\perp \cdot \mathbf{E}'_\perp + j_\parallel E_\parallel$. Inside the
1558 EDR, we expect that electron meandering motion provides $\mathbf{j}_\perp \cdot \mathbf{E}'_\perp > 0$ in antiparallel
1559 reconnection, and that the electron parallel motion leads to $j_\parallel E_\parallel > 0$ in guide-field
1560 reconnection. Wilder et al. (2018) evaluated the energy conversion rate $\mathbf{j} \cdot \mathbf{E}' = \mathbf{j}_\perp \cdot \mathbf{E}'_\perp +$
1561 $j_\parallel E_\parallel$ in the diffusion regions for multiple reconnection events seen by MMS. They
1562 organized the results as a function of the guide-field amplitude B_g/B_0 , and reported that
1563 the perpendicular contribution is dominant in the antiparallel cases ($B_g/B_0 \leq 0.3$) while
1564 the parallel contribution is dominant in the guide-field cases ($B_g/B_0 \geq 0.3$) (Figure 10 in
1565 Wilder et al. (2018)). However, the critical guide field between the two regimes has not
1566 been addressed before, theoretically or numerically. Further research is thus necessary to
1567 make a quantitative discussion. Third, strictly speaking, the term “dissipation” is
1568 ambiguously used in this section, because these measures do not always lead to an
1569 irreversible energy conversion in a collisionless plasma. Connection between the
1570 dissipation measures and a true irreversible dissipation process needs to be clarified. This
1571 might be better understood from the viewpoint of the entropy production in a kinetic
1572 plasma (Liang et al. 2019; Section 4.2.4).

1573

1574 **4.1.2 Agyrotropy**

1575 Due to their small Larmor radii and short gyroperiods, electrons are closely tied to the
1576 magnetic field, much more so than heavier ions. As a result, they efficiently probe the
1577 field’s structure so that locations of topological interest, such as reconnection X-lines and
1578 magnetic separatrices, should leave signatures in electron distribution functions.
1579 Vasyliunas (1975) identified one such signature by noting that for reconnection to occur,
1580 the electron pressure tensor must be non-gyrotropic at the X-point. Spacecraft
1581 measurements of non-gyrotropic electron distributions can hence be used as a measure of
1582 the proximity to the X-point.

1583 Other authors (Scudder and Daughton 2008; Aunai et al. 2013) have proposed
1584 quantifications of agyrotropy, but the version discussed here follows the presentation in
1585 Swisdak (2016). A pressure tensor in a field-aligned coordinate system can always be put
1586 in the form

1587
$$\mathbf{P} = \begin{pmatrix} P_{\parallel} & P_{12} & P_{13} \\ P_{12} & P_{\perp} & P_{23} \\ P_{13} & P_{23} & P_{\perp} \end{pmatrix}, \quad (34)$$

1588 where P_{\parallel} and P_{\perp} represent the pressure parallel and perpendicular to the field,
 1589 respectively.

1590 In the gyrotropic case the off-diagonal components vanish; measures of agyrotropy
 1591 attempt to quantify the size of these components relative to the diagonal ones. Pressure
 1592 tensors are positive semidefinite (i.e., have non-negative eigenvalues) and thus satisfy the
 1593 inequalities

1594
$$P_{12}^2 \leq P_{\parallel}P_{\perp}, \quad P_{13}^2 \leq P_{\parallel}P_{\perp}, \quad P_{23}^2 \leq P_{\perp}^2, \quad (35)$$

1595 which leads to a natural definition of a gyrotropy parameter

1596
$$Q = \frac{P_{12}^2 + P_{13}^2 + P_{23}^2}{P_{\perp}^2 + 2P_{\perp}P_{\parallel}}. \quad (36)$$

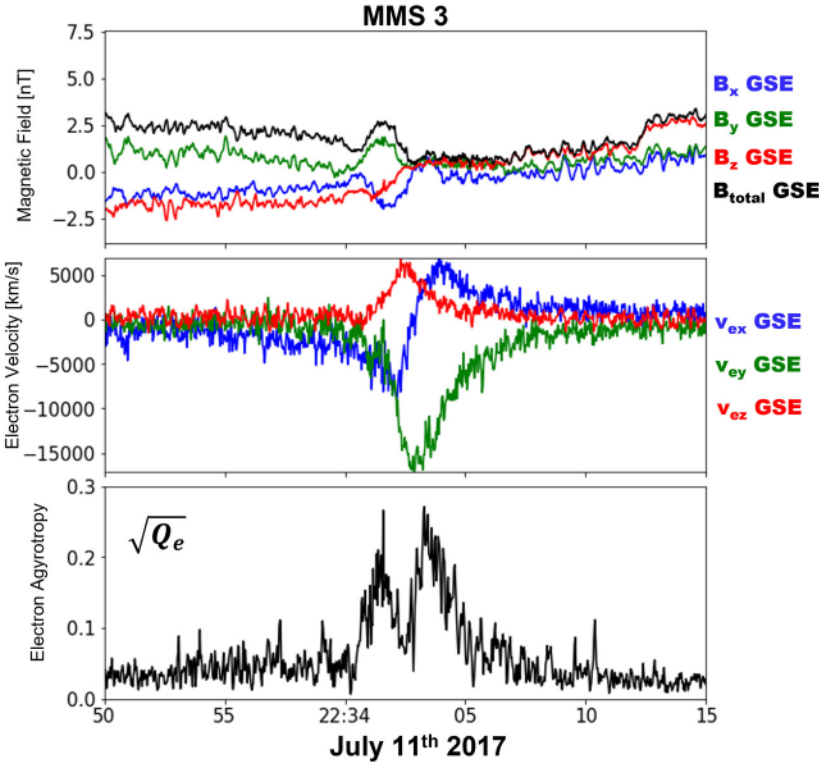
1597 For gyrotropic distributions $Q = 0$, while maximally agyrotropy occurs when $Q = 1$.
 1598 By using certain rotationally invariant quantities it is possible to calculate Q while in
 1599 any coordinate system (i.e., the pressure tensor needs not be in the form of Eq. (34)):

1600
$$Q = 1 - \frac{4I_2}{(I_1 - P_{\parallel})(I_1 + 3P_{\parallel})}. \quad (37)$$

1601 The necessary factors are the trace, $I_1 = P_{xx} + P_{yy} + P_{zz}$, the sum of principal minors,
 1602 $I_2 = P_{xx}P_{yy} + P_{xx}P_{zz} + P_{yy}P_{zz} - (P_{xy}^2 + P_{xz}^2 + P_{yz}^2)$, and the parallel pressure $P_{\parallel} = \hat{\mathbf{b}} \cdot$
 1603 $\mathbf{P} \cdot \hat{\mathbf{b}} = b_x^2 P_{xx} + b_y^2 P_{yy} + b_z^2 P_{zz} + 2(b_x b_y P_{xy} + b_x b_z P_{xz} + b_y b_z P_{yz})$. Here $\hat{\mathbf{b}}$ is the unit
 1604 vector aligned with the magnetic field.

1605 Figure 17 shows MMS data from a well known crossing of an EDR (Torbert et al.
 1606 2018) in the magnetotail with a small guide field (B_y component). The top two panels,
 1607 which show the components of the magnetic field and the electron velocity, respectively,
 1608 exhibit the expected signatures of an EDR crossing: a null in B_x associated with a
 1609 minimum in B and a divergence or reversal in u_{ex} . Within the EDR $\sqrt{Q_e}$ rises sharply
 1610 from its background value of ≈ 0.05 to a peak of ≈ 0.25 . The bifurcated structure in \sqrt{Q}
 1611 has been seen in PIC simulations of antiparallel reconnection (Swisdak et al. 2016).
 1612 Calculations of Q_i (not shown) exhibit a much broader peak, as expected, since ions
 1613 decouple from the magnetic field, and hence can acquire non-gyrotropic distribution
 1614 functions on the much larger scales of the IDR.

1615



1616

1617 **Fig. 17** Magnetospheric Multiscale (MMS) spacecraft 3 observations of an electron
 1618 diffusion region at 2233:50-2234:15 UT on 11 July 2017. The top panel shows the
 1619 three components and the strength of the magnetic field in geocentric solar ecliptic
 1620 (GSE) coordinates (B_x , blue; B_y , green; B_z , red; and $|\mathbf{B}|$, black). The second panel
 1621 shows the components of the electron velocity in the same color scheme. The
 1622 final panel shows $\sqrt{Q_e}$.

1623

1624 We note that non-gyrotropic electron velocity distributions are not a unique
 1625 signature of magnetic reconnection or the EDR; they have been observed at a non-
 1626 reconnecting magnetopause current sheet (Tang et al. 2019).

1627

1628 **4.1.3 Pressure-Strain Interaction in Reconnection Diffusion Region**

1629 Energy conversion in magnetic reconnection is a topic of fundamental importance.
 1630 Several energy conversion measures, such as the Zenitani measure (Zenitani et al. 2011;
 1631 section 4.1.1), have been used to evaluate energy conversion at the reconnection site.
 1632 Recent studies have revealed the role of pressure-strain interaction in the conversion of
 1633 bulk kinetic energy to the random (or thermal, or internal) component in collisionless
 1634 plasmas (Cerri 2016; Yang et al. 2017; Fadanelli et al. 2021). Here, we show the
 1635 evaluation of pressure-strain interaction near reconnection X-lines and discuss related

interpretations (Bandyopadhyay et al. 2021).

The equation of the thermal or random energy density E_α^{th} , computed from the moments of the Vlasov equations, is given by

$$\partial E_\alpha^{\text{th}} / \partial t + \nabla \cdot (E_\alpha^{\text{th}} \mathbf{u}_\alpha + \mathbf{h}_\alpha) = -(\mathbf{P}_\alpha \cdot \nabla) \cdot \mathbf{u}_\alpha, \quad (38)$$

where α indicates a specific charged species, \mathbf{u}_α is the fluid velocity, \mathbf{P}_α is the pressure tensor, $E_\alpha^{\text{th}} = 3p^{(\alpha)}/2 = P_{ii}^{(\alpha)}/2$ with $P_{ii}^{(\alpha)}$ as the trace of the pressure tensor, and \mathbf{h}_α is the heat flux.

When integrated over a closed domain, the terms on the left-hand side within the divergence operator average to zero. Therefore, these may be interpreted as transport terms that do not contribute to net change in the form of energy but simply move energy from one location to another spatially. However, if we are concerned with quantifying conversion between different kinds of energy instead of transport, we see that the quantity on the right-hand side is responsible for the conversion of bulk kinetic energy to or from the thermal or random energy. We note that $-(\mathbf{P}_\alpha \cdot \nabla) \cdot \mathbf{u}_\alpha$ is not single-signed, and therefore it does not quantify irreversible conversion of energy. The net energy can convert in or out of the random component, depending on the sign of the pressure-strain.

The pressure-strain can be decomposed into compressive and incompressive components as

$$-(\mathbf{P}_\alpha \cdot \nabla) \cdot \mathbf{u}_\alpha = -p^{(\alpha)} \theta^{(\alpha)} - \Pi_{ij}^{(\alpha)} D_{ij}^{(\alpha)}, \quad (39)$$

where $-p^{(\alpha)} \theta^{(\alpha)}$ represents the energy conversion due to compressive motion, and

$\theta^{(\alpha)} = \nabla \cdot \mathbf{u}_\alpha$ is the dilatation. Therefore, the remaining term $-\Pi_{ij}^{(\alpha)} D_{ij}^{(\alpha)}$ corresponds

to incompressive energy conversion with the deviatoric pressure tensor $\Pi_{ij}^{(\alpha)} = P_{ij}^{(\alpha)} -$

$p^{(\alpha)} \delta_{ij}$ and the traceless strain rate tensor $D_{ij}^{(\alpha)} = (1/2)(\nabla_i u_j^{(\alpha)} + \nabla_j u_i^{(\alpha)}) - (1/3)\theta^{(\alpha)} \delta_{ij}$ (Yang et al. 2017; Cassak and Barbhuiya 2022 and references therein).

In recent times, two major advances have facilitated the study of the pressure-strain interaction. First, PIC simulations have become sufficiently accurate to evaluate the pressure tensor, and supercomputers have become adequately powerful to perform plasma simulations with higher number of particles and larger systems. Secondly, an evaluation of $-(\mathbf{P}_\alpha \cdot \nabla) \cdot \mathbf{u}_\alpha$ requires accurate evaluation of the full pressure tensor as well as spatial derivatives of the fluid velocity down to kinetic scales. This was not possible observationally before the Magnetospheric Multiscale (MMS) Mission. The MMS mission, consisting of 4 spacecraft separated by a small distance, with high cadence

1668 instruments, provides the first and the only opportunity yet to study pressure-strain
1669 interactions using in-situ data.

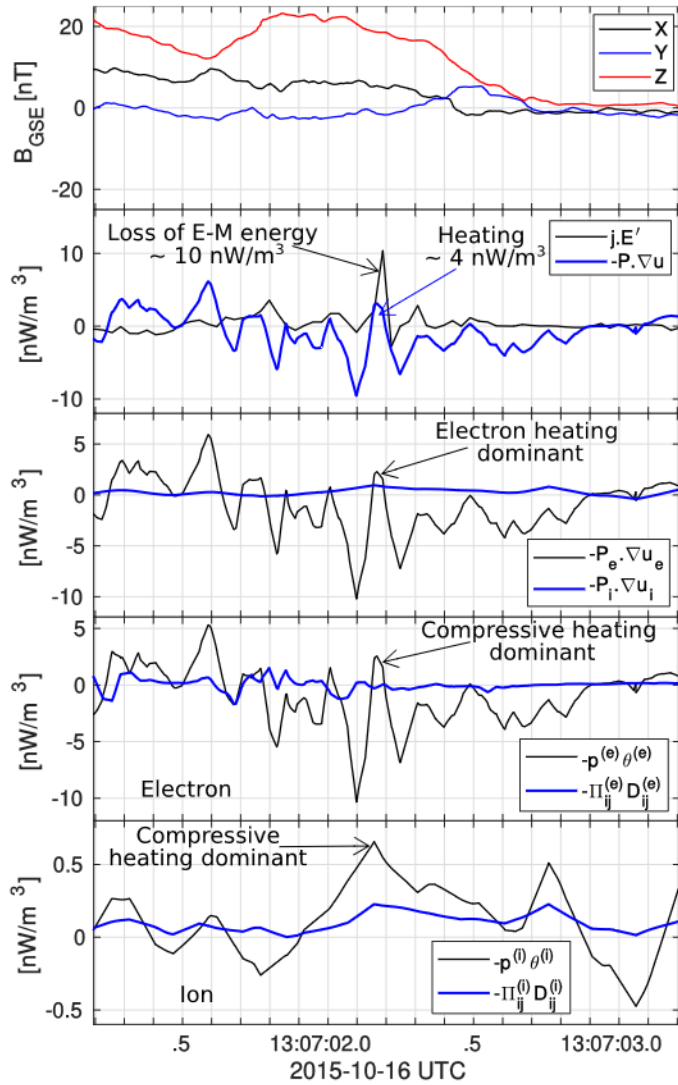
1670 Figure 18 shows an example of MMS observation of the reconnection diffusion region
1671 in the magnetopause current sheet, presented by Burch et al. (2016b). The top panel shows
1672 the magnetic field measurement in GSE coordinates. The next panel plots the
1673 electromagnetic energy conversion rate, as measured by the Zenitani measure (narrow
1674 black), and the energy conversion rate to internal energy, quantified by the total
1675 (ion+electron) pressure-strain rate (broad blue). We use the extension of the multi-
1676 spacecraft curlometer method (Dunlop et al. 1988; Paschmann & Daly 1998), along with
1677 the averaged pressure tensor from all 4 MMS spacecraft to measure $-(\mathbf{P}_\alpha \cdot \nabla) \cdot \mathbf{u}_\alpha$ for
1678 ions and electrons. Both conversion rates show an elevated signal in the diffusion region
1679 with similar magnitude, but the value of $-(\mathbf{P}_\alpha \cdot \nabla) \cdot \mathbf{u}_\alpha$ is smaller than $\mathbf{j} \cdot \mathbf{E}'$. This
1680 observation indicates that only part of the magnetic energy is being converted to random
1681 energy. The third panel shows that the electrons are responsible for the majority of the
1682 conversion. Finally, the bottom two panels show that for both electrons and ions, the
1683 compressive heating rate is stronger than the incompressive part.

1684 These results show that the pressure-strain interaction can be used as an independent
1685 diagnostic of plasma energization in reconnection regions. Bandyopadhyay et al. (2021)
1686 show a few other examples of MMS reconnection events, including magnetosheath
1687 reconnection in thin current sheets and electron-only reconnection to analyze the role of
1688 the pressure-strain. Examples from turbulent PIC simulations are also shown by
1689 Bandyopadhyay et al. (2021) for comparison with MMS data. Broadly speaking, the
1690 simulations and different kinds of reconnection events sampled by MMS do not show any
1691 systematic difference in the pressure-strain interaction in the diffusion region. However,
1692 $-(\mathbf{P}_\alpha \cdot \nabla) \cdot \mathbf{u}_\alpha$ can be negative in some cases at the reconnecting X-lines, indicating that
1693 internal energy is locally being converted into kinetic energy. This contrasts with the
1694 electromagnetic energy conversion rate (as measured by $\mathbf{j} \cdot \mathbf{E}'$), which is positive for most
1695 of the cases. Understanding the ratio of ion to electron conversion between kinetic and
1696 internal energy also poses an intriguing challenge. Like the example shown here, most
1697 reconnection cases show that the electron energy conversion rate (as measured by $-(\mathbf{P}_\alpha \cdot$
1698 $\nabla) \cdot \mathbf{u}_\alpha$) is larger than the ion energy conversion rate. This is in contrast to the global
1699 energy conversion, which is dominated by the ions in the magnetosheath. A recent work
1700 by Barbhuiya and Cassak (2022) provided an explanation of this based on scaling analysis.
1701 Further statistical studies are required to fully understand the role of pressure-strain in
1702 heating due to magnetic reconnection.

1703 Finally, it should be noted that the above works focused mainly on the $-(\mathbf{P}_\alpha \cdot \nabla) \cdot \mathbf{u}_\alpha$

1704 term that relates the transfer of bulk kinetic energy to internal energy. However, as shown
 1705 in Fadanelli et al. (2021), it is possible to look at all the terms that compose the
 1706 electromagnetic, kinetic, and internal energy equations. Such a description allows to
 1707 perform a point-by-point analysis of all energy conversion channels. While the study of
 1708 how these various terms compare with and balance each other in the context of
 1709 reconnection was done using a Hybrid-Vlasov simulation, this exercise remains to be
 1710 done with spacecraft observations.

1711



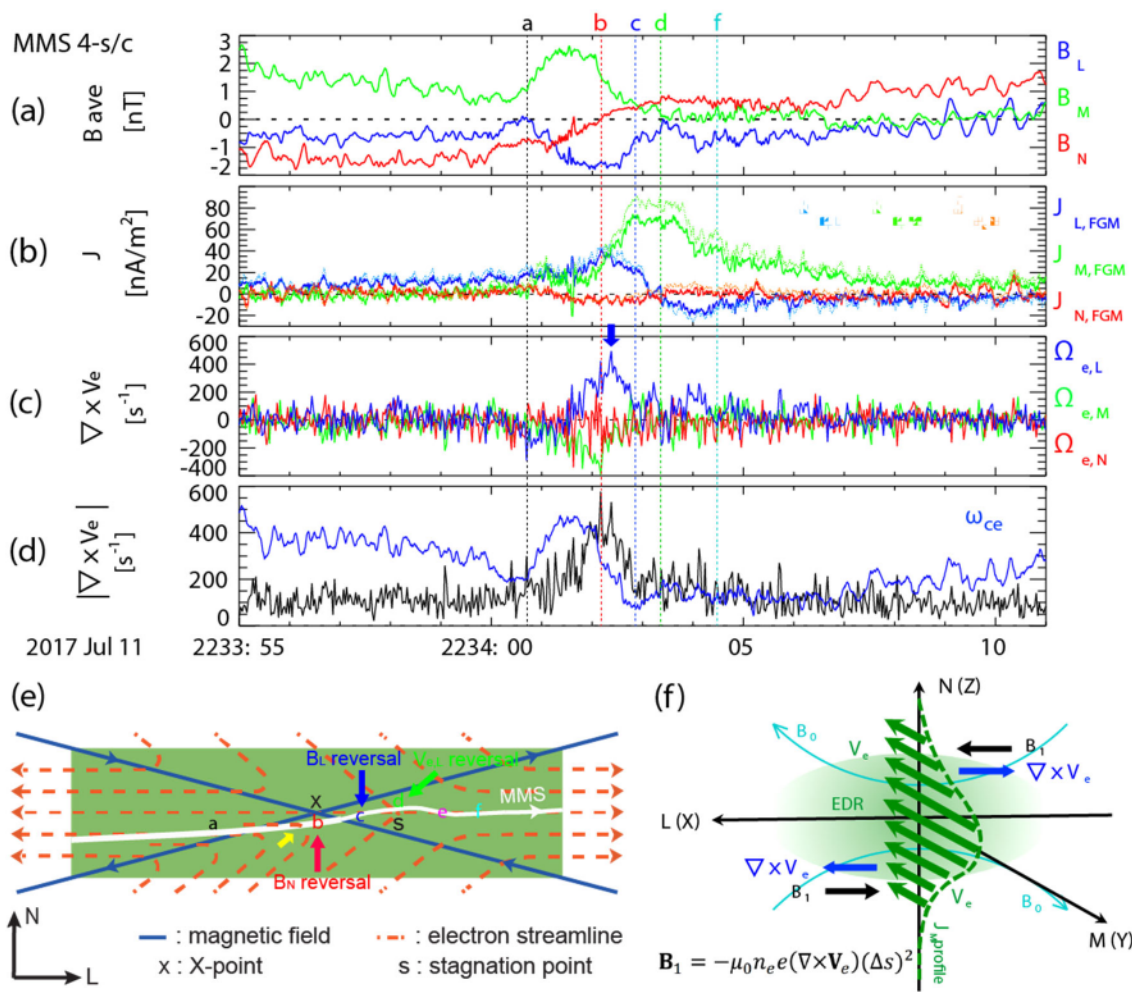
1712 **Fig. 18** MMS data in the magnetopause reconnection event on 16 October 2015. The
 1713 X-line crossing was around 13:07:02.4 UTC. From top the plotted quantities are the
 1714 magnetic field in GSE coordinates (\mathbf{B}_{GSE}), the Zenitani measure ($\mathbf{j} \cdot \mathbf{E}'$) and pressure-
 1715 strain rate $-(\mathbf{P} \cdot \nabla) \cdot \mathbf{u}$, electron $-(\mathbf{P}_e \cdot \nabla) \cdot \mathbf{u}_e$ and ion $-(\mathbf{P}_i \cdot \nabla) \cdot \mathbf{u}_i$ pressure-strain
 1716 rates, compressive $(-\mathbf{p}^{(e)} \theta^{(e)})$ and incompressive $(-\Pi_{ij}^{(e)} D_{ij}^{(e)})$ pressure-strain rates for

1717 electrons, and compressive ($-p^{(i)}\theta^{(i)}$) and incompressive ($-\Pi_{ij}^{(i)}D_{ij}^{(i)}$) pressure-strain
 1718 rates for ions.

1719

1720 4.1.4 Electron Vorticity Indicative of the EDR

1721 The electron vorticity ($\Omega_e = \nabla \times u_e$) can be used as a proxy for delineating the EDR
 1722 of magnetic reconnection. Figures 19a-d show the 11 July 2017 event (Torbert et al. 2018),
 1723 during which MMS traversed a magnetotail current sheet along the trajectory shown in
 1724 Figure 19e: (a) the four-spacecraft tetrahedral-averaged magnetic field components in
 1725 boundary normal coordinates (LMN), (b) the current density calculated from the
 1726 curlometer technique (Dunlop et al. 2002), (c and d) electron vorticity and its magnitude
 1727 (black profile) compared to ω_{ce} (the electron cyclotron angular frequency; blue). The
 1728 electron vorticity is enhanced around ‘b’ marked by the vertical dashed red line in Figures
 1729 19a-d and red arrow in Figure 19e.
 1730



1731

1732 **Fig. 19** MMS observation of a magnetotail current sheet crossing along the trajectory
 1733 shown in white in panel (e). (a) The tetrahedral-averaged magnetic field, (b) current
 1734 density calculated from the curlometer technique, (c,d) electron vorticity and its
 1735 magnitude compared to ω_{ce} . Panel (f) illustrates the origin of the enhanced electron
 1736 vorticity near the northern/southern edge of the EDR. Adapted from Hwang et al. (2019).
 1737

1738 Electron velocity vectors and electron distribution functions measured at the four
 1739 spacecraft (not shown) demonstrate that the enhanced electron vorticity is due to the
 1740 intense shear of the velocity mostly along $-\hat{\mathbf{e}}_M$, which originates from the variation along
 1741 $\pm\hat{\mathbf{e}}_N$ of the meandering electrons' velocity (Figure 19f). Since the meandering electrons
 1742 carry the out-of-plane current (j_M in Figure 19b), the electron vorticity enhancement
 1743 should coincide with the strong gradient of the current density. Indeed, Ω_e peaks (blue
 1744 arrow in Figure 19c) are located at the edges of the current density (j_M) profile (Figure
 1745 19b).

1746 In these observations, the largest component of electron vorticity, i.e., $\Omega_{e,L}$ (Figure
 1747 19c), can be approximately written as
 1748 $\Omega_{e,L} \sim -\partial u_{e,M}/\partial N \sim (1/(en_e)) \partial j_M/\partial N \sim (1/(en_e\mu_0)) \partial^2 B_L/\partial N^2$. If B_L changes from
 1749 0 at the neutral sheet to B_{edge} at the southern/northern edge of an EDR with a thickness of
 1750 d_e , $\Omega_{e,L} \sim (1/(en_e\mu_0)) B_{edge}/d_e^2 \sim \omega_{ce}$. Thus, a peak of $\Omega_{e,L}$ that is comparable to or
 1751 larger than ω_{ce} (Figure 19d) delineates the N -directional edge of the EDR of a
 1752 reconnecting current sheets on the d_e scale. This demonstrates why $|\Omega_e|$ compared with
 1753 ω_{ce} can be a physical measure for EDR identification (Hwang et al. 2019).

1754

1755 4.1.5 Magnetic flux transport (MFT) method

1756 The magnetic flux transport (MFT) method represents a novel way of detecting
 1757 diffusion regions in situ. It is based on the definition of reconnection as the transport of
 1758 magnetic flux across magnetic separatrices that intersect at an X-line (Vasyliunas et al.
 1759 1975). This method measures signatures of active reconnection in the in-plane velocity
 1760 of magnetic flux, \mathbf{U}_ψ , and its divergence, $\nabla \cdot \mathbf{U}_\psi$. Previously derived in 2D (Liu et al.
 1761 2018a; Liu and Hesse 2016) from Faraday's law and the advection equation of magnetic
 1762 flux, $\partial\psi/\partial t + \mathbf{U}_\psi \cdot \nabla_\perp \psi = 0$, \mathbf{U}_ψ was simplified and adapted for application in 3D (Li
 1763 et al. 2021, 2023) as

$$1764 \mathbf{U}_\psi = (E_M/B_{LN})(\hat{\mathbf{e}}_M \times \hat{\mathbf{b}}_{LN}), \quad (40)$$

1765 where E_M is the out-of-plane (M) component of the electric field in LMN coordinates,
 1766 $B_{LN} = \sqrt{B_L^2 + B_N^2}$ is the magnetic field component in the 2D reconnection (LN) plane,
 1767 $\hat{\mathbf{e}}_M$ is the unit vector in the M direction, and $\hat{\mathbf{b}}_{LN} \equiv \mathbf{B}_{LN}/B_{LN}$ the unit vector of the in-

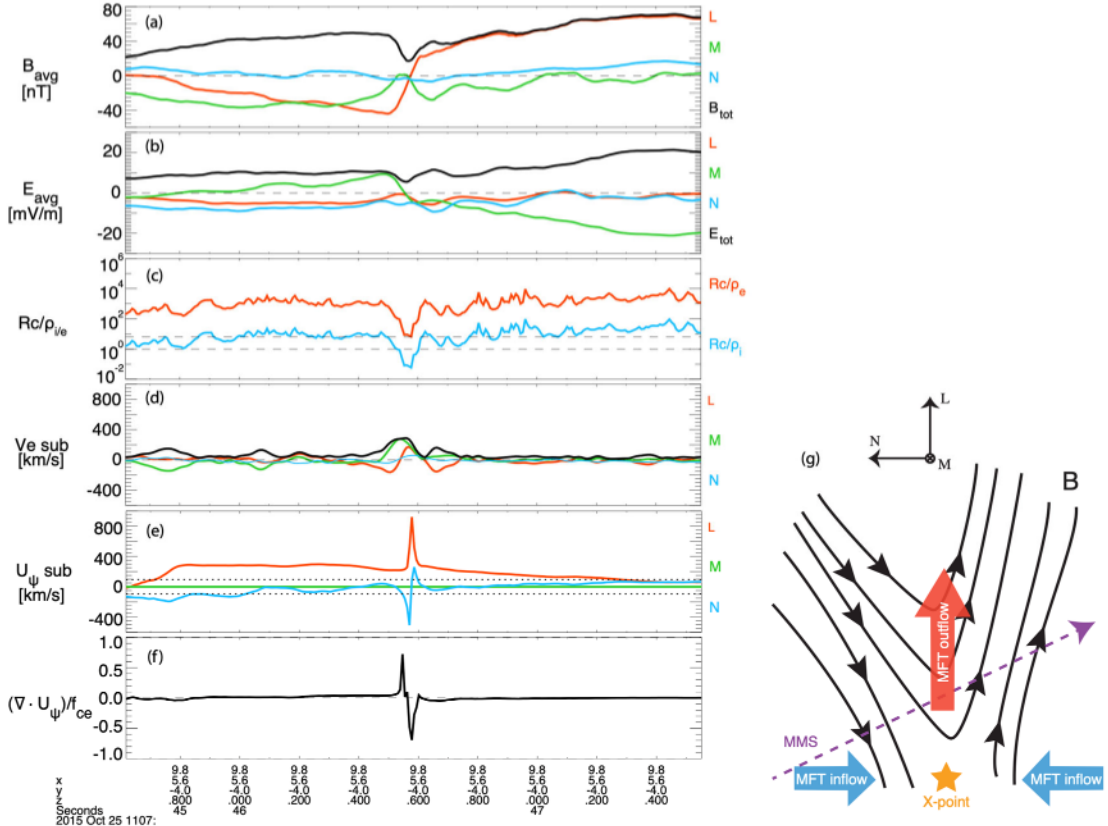
1768 plane magnetic field \mathbf{B}_{LN} . The underlying assumptions are that the advection equation
1769 does not have a source or loss term, i.e., no magnetic field generation or diffusion occurs,
1770 and that $k_M \ll k_\perp$, where k_M and k_\perp are the wavenumbers corresponding to the length
1771 scales of the magnetic field variation parallel and perpendicular to the M direction,
1772 respectively (Li et al. 2023, 2021). The latter essentially means that the scale of variation
1773 in the out-of-plane (M) direction is much larger than the current sheet thickness.
1774 Physically, it represents quasi-2D reconnection (Liu et al. 2018b, 2019; Li et al. 2020).
1775 The LMN coordinates can be determined by methods such as minimum variance analysis
1776 (Sonnerup and Scheible 1998), maximum directional derivative (Shi et al. 2019), or a
1777 combination of methods (Genestreti et al. 2018) (see section 3.2.1 for more details). In
1778 simulations, \mathbf{U}_ψ can be calculated if the guide field (M) direction is known (e.g., Li et al
1779 2023). Based on measured electromagnetic fields, MFT locates reconnection sites in
1780 diffusion regions without using information on plasma flows (Qi et al. 2022). This is ideal
1781 for identifying diffusion regions where ion and/or electron outflow jets are not well
1782 developed.

1783 The MFT method has been demonstrated to accurately identify reconnection in 2D
1784 and 3D kinetic turbulence (Li et al. 2021, 2023) and 3D shock turbulence (Ng et al. 2022)
1785 simulations. Recent MMS observations further demonstrated the capability and accuracy
1786 of MFT statistically, by directly measuring MFT signatures for active reconnection
1787 throughout Earth’s magnetosphere (Qi et al. 2022). Reconnection signatures in MFT are
1788 (i) co-existing Alfvénic inflow and outflow magnetic flux (\mathbf{U}_ψ) jets, and (ii) a
1789 significantly enhanced divergence of flux transport ($\nabla \cdot \mathbf{U}_\psi$) at an X-line exceeding the
1790 threshold of order $0.1\omega_{ce}$. We note that the first signature should be observed in a proper
1791 frame in which the corresponding X-line is seen to be quasi-stationary.

1792 Here we show an example of application of MFT to the Eriksson event (Eriksson et
1793 al. 2018) observed in the magnetosheath on 25 October 2015 by MMS in Figure 20.
1794 Panels (e,f) show the MFT quantities: \mathbf{U}_ψ reveals bi-directional inflow MFT jets in the
1795 N direction (blue) and a super-Alfvénic outflow jet in the L direction (red), as a signature
1796 of reconnection; $\nabla \cdot \mathbf{U}_\psi$ is on the order of the electron gyro-frequency $f_{ce} = \omega_{ce}/(2\pi)$,
1797 exceeding the threshold of $0.1f_{ce}$ for identification. The MFT signatures are clear despite
1798 the fact that no ion jets were detected along the spacecraft trajectory in this event,
1799 interpreted as reconnection in an extended current sheet. A total of 37 previously reported
1800 EDR or reconnection-line crossing events were analyzed, including well-known MMS
1801 events (e.g., Burch et al. 2016b; Torbert et al. 2018) and electron-only events (e.g., Phan
1802 et al. 2018). Almost all ($\geq 95\%$) of the events can be identified through either of the MFT
1803 signatures (Qi et al. 2022). The range of the observed \mathbf{U}_ψ is on the order of ion to electron

1804 Alfvén speeds, and $\nabla \cdot \mathbf{U}_\psi$ is of order $0.1 f_{ce}$ or higher. This order of magnitude is
 1805 consistent with simulations (Li et al. 2021, 2023). The MFT method can thus provide a
 1806 clear identification of reconnection in diffusion regions in space.

1807



1808
 1809 **Fig. 20** MMS observations of the Eriksson et al. event (adapted from Qi et al. (2022)).
 1810 (a) Magnetic field and (b) electric field averaged over four spacecraft. (c) Radius of
 1811 curvature R_c normalized to the electron (red) and ion (blue) gyro-radius. (d) Electron bulk
 1812 flow velocity and (e) MFT velocity \mathbf{U}_ψ , where the ion bulk flow velocity is subtracted.
 1813 Dotted lines denote the upstream Alfvén speed. (f) $\nabla \cdot \mathbf{U}_\psi$ normalized to f_{ce} . (g) Sketch
 1814 of the trajectory of MMS and expected MFT inflows and outflow, adapted from Eriksson
 1815 et al. (2018).

1816

1817 4.1.6 Electron Diffusion Region Detection with Machine Learning methods

1818 Machine learning methods recently became a useful tool for space physics data
 1819 analysis and were employed for a variety of tasks, including classification, event detection,
 1820 and prediction (sections 2.3-2.5). In the following, we present some recent developments
 1821 which apply this approach to the detection of EDRs. This type of event is “rare”: Webster
 1822 et al. (2018) reported 32 events, Lenouvel et al. (2021) identified 18 new events, while

1823 Fuselier et al. (2016) estimated 56 events for the first 2.5 years of the nominal MMS
1824 mission. Therefore, this, at first glance, does not argue for the use of machine learning for
1825 EDR detection. However, by using special features of the MMS measurements, namely
1826 the details of the electron distribution function, it is possible to extract valuable
1827 information which can be processed by machine learning algorithms.

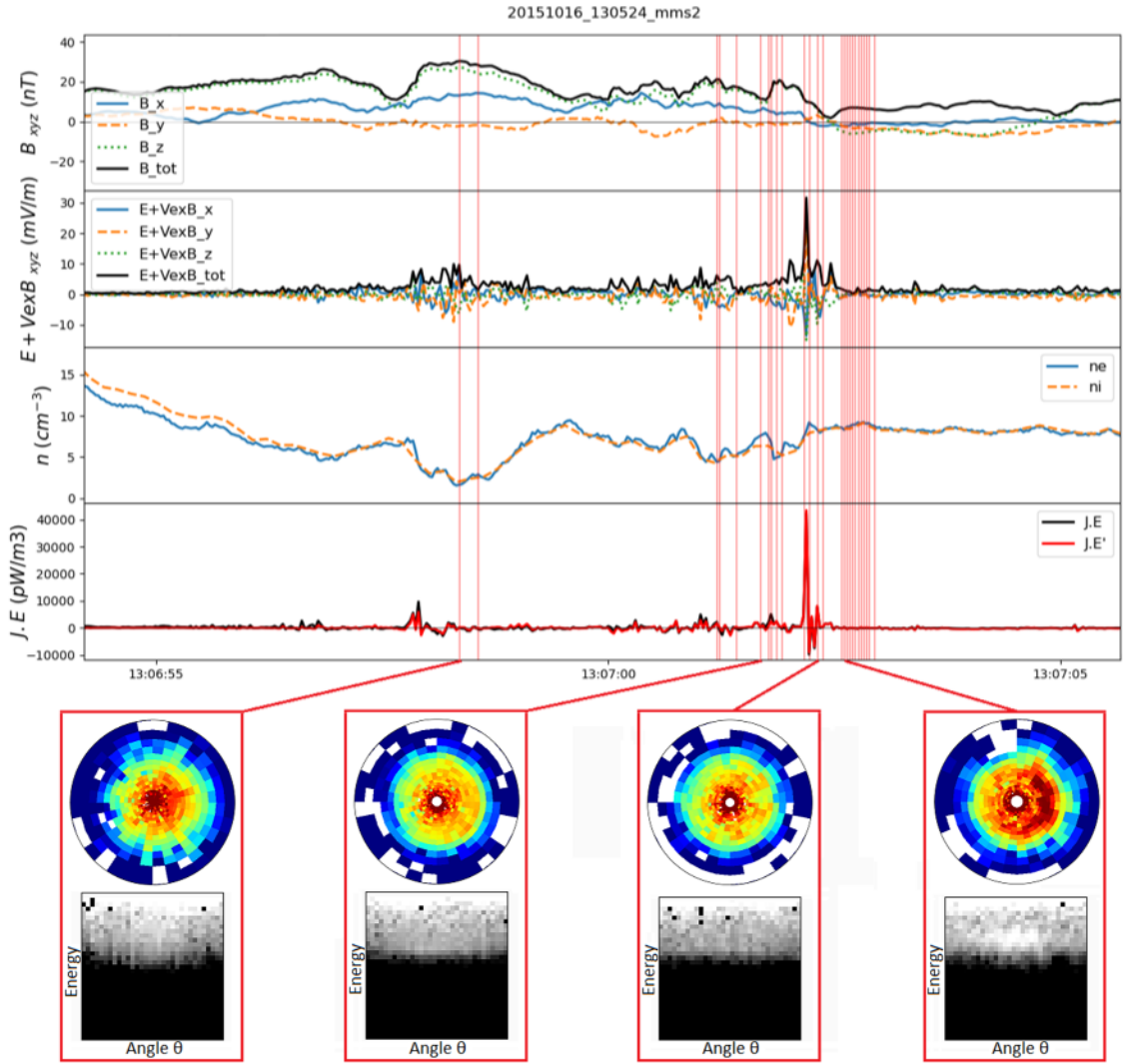
1828 The first algorithm is detailed in Lenouvel et al. (2021) and is only summarized here.
1829 It is a rather classical feed-forward MultiLayer Perceptron (e.g., Rumelhart et al. 1986),
1830 i.e., a neural network with multiple layers of neurons connected to each other, using MMS
1831 observations as features and 4 classes as outputs. Notably one of the key features is a
1832 scalar parameter specifically characterizing the asymmetry observed in the crescent-
1833 shaped electron distribution functions (hereafter referred to as "electron crescents"
1834 or "crescents" for notational simplicity) on the dayside magnetopause (Hesse et al. 2014;
1835 Bessho et al. 2016; see also section 4.3.1). The main drawback of this early model was
1836 the large number of false positives which needed to be visually analyzed to extract the
1837 best EDR candidates. It nevertheless enabled an increase in the number of EDR events
1838 and eventually led to a statistical analysis of the sign of the energy conversion rate $\mathbf{j} \cdot \mathbf{E}'$,
1839 and a discussion on the distinction between inner and outer EDRs (Lenouvel et al. 2021).

1840 The second algorithm (Lenouvel 2022) has a different structure and is based on a
1841 Convolutional Neural Network (CNN) (Lecun et al. 1998), i.e., a deep learning algorithm
1842 specifically adapted to image recognition and classification. The idea of the architecture
1843 builds on the characteristic feature of electron crescents seen in the full distribution
1844 functions rather than reducing them to a scalar as in the first algorithm. The training set
1845 is based on all 50 events described in Webster et al. (2018) and a total of 214 crescents
1846 yielded by Lenouvel et al. (2021) using data from the four MMS spacecraft. The
1847 distribution functions are transformed into 32 by 32 pixel images where each pixel holds
1848 the value of the electron PSD for a given angle ($\theta = \arctan(v_{\perp 2}/v_{\perp 1})$) and energy ranges
1849 (see Figure 21 for details). The range of PSD on log scale (min-max for all images) is
1850 coded on 256 levels. Data augmentation is then used to increase the number of training
1851 samples, by first extracting 112 most clear crescents (exhibiting a clear left-right
1852 asymmetry in the $v_{\perp 1} - v_{\perp 2}$ plane) and then combining them with each other (by
1853 averaging two images after random small rotation and adding logarithmic noise), which
1854 produces a dataset of ${}_{112}C_2 = 112!/(110!2!) = 6126$ new synthetic crescents from
1855 all possible combinations. The CNN architecture is formed by a succession of dedicated
1856 layers which aim at extracting features or patterns in input data. Finally, applying this
1857 algorithm on the full MMS phase 1b of the prime mission resulted in the discovery of 17
1858 new events (from the analysis of MMS 1 and 2 data only). For future studies, a list of

1859 events combining those obtained from both algorithms, with the addition of individual
1860 events analyzed in the literature during phases 1a and 1b, is available at Zenodo
1861 (<https://zenodo.org/record/8319481>).

1862 To demonstrate how the detection works and performs, a model was trained after
1863 removing the distribution functions (736 distribution functions including real crescents,
1864 synthetic crescents and random distribution functions) from the EDR event reported by
1865 Burch et al. (2016b) that took place on 16 October 2015 at 13:07:02 UTC. The model
1866 could then be applied to the whole event (from 13:05:25 UTC to 13:07:44 UTC) without
1867 any bias that could be due to data leakage between the training dataset and the data from
1868 this example. In Figure 21, the red vertical lines correspond to times of the distribution
1869 functions labeled as “crescents” by the model; 26 are visible on the plot and, after visual
1870 inspection, 18 of them were considered as correctly identified by the algorithm (true
1871 positives).

1872



1873

1874 **Fig. 21** EDR event from Burch et al. (2016b) with detected crescent distribution
 1875 functions. The top four panels show MMS2 observations of the magnetic field \mathbf{B} ,
 1876 electron-frame electric field \mathbf{E}' (showing the departure from the ideal conditions),
 1877 electron and ion densities, and the energy conversion rate $\mathbf{j} \cdot \mathbf{E}'$. Four of the identified
 1878 “crescents” are shown below the time series plots, both in classical phase space density
 1879 units (top) and in transformed 32×32 images (bottom). The two-dimensional electron
 1880 distribution slices are displayed in the $v_{\perp 1} - v_{\perp 2}$ plane where $v_{\perp 1}$ is directed along $(-\mathbf{u}_e \times$
 1881 $\mathbf{B}) \times \mathbf{B}$ (approximately the $\mathbf{E} \times \mathbf{B}$ direction, where \mathbf{E} is the electric field, and \mathbf{u}_e is the
 1882 electron bulk velocity), and $v_{\perp 2}$ is directed along $-\mathbf{u}_e \times \mathbf{B}$ (approximately the direction
 1883 of \mathbf{E}).
 1884

1885 In this application, only the distribution function is used to make a prediction and no
 1886 post-processing is applied, so false positives are to be expected. Removing these false

positives would require the use of additional parameters to be associated with the distribution functions, such as the electron density (low densities are known to produce incomplete distribution functions that are interpreted as asymmetric by the model) or other key EDR parameters including the electron-frame electric field \mathbf{E}' and $\mathbf{j} \cdot \mathbf{E}'$. One needs to bear in mind that peaks in the last two parameters may not occur at the same time as the presence of electron crescents (the separation time can go up to a few hundred milliseconds), so the automatic removal of false detections is not an easy matter and will be the topic of future work with a more advanced automatic EDR detection model. Nonetheless, the ability of these automatic EDR detection methods shows that they are valuable to identify and analyze rare and complex physical plasma processes.

1897

1898 **4.1.7 Magnetic Nulls**

1899 Magnetic nulls are singularities or critical points where the magnetic field vanishes,
1900 and can be essential for characterizing 3D magnetic topology and understanding magnetic
1901 reconnection in 3D (Pontin and Priest 2022 and references therein). See recent works (e.g.,
1902 Fu et al. 2015; Olshevsky et al. 2020; Guo et al. 2022; Ekawati and Cai 2023) for details
1903 about the methods to identify and analyze the magnetic nulls.

1904

1905 **4.2 Analysis Methods for the Electron Diffusion Region**

1906 **4.2.1 Estimation of Anomalous Resistivity, Viscosity, and Diffusion**

1907 In Graham et al. (2022) anomalous terms associated with lower hybrid waves were
1908 estimated from direct spacecraft observations in magnetopause reconnection events, and
1909 an assessment was performed to see whether the anomalous terms could contribute to the
1910 reconnection electric field E_M . The anomalous terms are based on expansions of the
1911 electron continuity and momentum equations:

$$1912 \quad \frac{\partial n}{\partial t} + \nabla \cdot (n\mathbf{u}) = 0, \quad (41)$$

$$1913 \quad m \frac{\partial(n\mathbf{u})}{\partial t} + m\nabla \cdot (n\mathbf{u}\mathbf{u}) + \nabla \cdot \mathbf{P} + en(\mathbf{E} + \mathbf{u} \times \mathbf{B}) = 0, \quad (42)$$

1914 where m is the electron mass, e is the unit charge, n is the number density, \mathbf{u} is the
1915 bulk velocity, \mathbf{P} is the pressure tensor, \mathbf{E} is the electric field, and \mathbf{B} is the magnetic field.
1916 To derive the anomalous terms the quantities in these equations are separated into
1917 fluctuating and quasi-stationary components: $Q = \delta Q + \langle Q \rangle$, where δQ is the fluctuating
1918 component due to waves, and $\langle Q \rangle$ is an ensemble average over Q , and $\langle \delta Q \rangle = 0$. The
1919 anomalous terms are obtained by taking the ensemble average of the momentum equation.
1920 The ensemble average of the product of two quantities is $\langle QR \rangle = \langle Q \rangle \langle R \rangle + \langle \delta Q \delta R \rangle$. From

1921 the continuity equation (41) a cross-field diffusion coefficient can be defined as

1922
$$D_{\perp} = -\frac{\langle \delta n \delta u_N \rangle}{\nabla \langle n \rangle_N}, \quad (43)$$

1923 where \mathbf{N} is the direction normal to the local boundary. From the momentum equation (42)
1924 we obtain:

1925
$$\langle \mathbf{E} \rangle + \langle \mathbf{u} \rangle \times \langle \mathbf{B} \rangle = -\frac{\nabla \cdot \langle \mathbf{P} \rangle}{\langle n \rangle e} - \frac{m}{\langle n \rangle e} \nabla \cdot (\langle n \rangle \langle \mathbf{u} \rangle \langle \mathbf{u} \rangle) + \mathbf{D} + \mathbf{T} + \mathbf{I}. \quad (44)$$

1927 The time derivative term in Eq. (42) is assumed to be small, so it is neglected in Eq. (44).
1928 Here \mathbf{D} , \mathbf{T} , and \mathbf{I} are the anomalous resistivity, anomalous viscosity, and anomalous
1929 inertial terms, which are given by

1930
$$\mathbf{D} = -\frac{\langle \delta n \delta \mathbf{E} \rangle}{\langle n \rangle}, \quad (45)$$

1931
$$\mathbf{T} = -\frac{\langle n \mathbf{u} \times \mathbf{B} \rangle}{\langle n \rangle} + \langle \mathbf{u} \rangle \times \langle \mathbf{B} \rangle, \quad (46)$$

1932
$$\mathbf{I} = -\frac{m}{e \langle n \rangle} [\nabla \cdot (\langle n \mathbf{u} \mathbf{u} \rangle) - \nabla \cdot (\langle n \rangle \langle \mathbf{u} \rangle \langle \mathbf{u} \rangle)]. \quad (47)$$

1933 This approach to calculate the anomalous terms corresponds to Reynolds averaging,
1934 which is often used to study fluid turbulence. The above terms were derived in Graham
1935 et al. (2022). Similar definitions are used in numerical simulations (Che et al. 2011 ; Price
1936 et al. 2016; Le et al. 2018; Price et al. 2020), although often the particle fluxes are treated
1937 as a single quantity, which can modify the contributions from the anomalous terms (Price
1938 et al. 2020).

1939 The anomalous terms result from the correlations between fluctuating quantities
1940 associated with the waves. In numerical simulations the average is taken over the
1941 reconnection out-of-plane (M) direction (e.g., Price et al. 2016, 2020; Le et al. 2017),
1942 although the ensemble average can be performed over time (Le et al. 2018). With MMS
1943 an approximate average can also be obtained by averaging over the four spacecraft.

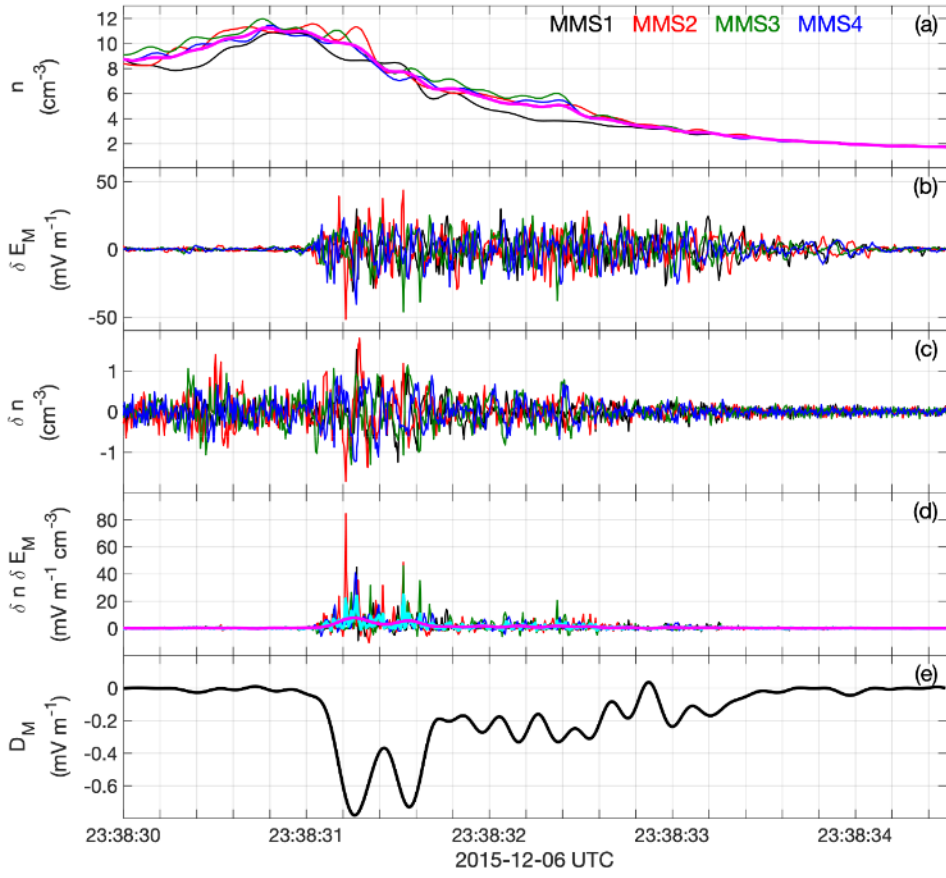
1944 To calculate the anomalous contributions requires fields and particle measurements
1945 that can resolve the lower hybrid wave fluctuations. This is possible for the electron
1946 particle data using the highest time resolution electron distributions and moments, which
1947 can be sampled every 7.5 ms, rather than the nominal 30 ms sampling rate during burst
1948 mode (Pollock et al. 2016). Resolution of 7.5 ms is achieved by reducing the azimuthal
1949 resolution in the spacecraft spin plane of the electron measurements (Rager et al. 2018;
1950 Appendix A). Since we are interested in the bulk changes in the distributions rather than

1951 fine structures in computing the lower order moments, this reduced azimuthal resolution
1952 does not present a major problem.

1953 The anomalous terms were calculated in Graham et al. (2022) and Figure 22 shows
1954 the steps to calculate the M component of \mathbf{D} . We summarize the steps they used to
1955 calculate the anomalous terms:

- 1956 (1) The vector quantities are converted to the LMN coordinate system.
- 1957 (2) All electric and magnetic field data are resampled to the sampling frequency of the
1958 7.5 ms electron moments.
- 1959 (3) Four spacecraft timing analysis on B_L at the current sheet to determine the velocity of
1960 the boundary in the normal direction and the time delays between the spacecraft.
- 1961 (4) The time delays are used to offset the spacecraft times so all spacecraft cross the
1962 current sheet at the same time as MMS1.
- 1963 (5) Quasi-stationary quantities $\langle Q \rangle$ are obtained by bandpass filtering the signals below 5
1964 Hz, and averaging the data over the four spacecraft. For the magnetopause, as shown in
1965 Figure 22, the frequency of the lower hybrid waves is typically comparable to or above
1966 10 Hz, so this removes most of the fluctuations due to these waves.
- 1967 (6) The fluctuating quantities δQ associated with lower hybrid waves are obtained by
1968 band pass filtering the data above 5 Hz (Figures 22b,c).
- 1969 (7) The correlations between fluctuating quantities $\langle \delta Q \delta R \rangle$ are obtained by averaging
1970 $\delta Q \delta R$ over the four spacecraft; then low-pass filtering the product below 5 Hz. This
1971 removes most of the remaining higher-frequency components from these terms (Figure
1972 22d). See Graham et al. (2022) for further details on the calculation of the anomalous
1973 terms (see also Table 6 in Appendix B).

1974



1975

1976 **Fig. 22** Example of the calculation of the M component of the anomalous resistivity \mathbf{D} .
 1977 (a) Background (lowpass filtered) components of the electron number density n (MMS1-
 1978 MMS4 data are plotted in black, red, green, and blue, respectively) and $\langle n \rangle$ calculated by
 1979 averaging over the four spacecraft (magenta line). (b) and (c) δE_M and δn for the four
 1980 spacecraft. (d) $\delta n \delta E_M$ calculated for the four spacecraft, and the four-spacecraft averaged
 1981 $\delta n \delta E_M$ (cyan), and $\langle \delta n \delta E_M \rangle$ (magenta) obtained by low-pass filtering the averaged $\delta n \delta E_M$.
 1982 I M component of \mathbf{D} calculated from $\langle \delta n \delta E_M \rangle$ and $\langle n \rangle$. In all panels (a)-(d) the quantities
 1983 from MMS2-MMS4 have been time shifted so they cross the current sheet at the same
 1984 time.

1985

1986 4.2.2 Evaluation of Terms in the Electron Vlasov Equation

1987 A wide variety of collisionless plasma phenomena have been studied and understood by
 1988 utilizing the kinetic description provided by the Vlasov equation (e.g., Nicholson 1983;
 1989 Califano et al. 2016; Gershman et al. 2017). Here, we summarize a methodology for utilizing the
 1990 MMS FPI Dual Electron Spectrometer (DES) data (Pollock et al. 2016) in order to compute
 1991 each derivative of the electron PSD f_e that appears in the electron Vlasov equation, given by

1992 $\frac{df_e}{dt} = \frac{\partial f_e}{\partial t} + \mathbf{v} \cdot \nabla f_e - \frac{e}{m_e} (\mathbf{E} + \mathbf{v} \times \mathbf{B}) \cdot \nabla_{\mathbf{v}} f_e = 0. \quad (48)$

1993 For example, since the generalized Ohm's law (electron momentum equation (42)) is derived
 1994 from the moments of the Vlasov equation (48), the method, as explained below, allows us to
 1995 discuss how and which part of the velocity-space distribution of each term of Eq. (48)
 1996 contributes to each term of Eq. (42).

1997 Figure 23 demonstrates the computation techniques needed for each Vlasov equation term
 1998 in the context of an electron spatial-scale current sheet encountered by MMS on 23 December
 1999 2016 (Shuster et al. 2019, 2021a,b). This event is discussed in more detail in Chapter 1.3 of this
 2000 issue (Norgren et al. 2023). The Vlasov equation $df_e/dt = 0$ is a statement indicating that
 2001 PSD is conserved along a particle's Lagrangian trajectory through phase space. In the Eulerian
 2002 frame of the MMS spacecraft, it is necessary to consider and evaluate each term of the Vlasov
 2003 equation (48) (see Shuster et al. (2019, 2023) for a more thorough discussion concerning the
 2004 computation methods outlined here). Figures 23a-d, Figures 23e-h, and Figures 23i-m
 2005 present a high-level, visual comparison of the three distinct methods for evaluating the
 2006 terms $\partial f_e/\partial t$, $\mathbf{v} \cdot \nabla f_e$, and $-(e/m_e)(\mathbf{E} + \mathbf{v} \times \mathbf{B}) \cdot \nabla_{\mathbf{v}} f_e$, respectively.

2007 For the event shown in Figure 23, the current layer's thickness was about 3 to 5 d_e ,
 2008 where the local electron skin depth d_e was about 1.5 km. The normal velocity of the
 2009 structure, V_N , was roughly 50 km/s, where N indicates the direction normal to the current
 2010 layer. The current layer passed by each MMS spacecraft in about a tenth of a second.
 2011 Thus, the spatial thickness was roughly $(50 \text{ km/s}) \cdot (0.1 \text{ s}) = 5 \text{ km}$, comparable to the inter-
 2012 spacecraft spacing of the four MMS spacecraft.

2013 Shuster et al. (2023) explain how to use higher order finite difference approximations
 2014 to obtain more accurate measures of the temporal and velocity-space derivative terms.
 2015 Furthermore, Shuster et al. (2023) show how $\partial f_e/\partial t$ may provide a useful estimate for
 2016 ∇f_e in situations where the plasma is believed to be quasi-steady state:

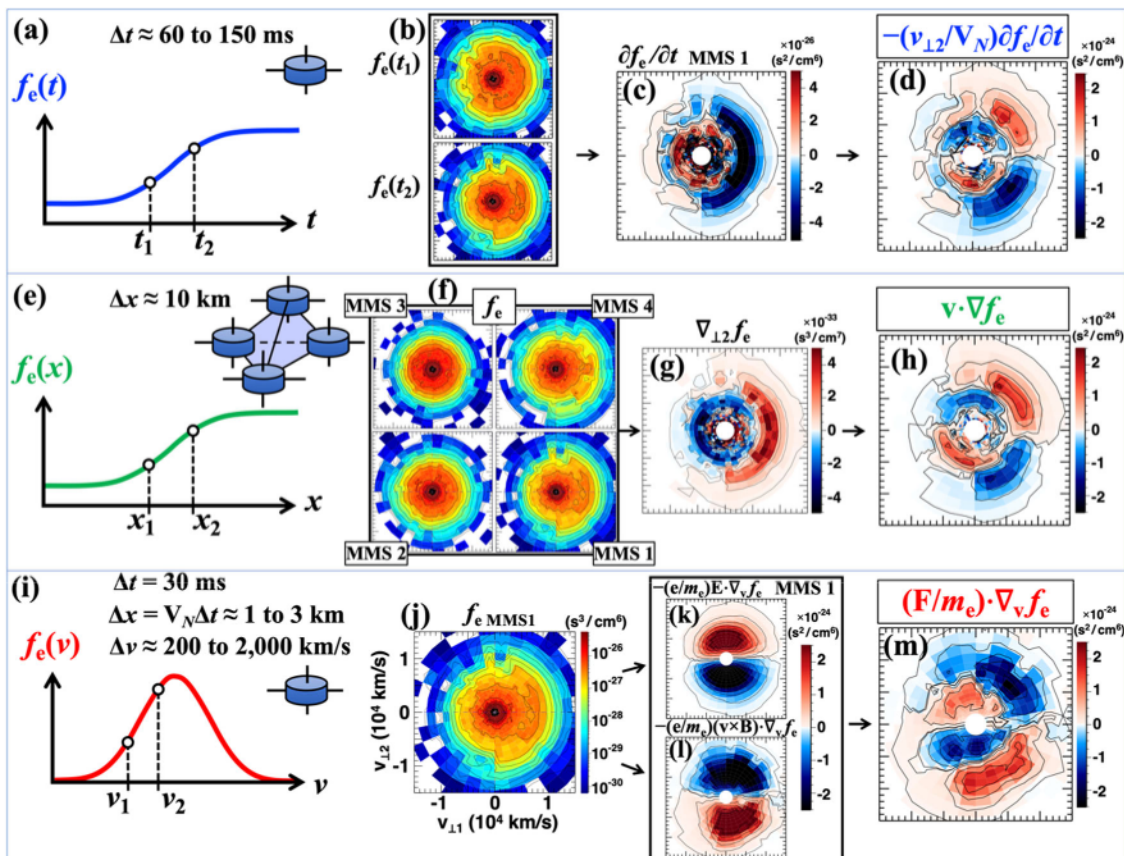
2017 $\frac{Df_e}{Dt} \equiv \frac{\partial f_e}{\partial t} + \mathbf{V}_{\text{str}} \cdot \nabla f_e \approx 0 \rightarrow \frac{\partial f_e}{\partial N} \approx \left(-\frac{1}{V_N} \right) \frac{\partial f_e}{\partial t}, \quad (49)$

2018 where $\partial f_e/\partial t$ is computed in the frame of the spacecraft. The temporal derivative notation
 2019 Df_e/Dt is used to indicate a time derivative taken in a frame moving in position space with
 2020 the velocity of the structure, $\mathbf{V}_{\text{str}} = V_N \hat{\mathbf{e}}_N$. Here the structure is assumed to be planar,
 2021 with spatial variations only in the N direction (Figure 23). As noted by Shuster et al.
 2022 (2019), we point out the connection between the spatial gradient term ∇f_e and the bulk
 2023 electron pressure divergence term $\nabla \cdot \mathbf{P}_e$ via the integral identity utilized when deriving
 2024 the electron momentum equation from the electron Vlasov equation (48):

2025 $m_e \int \mathbf{v}(\mathbf{v} \cdot \nabla f_e) d^3 v = \nabla \cdot \mathbf{P}_e + \nabla \cdot (m_e n_e \mathbf{u}_e \mathbf{u}_e). \quad (50)$

2026 For certain environments, such as magnetopause reconnection sites, the inertial term on
 2027 the right-hand side of Eq. (50) is commonly negligible compared to $\nabla \cdot \mathbf{P}_e$. Thus, we can
 2028 understand how velocity-space structures of each term of the Vlasov equation (48), as
 2029 shown in Figure 23, contribute to collisionless plasma processes including the generation
 2030 of a nonideal electric field (here, through the interrelationship among $\mathbf{v} \cdot \nabla f_e$, $\nabla \cdot \mathbf{P}_e$, and
 2031 the electric field, based on Eq. (50) and the generalized Ohm's law) and field-to-electron
 2032 energy conversion, which are key features of the EDR.

2033 Regarding the velocity-space gradient term on the righthand side of Eq. (48), one may
 2034 perform the derivative computations in the $\{E, \theta, \phi\}$ coordinates native to the FPI detectors,
 2035 or one may choose to first interpolate the distribution to a Cartesian grid with $\{v_x, v_y, v_z\}$
 2036 coordinates before calculating the derivatives (see Shuster et al. (2023) for more details).
 2037 As a consistency check, the results of each approach ought to be qualitatively consistent. We
 2038 note also that the electric and magnetic fields may be averaged to the DES 30 ms cadence
 2039 to obtain a measurement of the full velocity-space gradient term that appears in the Vlasov
 2040 equation.
 2041



2042 **Fig. 23** This figure presents a visual summary of the velocity-space structure and qualitative
 2043 balance of the three Vlasov equation terms for an electron-scale current sheet. The computation

2044 technique for **(a-d)** $\partial f_e / \partial t$, **(e-h)** $\mathbf{v} \cdot \nabla f_e$, and **(i-m)** $(\mathbf{F}/m_e) \cdot \nabla_v f_e$ is shown schematically. Each
 2045 velocity-space panel represents a slice taken in the $v_{\perp 1}$ - $v_{\perp 2}$ plane. In this example, $\hat{\mathbf{e}}_N$
 2046 points roughly along $\hat{\mathbf{e}}_{\perp 2}$, so that the quantities shown in panels (d) and (h) are roughly
 2047 equivalent. Comparing panels (h) and (m), one can see a notable quadrupolar pattern but
 2048 with a polarity difference, suggesting that Eq. (48) is roughly satisfied in velocity space
 2049 under the assumption of negligible $\partial f_e / \partial t$ (panel (c)). Adapted from Shuster et al. (2023).
 2050

2051 4.2.3 Non-Maxwellianity

2052 In many plasmas, particle distributions can deviate significantly from thermal
 2053 equilibrium, namely a Maxwellian distribution. Non-Maxwellian distributions develop
 2054 during magnetic reconnection and can be unstable to a range of instabilities. Several
 2055 scalar parameters have been defined to quantify the deviation of the observed
 2056 distributions from a Maxwellian or bi-Maxwellian distribution function (Greco et al.
 2057 2012; Servidio et al. 2017; Liang et al. 2020; Graham et al. 2021; Argall et al. 2022; see
 2058 also section 4.2.4 for other versions of non-Maxwellianity not mentioned in this section).
 2059 Here we outline the one developed in Graham et al. (2021). In Greco et al. (2012),
 2060 Servidio et al. (2017), and Graham et al. (2021) the definitions of non-Maxwellianity are
 2061 based on the magnitude of the differences between the observed distribution and a model
 2062 Maxwellian distribution. In Liang et al. (2020) and Argall et al. (2022) the definition of
 2063 non-Maxwellianity is based on the increase in kinetic entropy from a Maxwellian
 2064 distribution. In Graham et al. (2021) the non-Maxwellianity parameter was defined as

$$2065 \quad \epsilon = \frac{1}{2n} \int_{v,\theta,\phi} |f(v, \theta, \phi) - f_{model}(v, \theta, \phi)| v^2 \sin\theta dv d\theta d\phi, \quad (51)$$

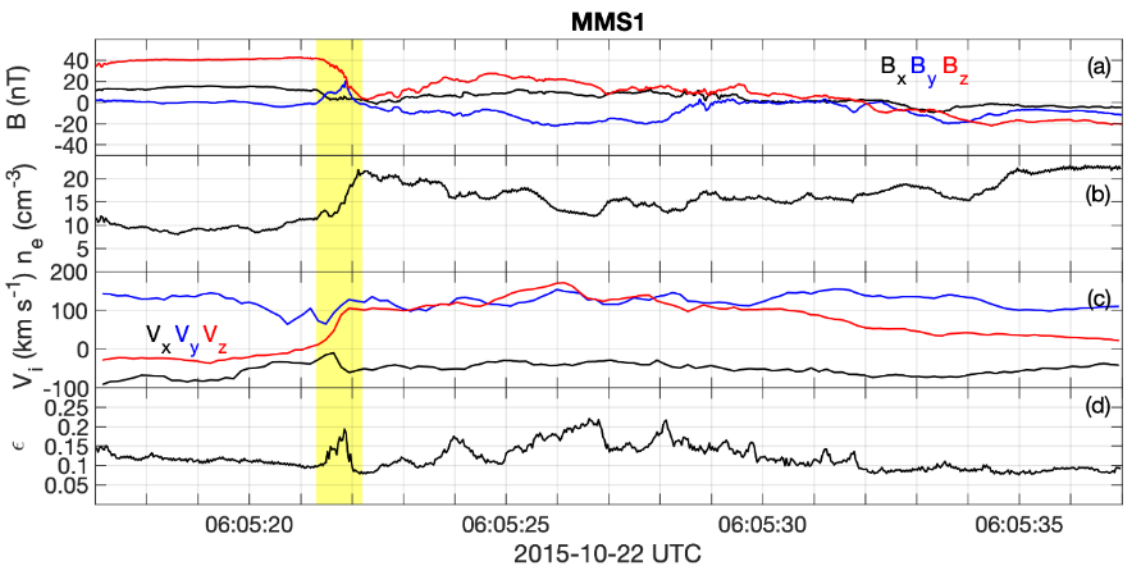
2066 where n is the number density, f is the observed particle distribution function, f_{model} is the
 2067 model particle distribution function, v is the speed, θ is the polar angle, and ϕ is the
 2068 azimuthal angle in velocity space. The model distribution can be either a Maxwellian or
 2069 bi-Maxwellian distribution with the same density, bulk velocity, and temperature as the
 2070 observed distribution. The integral is performed in the same way as the particle moments
 2071 calculations. The $1/(2n)$ factor normalizes ϵ to a dimensionless quantity with values
 2072 between 0 and 1. A value of 0 indicates no deviation from the model distribution, while
 2073 1 corresponds to complete deviation from the model distribution. In Graham et al. (2021)
 2074 a bi-Maxwellian distribution was used as the model distribution, given by:

$$2075 \quad f_{model}(\mathbf{v}) = \frac{n}{\pi^{3/2} v_{th,\parallel}^3 T_{\perp}} \exp \left(-\frac{(v_{\parallel} - V_{\parallel})^2}{v_{th,\parallel}^2} - \frac{(v_{\perp,1} - u_{\perp})^2 + v_{\perp,2}^2}{v_{th,\parallel}^2 (T_{\perp}/T_{\parallel})} \right), \quad (52)$$

2076 where T_{\parallel} and T_{\perp} are the parallel and perpendicular temperatures, $v_{th,\parallel} = \sqrt{2k_B T_{\parallel}/m}$ is
 2077 the thermal speed, k_B is Boltzman's constant, m is the particle mass, and u_{\perp} is the

2078 magnitude of the perpendicular bulk velocity. The velocity coordinates are defined such
 2079 that v_{\parallel} is aligned with the magnetic field, $v_{\perp,1}$ is aligned with the component of the bulk
 2080 velocity perpendicular to the magnetic field, and $v_{\perp,2}$ is orthogonal to v_{\parallel} and $v_{\perp,1}$. The
 2081 calculation of ϵ corresponds to a zeroth order moment calculation, so the largest
 2082 contributions to ϵ typically occur in the thermal energy range. The parameters used to
 2083 calculate f_{model} are obtained from the observed particle moments, so no fitting to the
 2084 observed distribution is required. In Graham et al., the bi-Maxwellian distribution
 2085 function was used rather than an isotropic Maxwellian so temperature anisotropies, which
 2086 are simple to identify in the particle moments, are not the cause of non-Maxwellianity.

2087 Figure 24 shows an example of ϵ calculated for an EDR observed on 22 October 2015.
 2088 The figure shows a reconnection event, as indicated by the reversal in the direction of the
 2089 magnetic field (panel a), an increase in density (panel b), and a northward ion outflow
 2090 (panel c).
 2091



2092
 2093 **Fig. 24** Example of electron non-Maxwellianity for the electron diffusion region
 2094 crossing observed by MMS1 on 22 October 2015. **(a)** Magnetic field. **(b)** electron number
 2095 density. **(c)** Ion bulk velocity. **(d)** Non-Maxwellianity ϵ of electrons. The EDR is indicated
 2096 by the yellow-shaded region.
 2097

2098 The EDR was observed at the time indicated by the yellow-shaded region (e.g., Phan
 2099 et al. 2016; Toledo-Redondo et al. 2016). Figure 24d shows ϵ calculated from the above
 2100 equations. There is a significant increase in ϵ , which peaks in the EDR, indicating that
 2101 non-Maxwellian electron distributions develop there. Additionally, large ϵ occurs in the
 2102 outflow region, indicating that non-Maxwellian electron distributions are not limited to

the EDR. More generally, all the observed EDRs in the first phase of the MMS mission exhibited enhanced electron non-Maxwellianities (Graham et al. 2021). In Graham et al. (2021) a statistical analysis of electron distributions was performed on six months of data to determine which values of ϵ corresponded to enhanced non-Maxwellian electron distributions compared to typical values.

It should be noted that ϵ can be artificially large due to the low counting statistics from the particle detectors when the density is low, such as in Earth's magnetotail. This problem can be mitigated by averaging multiple particle distributions in such cases.

4.2.4 Kinetic Entropy

Due to the fact that collisions in space plasmas are weak, processes that involve kinetic physics often distort the distribution function so that it is no longer in equilibrium. Structures in the distribution function are linked to specific energy conversion processes (Egedal et al. 2010a, 2010b; Hoshino et al. 2001) and are used to create maps of the reconnection diffusion region (Chen et al. 2008, 2016) and study the spatio-temporal evolution of reconnection (Shuster et al. 2014, 2015; Egedal et al. 2016; Barbhuiya et al. 2022). Inhomogeneities in the distribution were quantified to provide indicators of when kinetic physics is important (Scudder and Daughton 2008; Aunai et al. 2013; Swisdak 2016; Section 4.1.2). The measured distribution was compared to an equivalent distribution in equilibrium to quantify the amount of free energy available to be dissipated (Greco et al. 2012; Servidio et al. 2017; Graham et al. 2021; Lindberg et al. 2022; section 4.2.3). Similar considerations were made with respect to kinetic entropy (Boltzmann 1877), noting that the measured distribution will be non-Maxwellian if its entropy is less than that of an equilibrium Maxwellian distribution with the same density and effective temperature (Kaufmann and Paterson 2009; Liang et al. 2019, 2020). The theoretical development of non-Maxwellianity (Liang et al. 2020) was adapted to the non-uniform velocity space grid of MMS plasma measurements, and then was applied to a magnetotail reconnection event to show that non-Maxwellianity is indeed linked to kinetic processes in the EDR (Argall et al. 2022).

To develop a theory of kinetic entropy for a distribution function in velocity space, we start with Boltzmann's equation $S = k_B \ln \Omega$, where k_B is Boltzmann's constant and $\Omega = N_{tot}! / \prod_{j,k} N_{jk}!$ is the total number of microstates that correspond to a given macrostate, N_{tot} is the total number of particles in the system and is assumed constant, N_{jk} is the number of particles in the j th position-space and k th velocity-space cell of phase space, and the product over j and k is over all position- and velocity-space cells, respectively. We then break phase space up into discrete bins and separate the total

2139 entropy into position and velocity space entropy (Mouhot and Villani 2011) to obtain a
 2140 value for entropy that is local in position space and hence is measurable by a single
 2141 spacecraft (Liang et al. 2019),

$$2142 \quad S = S_r + S_v, \quad (53)$$

2143 where

$$2144 \quad S_r = k_B \left\{ N_{tot} \ln \left(\frac{N_{tot}}{\Delta^3 r} \right) - \int d^3 r n(\mathbf{r}) \ln[n(\mathbf{r})] \right\}, \quad (54)$$

$$2145 \quad S_v = \int d^3 r s_v(\mathbf{r}), \quad (55)$$

$$2146 \quad s_v(\mathbf{r}) = k_B \left\{ n(\mathbf{r}) \ln \left[\frac{n(\mathbf{r})}{\Delta^3 v} \right] - \int d^3 v f(\mathbf{r}, \mathbf{v}) \ln[f(\mathbf{r}, \mathbf{v})] \right\}. \quad (56)$$

2147 Here, $\Delta^3 r$ and $\Delta^3 v$ are the position and velocity space volume elements of phase space,
 2148 $f(\mathbf{r}, \mathbf{v})$ is the distribution function, and $n(\mathbf{r})$ is the number density. Eq. (56) is the
 2149 velocity-space entropy density and its last term is often referred to as the total kinetic
 2150 entropy density, $s = -k_B \int d^3 v f(\mathbf{r}, \mathbf{v}) \ln[f(\mathbf{r}, \mathbf{v})]$ (Kaufmann and Paterson 2009).

2151 The entropy of a measured distribution can be compared with that of an equivalent
 2152 drifting Maxwellian distribution described by (omitting the dependence on \mathbf{r})

$$2153 \quad f_M(\mathbf{v}) = n \left(\frac{m}{2\pi k_B T} \right)^{3/2} e^{-m(\mathbf{v}-\mathbf{u})^2/(2k_B T)}, \quad (57)$$

2154 where m is the particle mass, \mathbf{u} is the bulk flow velocity, and T is the effective
 2155 temperature. Combining Eq. (57) with Eq. (56) to calculate the total and velocity-space
 2156 entropy densities of a Maxwellian distribution (s_M and $s_{M,V}$, respectively) yields

$$2157 \quad s_M = \frac{3}{2} k_B n \left[1 + \ln \left(\frac{2\pi k_B T}{mn^{3/2}} \right) \right], \quad (58)$$

$$2158 \quad s_{M,V} = \frac{3}{2} k_B n \left[1 + \ln \left(\frac{2\pi k_B T}{m(\Delta^3 v)^{3/2}} \right) \right]. \quad (59)$$

2159 The difference between the equivalent Maxwellian and measured total and velocity-
 2160 space entropy densities defines two non-Maxwellianity parameters

$$2161 \quad \bar{M}_{KP} = \frac{s_M - s}{(3/2)k_B T}, \quad (60)$$

$$2162 \quad \bar{M} = \frac{s_{M,V} - s_v}{s_{M,V}}, \quad (61)$$

2163 where the Kaufmann and Paterson non-Maxwellianity, \bar{M}_{KP} , is normalized by the
 2164 internal energy per particle of an ideal gas (Kaufmann and Paterson 2009), and \bar{M} is
 2165 normalized by the velocity space Maxwellian entropy density (Liang et al. 2020). While
 2166 \bar{M} is bounded between 0 and 1 and so provides a better measure for making comparisons
 2167 of non-Maxwellianity between distributions, the normalization of \bar{M}_{KP} better relates

entropy to the energetics of the system (Cassak et al. 2023).

The development so far has considered uniform velocity space grids typical of theory and simulations. Particle detectors, on the other hand, have logarithmically spaced energy bins. Because of this, the velocity space volume element depends on velocity: $d^3v(\mathbf{v})$. Revisiting the above derivations in spherical velocity space coordinates leads to (Argall et al. 2022)

$$s_v = s + k_B n \ln n - k_B \int d^3v(\mathbf{v}) f(\mathbf{v}) \ln[d^3v(\mathbf{v})], \quad (62)$$

$$\bar{M} = \frac{s_M - s - k_B \int d^3v(\mathbf{v}) \ln[d^3v(\mathbf{v})] [f_M(\mathbf{v}) - f(\mathbf{v})]}{1 + k_B n \ln n - k_B \int d^3v(\mathbf{v}) \ln[d^3v(\mathbf{v})] f_M(\mathbf{v})}. \quad (63)$$

A number of corrections are required when integrating the measured particle distribution functions. These include corrections for photoelectrons and spacecraft potential, and normalization of the energy and look-angle space of the instrument (FPI in the case of MMS). The subsequent spherical, normalized energy space is obtained by applying the transformations outlined in Moseev et al. (2019), and Argall et al. (2022) and its Supplemental Material. In addition, to calculate the equivalent Maxwellian distribution, it is essential to create a look-up table to minimize numerical errors (Argall et al. 2022).

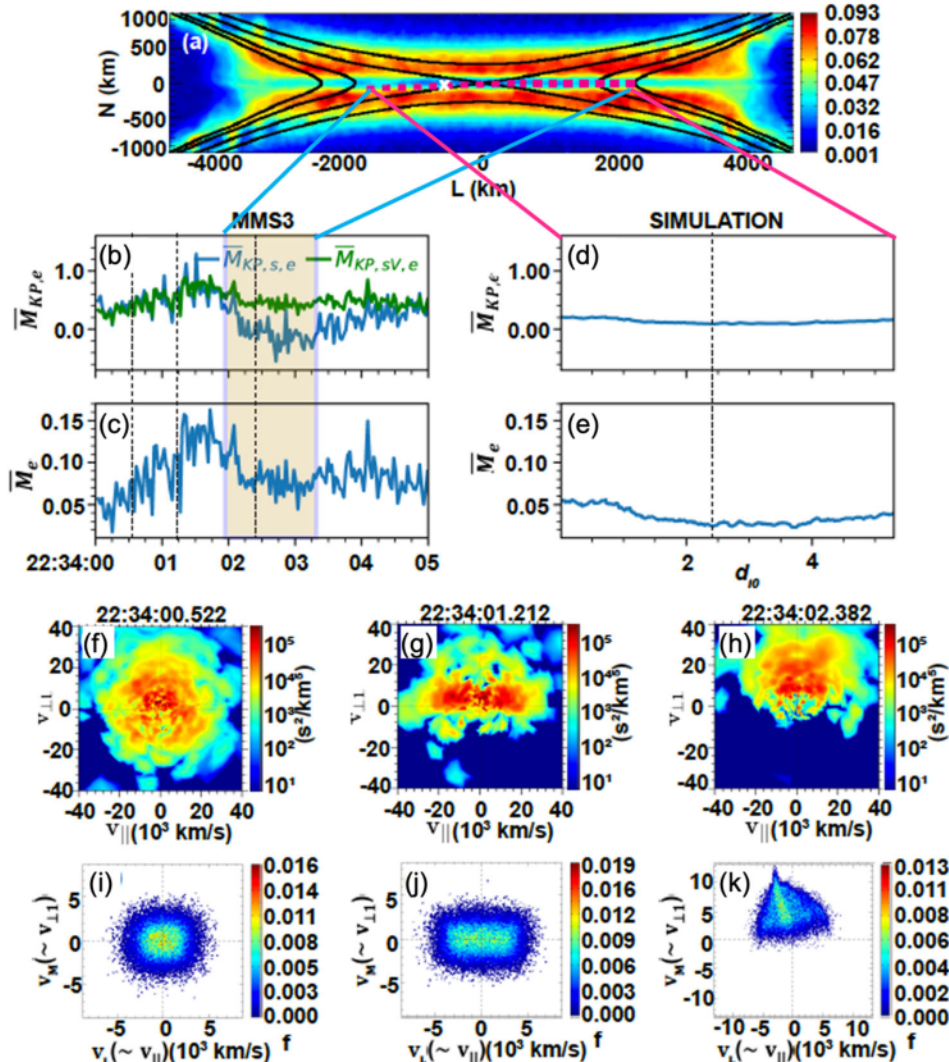
Figure 25 shows calculations of non-Maxwellianity from MMS observations and PIC simulations within the EDR of a magnetotail reconnection event. The 2D profile of \bar{M} (panel a) shows significant departures from Maxwellianity in the vicinity of the EDR, indicating that important kinetic effects are taking place. The trajectory (magenta dashed line) indicates the path that MMS took through the EDR and the corresponding data is shown in the following panels. Three different measures of non-Maxwellianity, including \bar{M} and \bar{M}_{KP} show qualitative agreement between observations and simulations.

Distribution functions observed by MMS (Figure 25f,g,h) and in PIC (Figure 25k) are taken at the black vertical dashed lines (and the “x” in panel a). PIC distributions (Figure 25i,j) outside the area shown in Figure 25a were taken from regions representative of the MMS locations within the reconnection domain. The electron distribution functions are from the upstream (Figure 25f,i), inflow (Figure 25g,j), and X-line (Figure 25h,k) regions. Upstream, the distributions are nearly Maxwellian and have the lowest non-Maxwellianity of the three regions sampled. The inflow distributions are elongated in the direction parallel to the magnetic field due to their bouncing within a parallel potential well (Egedal et al. 2010a), and X-line distributions are striated due to their meandering current sheet motion (Ng et al. 2011). This shows that entropy measures of non-Maxwellianity are able to identify regions where important kinetic effects are taking place.

Unfortunately, by breaking phase space up into discrete bins (i.e., by considering a distribution of particles instead of combinations of individual particles), we lose

information about the system; \bar{M} depends on the scale of the velocity space grids and their non-uniformity and thus is not equal to \bar{M}_{KP} . For details about how the difference between \bar{M} and \bar{M}_{KP} allows us to quantify the amount of information loss incurred by discretizing velocity space, see Argall et al. (2022). Implications include considering the thermal velocity of the target environment when designing plasma instruments and quantifying limits to observations of dissipation.

2209



2210 **Fig. 25** MMS and PIC simulation comparisons of non-Maxwellianity in a magnetotail
 2211 electron diffusion region. (a) The 2D profile of non-Maxwellianity surrounding the EDR
 2212 with the MMS trajectory shown (dotted magenta line). Different electron non-
 2213 Maxwellianity quantities as observed (b,c) by MMS and (d,e) in PIC, where \bar{M}_{KP} (Eq.
 2214 (60)) is computed using s (blue) and s_V (Eq. 62) (green). The MMS panels show a
 2215 larger view than is depicted in the simulation for comparison with other published studies.

2216 Vertical dashed lines (and the “x” in panel **a**) indicate where electron distributions were
 2217 obtained (**f,g,h**) by MMS and (**k**) in PIC simulation. PIC distributions in (**i,j**) were taken
 2218 outside of the bounds of panel (**a**) from locations representative of the regions MMS
 2219 sampled. Adapted from Argall et al. (Phys. Plasmas, 29, 022902, 2022; licensed under a
 2220 Creative Commons Attribution (CC BY) license).

2221

2222 **4.3 Reconnection Electric Field Estimation**

2223 **4.3.1 Extracting E_M from Multiple Crescents in Electron Velocity Distributions**

2224 In the event on 11 July 2017 in the Earth’s magnetotail (Torbert et al. 2018), MMS
 2225 detected multi-crescent electron VDFs in the EDR. Multi-crescent VDFs are produced
 2226 because the reconnection electric field E_M accelerates electrons while they are meandering
 2227 across the reconnecting current sheet. In the following, we explain how to extract the
 2228 information about E_M from a multi-crescent VDF.

2229 Suppose electrons are meandering in a current sheet with a magnetic field $B_L=bN$ and
 2230 a Hall electric field $E_N=-kN$, where N is the position measured from the current sheet
 2231 center ($B_L=0$) plane, and b and k are the slope of B_L and E_N , respectively, in the N direction.
 2232 Consider an electron moving back and forth in the N direction, starting from $N=0$ at $t=0$.
 2233 The velocity v_M is given as $v_M=v_{M0}-(eE_M/m_e)t-(eb/2m_e)N^2$, where v_{M0} is the initial velocity.
 2234 The N motion is an oscillatory motion under $E_N=-kN$ and the magnetic force, and
 2235 approximately described using Airy functions as $N=c_1\text{Ai}(r)+c_2\text{Bi}(r)$, where c_1 and c_2 are
 2236 constants, and r is defined as

$$2237 \quad r = -\left(\frac{e^2 E_M b}{m_e^2}\right)^{1/3} \left[t - \frac{m_e}{e E_M} \left(v_{M0} + \frac{k}{b} \right) \right]. \quad (64)$$

2238 Bessho et al. (2018) derived the equation of v_N as a function of v_M , as follows:

$$2239 \quad v_N = N \left(\frac{eb}{m_e} \right)^{1/2} \left(-v_M - \frac{eb}{2m_e} N^2 - \frac{k}{b} \right)^{1/2} \\ 2240 \quad \times \cot \left\{ \frac{2}{3} \left(\frac{eb}{m_e} \right)^{1/2} \frac{m_e}{e E_M} \left[\left(-v_M - \frac{eb}{2m_e} N^2 - \frac{k}{b} \right)^{3/2} - \left(-v_{M0} - \frac{k}{b} \right)^{3/2} \right] \right\}, \quad (65)$$

2241 which is for a case where $v_{M0} < -k/b$. In the other case, where $v_{M0} > -k/b$, we have

$$2242 \quad v_N = N \left(\frac{e^2 E_y b}{m_e^2} \right)^{1/3} \frac{\text{Bi}(r_0) \frac{d\text{Ai}(r)}{dr} - \text{Ai}(r_0) \frac{d\text{Bi}(r)}{dr}}{\text{Ai}(r_0)\text{Bi}(r) - \text{Bi}(r_0)\text{Ai}(r)}, \quad (66)$$

2243 where r_0 is the initial value of r at $N=0$. Both equations represent multiple curves in the
 2244 v_M-v_N plane, because the cot function and Airy functions Ai and Bi are oscillatory
 2245 functions.

2246 In the MMS observation of the Torbert event, the electron VDF at the neutral line
 2247 shows $v_{M0} > -k/b$; therefore, in Bessho et al. (2018) (see Figure 26), to compare the

2248 observed multi-crescent VDF with the theory, Eq. (66) was used. In the following, we
2249 will explain how to extract the reconnection electric field E_M by comparing the theory
2250 and the observed VDF.

2251 **Procedure 1:** Deriving the field quantities from observed field data

2252 From the magnetic field and electric field data, we obtain the slope b for B_L and the
2253 slope k for E_N . Figure 26a shows magnetic fields (top), electric fields (middle), and the
2254 distance from the neutral line (bottom), obtained by MMS2 and MMS3. The LMN
2255 coordinates were obtained by a hybrid method (Denton et al. 2016) of MDD (Shi et al.
2256 2005; Section 3.2.1) and MVA (Sonnerup and Scheible, 1998). The N distance was
2257 obtained by a method similar to Denton et al. (2016), from the time integral of $V_N =$
2258 $(dB_L/dt)/(\partial B_L/\partial N)$, which represents the MMS barycenter velocity relative to the current
2259 sheet. The values of b and k were obtained as $b=9.0\times 10^{-2}$ nT/km (from MMS3 data), and
2260 $k=1.2\times 10^3$ mV/km² (from MMS2 data).

2261 **Procedure 2:** Obtaining v_{M0} from the VDF at the neutral line $N=0$

2262 There are two equations, Eq. (65) and Eq. (66), depending on the value of v_{M0} . Using
2263 the VDF on the neutral line, we identify the population of electrons that have just arrived
2264 at the neutral line and started the meandering motion. Figure 26b shows the VDF at the
2265 neutral line $N=0$ ($B_L=0$ line) by MMS3, and the population near the white vertical line
2266 shows that $v_{M0}=-0.7\times 10^4$ km/s. In this event, the $E_N \times B_L$ drift velocity, $-k/b$, is $=-1.3\times$
2267 10^4 km/s; therefore, the condition $v_{M0}>-k/b$ needs to be used, and we will use Eq. (66).

2268

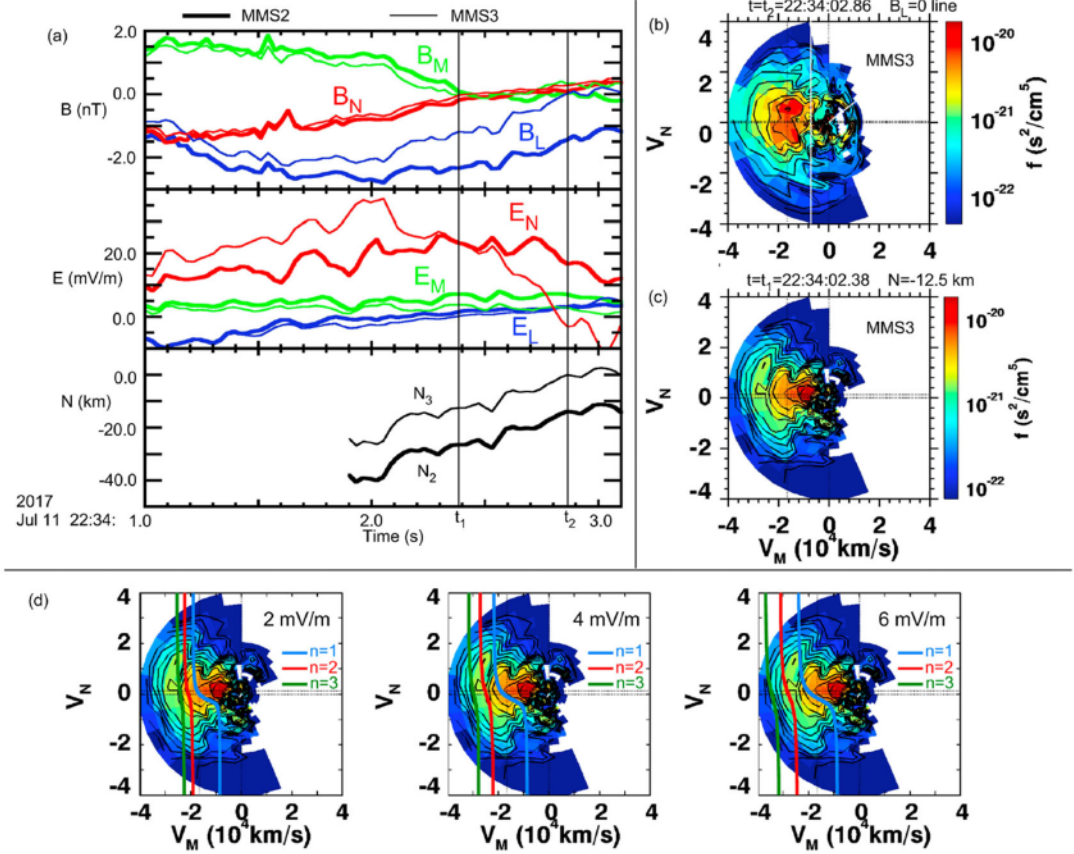


Fig. 26 MMS data in the event on 11 July 2017. (a) MMS data for the field quantities and the distance N from the neutral line. (b) Electron VDF at the neutral line. (c) VDF at $t=t_1$. (d) Comparison between the theory (blue, red, green curves by Eq. (66)) and the multi-crescent VDF. Adapted from Bessho et al. (2018).

Procedure 3: Compare the theory and the multi-crescent VDF, and determine E_M

Now, we have obtained all the required parameters, b , k , N , and v_{M0} to draw the theoretical curves on the multi-crescent VDF, except for an undetermined parameter, E_M . In this event, Figure 26c is the VDF that was compared with the theory. In the VDF, there are three crescent-like stripes. Figure 26d shows three plots with different E_M values, 2 mV/m, 4 mV/m, and 6 mV/m. Values of $E_M = 2$ mV/m and $E_M = 6$ mV/m are excluded because the separations between theoretical curves based on Eq. (66) do not match the separations in the observed VDF. In contrast, $E_M = 4$ mV/m is consistent with the observed VDF. In this way, we can determine the reconnection electric field from a multi-crescent VDF. Note that this value, $E_M = 4$ mV/m is close to the value of $E_M = 3.2$ mV/m determined by Genestreti et al. (2018), if we allow for an uncertainty of 1-2 mV/m in the MMS measurements.

2287

2288 **4.3.2 Remote Sensing at the Reconnection Separatrix Boundary**

2289 **Background:** The change of magnetic field connectivity during magnetic reconnection
 2290 occurs within the micro-scale diffusion region. Assuming that reconnection develops in
 2291 the x - z plane (Figure 27), the y -component of the electric field E_y around the diffusion
 2292 region matches the convectional electric field at the inflow and outflow regions to
 2293 conserve the magnetic flux, $E_y \sim -u_{\text{in}}B_{\text{in}} \sim -u_{\text{out}}B_{\text{out}}$ where u_{in} , u_{out} and B_{in} , B_{out} are the
 2294 plasma flow speeds and the magnetic field strengths, respectively, at the boundaries of
 2295 the diffusion region and subscripts “in” and “out” mean the inflow and outflow
 2296 boundaries, respectively. The magnitude of E_y , which represents the flux transfer rate
 2297 from the inflow region into the diffusion region, is called the reconnection electric field
 2298 E_r or the unnormalized reconnection rate. Near the center of the diffusion region called
 2299 the EDR, E_r is sustained by the non-ideal component of the generalized Ohm’s law as E_r
 2300 $\sim |E'_y| = |E_y + (\mathbf{u}_e \times \mathbf{B})_y|$. High-resolution in-situ observations by MMS successfully
 2301 encountered the EDR and directly measured E_y near the EDRs in Earth’s magnetopause
 2302 (e.g., Burch et al. 2016b) and magnetotail (e.g., Torbert et al. 2018) current sheets.
 2303 Statistically, it is relatively rare to encounter these small regions and measure E_r directly.
 2304 To meet this challenge, a new technique for estimating E_r using in-situ measurements at
 2305 the reconnection separatrix boundary was recently proposed (Nakamura et al., 2018a).
 2306 Since the extent of the separatrix is longer than the micro-scale EDR, the probability for
 2307 encountering the separatrix is much greater than that for the EDR.

2308 **Methods:** Ignoring variations in the out-of-plane direction, then E_r , which corresponds to
 2309 E_y at the X-line, can be written as

$$2310 \quad E_r = -E_{y,x-\text{line}} = \frac{\partial A_{y,x-\text{line}}}{\partial t} \sim \frac{\partial A_{ys}}{\partial t}, \quad (67)$$

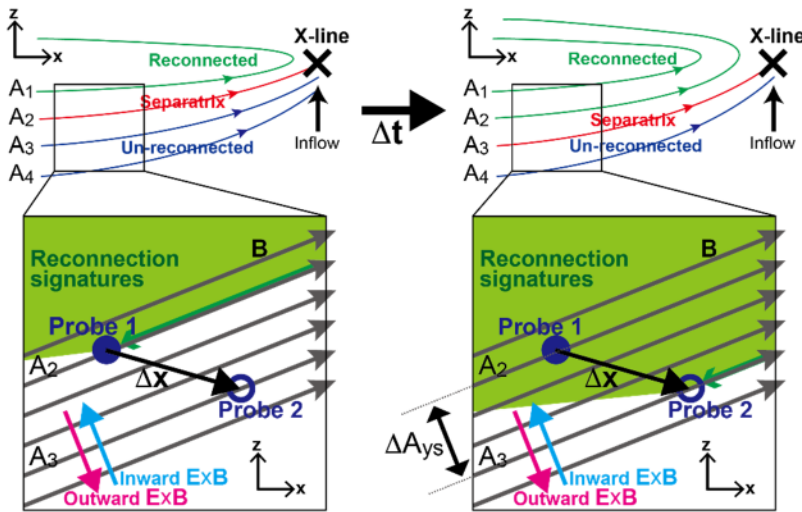
2311 where $A_{y,x-\text{line}}$ is the out-of-plane component of the vector potential at the X-line and
 2312 A_{ys} is the potential at the separatrix. Note that in the 2-D limit, the potential at the X-line
 2313 is constant along the reconnection separatrix boundary (Vasylinas 1975). Since the
 2314 separatrix may be moving relative to observing spacecraft because of structure motion
 2315 (see Figure 27), by sequentially obtaining the potential at the separatrix by two different
 2316 probes that are separated in the boundary normal direction, E_r can be estimated as $E_r \sim$
 2317 $\Delta A_{ys} / \Delta t$. Here Δt is the time difference between the separatrix detections by the two
 2318 probes and ΔA_{ys} (corresponding to $A_3 - A_2$ in Figure 27) is the difference of A_{ys} between the
 2319 probes during this separatrix crossing. Defining the separation of the two probes as
 2320 $\Delta \mathbf{x} = (\Delta x, \Delta z)$, as illustrated in Figure 27, and assuming: (i) a constant reconnection rate
 2321 during Δt , and (ii) the uniform electric and magnetic fields between the two probes, then

2322 ΔA_{ys} can be estimated as $\Delta A_{ys} \sim (\Delta \mathbf{X} \times \mathbf{B})_y$, where $\Delta \mathbf{X} = \Delta \mathbf{x} - \mathbf{V}_c \Delta t$ takes out the effect of
 2323 background structural motion in the $\mathbf{E} \times \mathbf{B}$ drift velocity, $\mathbf{V}_c = (\mathbf{E} \times \mathbf{B})/B^2$. Then, from Eq.
 2324 (67), E_r can be described as,

2325
$$E_r \sim \frac{(\Delta \mathbf{X} \times \mathbf{B})_y}{\Delta t} = [-(\mathbf{V}_{tim} - \mathbf{V}_c) \times \mathbf{B}]_y = -B_x \frac{\Delta z}{\Delta t} + B_z \frac{\Delta x}{\Delta t} + B_x \left(\frac{\mathbf{E} \times \mathbf{B}}{B^2} \right)_z - B_z \left(\frac{\mathbf{E} \times \mathbf{B}}{B^2} \right)_x, \quad (68)$$

2326 where $\mathbf{V}_{tim} = \Delta \mathbf{x} / \Delta t$ is the separatrix velocity from the timing analysis. Eq. (68) suggests
 2327 that if two probes that are separated in the normal direction sequentially detect the
 2328 separatrix signatures, the reconnection electric field E_r can be remotely estimated
 2329 (Nakamura et al. 2018a).

2330



2331 **Fig. 27** Schematic of a reconnecting current sheet in motion in the x - z plane during Δt ,
 2332 focusing on a region near the separatrix boundary where two probes separated by Δx
 2333 sequentially detect the separatrix signatures (adapted from Nakamura et al. (2018a)). The
 2334 field line motion ($\mathbf{E} \times \mathbf{B}$ drift velocity) can be inward (cyan arrow) or outward (magenta
 2335 arrow), depending on the magnitude of the reconnection electric field and the magnitude
 2336 and direction of the structure velocity.

2337

2338 **Applications:** In Nakamura et al. (2018a), the proposed technique was first tested using
 2339 virtual satellites in a 2-D fully kinetic PIC simulation of reconnection without a guide
 2340 field. To identify separatrix boundaries from observation data, Nakamura et al. (2018a)
 2341 proposed to detect high-energy parallel electron beams that stream away from the X-line
 2342 along the separatrix and resulting enhancements of the B_y component (Hall fields). The
 2343 remotely estimated E_r from virtual observations for both electron beams and Hall fields
 2344 indeed agree well with the directly obtained E_r at the X-line, indicating the adequacy of

2346 this remote sensing technique.

2347 In real in-situ observations, this technique requires sufficiently high-cadence
2348 magnetic and electric field data under an assumption that temporal and spatial variations
2349 of the fields while obtaining \mathbf{V}_{tim} (i.e., while multi-probes sequentially detect the
2350 separatrix) are negligible. The MMS mission satisfies this requirement with its burst
2351 mode magnetic (Russell et al. 2016) and electric (Ergun et al. 2016; Lindqvist et al. 2016;
2352 Torbert et al. 2016a) field measurements and its small inter-spacecraft separation (10^{1-2}
2353 km). The plasma particle measurements at burst mode cadences (Pollock et al., 2016) are
2354 also useful to detect signatures of the separatrix such as parallel electron beams (Varsani
2355 et al. 2017). Nakamura et al. (2018a) first applied this technique to an MMS observation
2356 event on 10 August 2016 of the plasma sheet crossing in the near-Earth region
2357 accompanied by a strong substorm, which was initially reported by Nakamura et al.
2358 (2017). By identifying the separatrix boundary from the Hall field enhancements, they
2359 estimated the reconnection electric field as $E_r \sim 15 \pm 5$ mV/m. Wellenzohn et al. (2021)
2360 applied this technique to another MMS plasma sheet crossing event accompanied by a
2361 small substorm on 12 July 2018. By identifying the separatrix boundary from high-energy
2362 parallel electron beams and resulting electric field disturbances, they estimated $E_r \sim 2 \pm 0.5$
2363 mV/m. In another example, Nakamura et al. (2018b) focused on the magnetotail EDR
2364 crossing event by MMS on 11 July 2017 accompanied by a small substorm, which was
2365 initially reported by Torbert et al. (2018). In this event, E_r can be obtained not only from
2366 the remote sensing technique at the separatrix near the EDR, but also from the direct
2367 measurement within the EDR. The obtained E_r values from remote and direct methods
2368 both are in the range 2.5 ± 0.5 mV/m. These initial results of the remote sensing technique
2369 performed using MMS observations suggest a positive correlation between E_r and the
2370 intensity of substorms. A future statistical approach is required to comprehensively
2371 establish the relation between the local reconnection E_r and the geomagnetic disturbances.
2372

2373 **4.3.3 Separatrix Angle Related to Reconnection Rate**

2374 The reconnection electric field normalized by $V_{A0}B_0$, where B_0 is the background
2375 reconnecting magnetic field and V_{A0} is the upstream Alfvén speed based on B_0
2376 ($R \sim E_r/V_{A0}B_0$), measures how fast the connectivity changes during reconnection and it
2377 is generally called the normalized reconnection rate. Considering the force balance along
2378 the inflow and outflow directions at the meso-scale in the $\beta \ll 1$ limit, Liu et al. (2017)
2379 derived a general theory showing that for symmetric reconnection R is related to the
2380 separatrix opening angle θ near the IDR as,

2381

$$R \sim \frac{E_r}{V_{A0}B_0} \sim \tan \theta \left(\frac{1-\tan^2 \theta}{1+\tan^2 \theta} \right)^2 \sqrt{1 - \tan^2 \theta}. \quad (69)$$

2382 Here the separatrices are assumed to be straight from the center of the diffusion region
 2383 through the observation points. Given that the adequacy of Eq. (69) was indeed confirmed
 2384 by fully kinetic simulations (e.g., Liu et al. 2017, 2018a; Nakamura et al. 2018b), this
 2385 theory implies that the reconnection rate R can be obtained by measuring the opening
 2386 angle θ at an ion-scale distance from the X-line.

2387 As sketched in Figure 28a, the separatrix opening angle θ just outside the IDR needed
 2388 in Eq. (69) matches the flaring angle $\tan^{-1}(|B_{Ns}|/|B_{Ls}|)$ made by the magnetic fields
 2389 adjacent to the separatrix (\mathbf{B}_s), which also matches the flaring angle $\tan^{-1}(|B_{Nd}|/|B_{Ld}|)$
 2390 made by the magnetic fields at the upstream/downstream edge of the diffusion region
 2391 (\mathbf{B}_d). In light of these relations, Nakamura et al. (2018b) introduced the following
 2392 quantity f_r , that is a function of $|B_N|/|B_L|$ measured along the spacecraft path,

2393

$$f_r \left(\frac{|B_N|}{|B_L|} \right) \sim \frac{|B_N|}{|B_L|} \left(\frac{1 - \left(\frac{|B_N|}{|B_L|} \right)^2}{1 + \left(\frac{|B_N|}{|B_L|} \right)^2} \right)^2 \sqrt{1 - \left(\frac{|B_N|}{|B_L|} \right)^2}. \quad (70)$$

2394 They then applied this function to estimate the reconnection rate R in the magnetotail
 2395 EDR crossing event by MMS on 11 July 2017 (Torbert et al. 2018). This function gives
 2396 R whenever the spacecraft crosses the separatrix near the diffusion region; i.e., where
 2397 $|B_N|/|B_L| = |B_{Ns}|/|B_{Ls}|$. Thus, R can be estimated by detecting the separatrix signature
 2398 and computing f_r at that time. In Nakamura et al. (2018b), the separatrix boundary was
 2399 accurately deduced using close comparisons with a fully kinetic simulation of this MMS
 2400 event. The reconnection rate R was then successfully obtained as $R \sim 0.15-0.2$ (Figure 28b),
 2401 which indeed agrees well with the rate directly observed within the EDR (Genestreti et
 2402 al. 2018).

2403 Note that this technique of estimating the normalized reconnection rate R would be
 2404 applicable only in a limited region where the separatrix opening angle is sufficiently close
 2405 to the exhaust opening angle critical to the rate. This condition would be satisfied just
 2406 outside the edge of the IDR as sketched in Figure 28a. In addition, since the separatrix
 2407 line in the LN plane is nearly straight from outside the IDR toward the corner of the EDR
 2408 (Nakamura et al. 2018b), this condition would be satisfied even within the IDR.

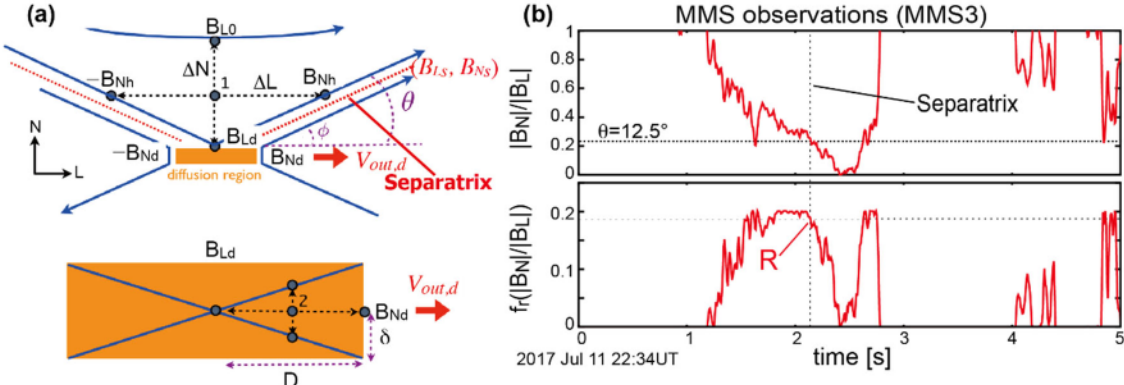


Fig. 28 (a) Sketch of the reconnection geometry around the diffusion region (adapted from Liu et al. (2017)). (b) MMS observations of $|B_N|/|B_L|$ and f_r (Eq. (70)) during the separatrix crossing on 11 July 2017 (adapted from Nakamura et al. (2018b)).

5. Summary and Outlook

Most of the methods discussed in the present review have not yet been extensively used in the analysis of in-situ data, including from the MMS mission. Thus, our hope is that the use of these methods will help advance our understanding of magnetic reconnection and associated processes in space, including wave excitation and particle acceleration, their feedback on the reconnection process, and coupling to macro-scale phenomena. Further improvement of the methodology would also be expected. In particular, since the MMS mission has focused essentially on electron-scale processes, cross-scale aspects of magnetic reconnection have not been well explored to date. Thus, there is vast room for the future development of data analysis methods to understand these multi-scale processes. See, for example, Broeren et al. (2021) for a potentially multi-scale method that can reconstruct a 3D magnetic field when more than four spacecraft are available.

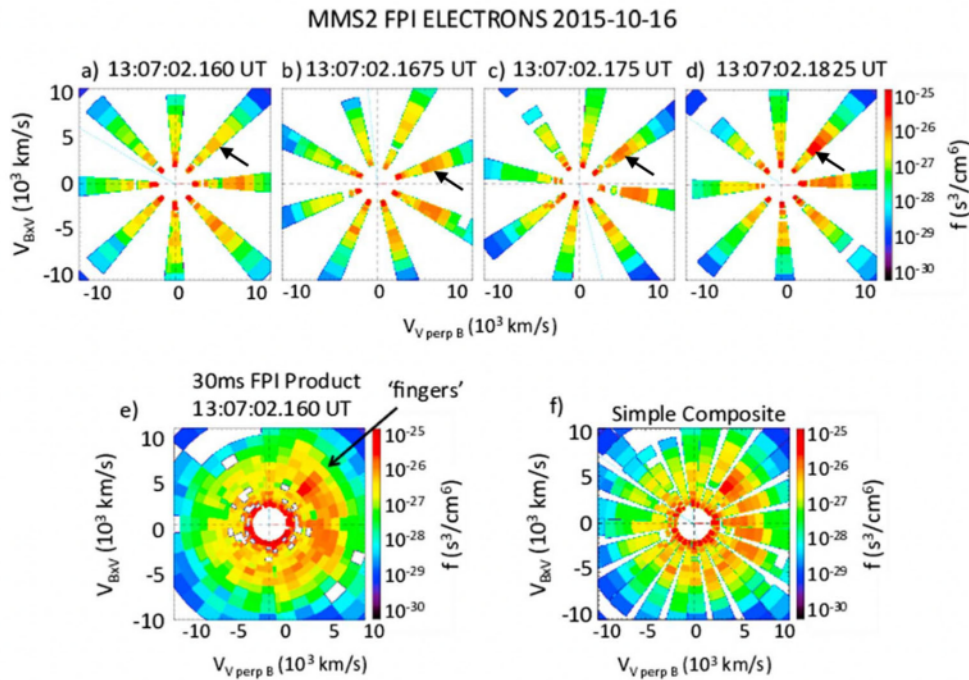
Appendix A The MMS “Quarter Moments” Data Product

The Fast Plasma Investigation (FPI) on the MMS mission was designed to measure three-dimensional electron (ion) phase space densities every 30 (150) ms. This high data rate is achieved by arranging 8 electrostatic analyzers (ESA) for each species around the spacecraft, where the field-of-view of each ESA can be electrostatically deflected to four uniformly spaced look directions spanning 45 degrees. The high voltage power supply executes a full energy sweep (from ~ 10 eV to ~ 30 keV) for each of the four deflection states, so that the suite of analyzers simultaneously samples 8 uniformly spaced azimuthal

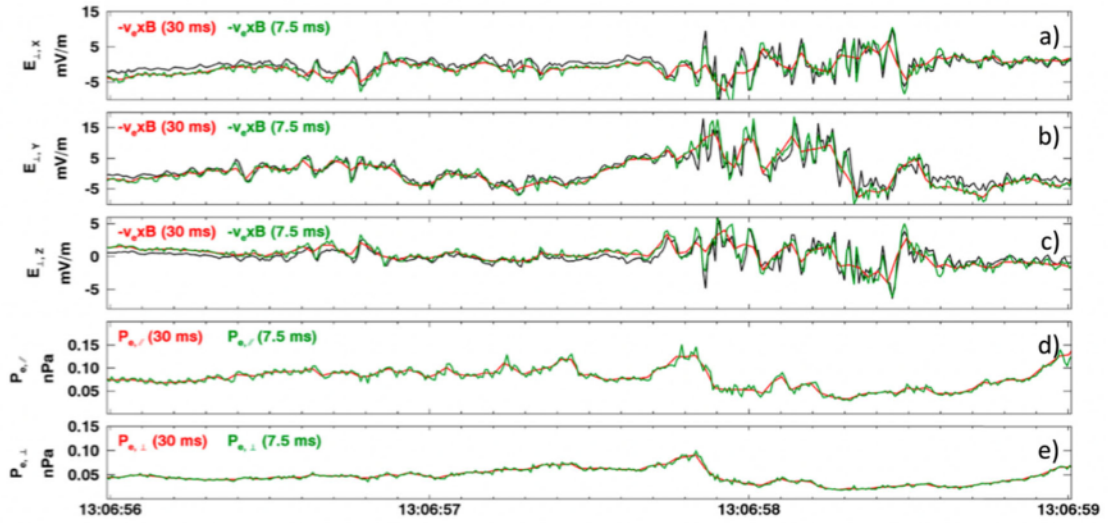
2437 angles for each energy sweep. This means that FPI samples a $32 \times 16 \times 8$ regular (energy,
 2438 zenith, azimuth) array every 7.5 (37.5) ms for electrons (ions), allowing for the possibility
 2439 of recovering plasma moments a factor of 4 times faster than the nominal 30 (150) ms
 2440 cadence. Figure 29 illustrates how the four deflection states are combined into the final
 2441 FPI Level 2 phase space density “skymaps.”

2442 To recover 3D plasma moments at 7.5 (37.5) ms for electrons (ions), we use cubic
 2443 spline interpolation to reconstruct 32 azimuthal samples – independently for each energy
 2444 and zenith – from the 8 azimuthal samples corresponding to a single deflection state. To
 2445 mitigate spline boundary condition issues, we interpolate an augmented set of data over
 2446 the domain $[-2\pi, 3\pi]$ in which data from $[0, 2\pi]$ is copied to $[-2\pi, 0]$ and $[2\pi, 3\pi]$. The
 2447 interpolated data is then passed to the production moments algorithm as a (32 energy) \times
 2448 (16 zenith) \times (32 azimuth) array.

2449



2450 **Fig. 29** The four FPI electrostatic deflection states (top four images), each composed of
 2451 a full 32-step energy sweep and obtained at 7.5 ms cadence for electrons, are combined
 2452 to produce a full Level 2 “skymap” (bottom left images) every 30 ms (adapted from Rager
 2453 et al. 2018).



2455 **Fig. 30** The spline interpolation technique does an excellent job of recovering electron
 2456 bulk velocity at 7.5 ms resolution (green line) (adapted from Rager et al. 2018). The top
 2457 three panels show three components of the electron convective electric field at 30 ms
 2458 (red) and 7.5 ms (green) resolutions. The perpendicular electric field measured by the
 2459 double probe instruments (Ergun et al. 2016; Lindqvist et al. 2016), averaged down to 7.5
 2460 ms, is shown in black. The bottom two panels show the electron pressures in the directions
 2461 parallel and perpendicular to the magnetic field.

2462

2463 Figure 30 shows a validation test in which 7.5 ms perpendicular electron bulk velocity
 2464 data is compared to the $E \times B$ drift velocity (from the electric field and magnetometer
 2465 experiments averaged down to 7.5 ms). The agreement is excellent, demonstrating that
 2466 this is a simple, robust method for extracting accurate plasma moments. These “quarter
 2467 moment” products have been used in many MMS publications (e.g., Phan et al. 2018).

2468

2469 **Appendix B Tables Summarizing Methods** (attached at the end)

2470

2471 **Acknowledgements**

2472 The work by H.H. was supported by JSPS Grant-in-aid for Scientific Research
 2473 KAKENHI 21K03504. Part of the work done while H.H. was at SwRI was supported by
 2474 NASA Contract No. NNG04EB99C at SwRI. R.E.D. was supported by a NASA grant
 2475 80NSSC22K1109. The work by D.B.K. has been supported by the Austrian Science Fund
 2476 (FWF): I 3506-N27 and Austrian FFG project ASAP15/873685. T.C.L. was supported by
 2477 NSF award AGS-2000222. T.K.M.N. was supported by the Austrian Research Fund

2478 (FWF) P32175-N27. S.M.P was supported by Contract 499935Q. Y.Q. was supported by
2479 NASA MMS mission NNG04EB99C. The authors acknowledge the International Space
2480 Science Institute in Bern for supporting the international team of the workshop “Magnetic
2481 Reconnection: Explosive Energy Conversion in Space Plasmas”.

2482

2483 **Compliance with Ethical Standards**

2484 The authors declare they have no conflicts of interest.

2485

2486 **References**

- 2487 V.A. Andreeva, N.A. Tsyganenko, Journal of Geophysical Research: Space Physics, **121**,
2488 2249–2263 (2016). <https://doi.org/10.1002/2015JA022242>
- 2489 M.R. Argall, C.R. Small, S. Piatt, et al., Frontiers in Astronomy and Space Sciences, **7**,
2490 54 (2020). <https://doi.org/10.3389/fspas.2020.00054>
- 2491 M.R. Argall, M.H. Barbuiya, P.A. Cassak, et al., Phys. Plasmas, **29**, 022902 (2022).
2492 <https://doi.org/10.1063/5.0073248>
- 2493 N. Aunai, M. Hesse, M. Kuznetsova, Phys. Plasmas, **20**, 092903 (2013).
2494 <https://doi.org/10.1063/1.4820953>
- 2495 D.N. Baker, L. Riesberg, C.K. Pankratz, R.S. Panneton, B.L. Giles, F.D. Wilder, R.E.
2496 Ergun, Space Science Reviews, **199**, 545–575 (2016).
2497 <https://doi.org/10.1007/s11214-014-0128-5>
- 2498 R. Bandyopadhyay, A. Chasapis, W. H. Matthaeus, et al., Phys. Plasmas, **28**, 112305
2499 (2021). <https://doi.org/10.1063/5.0071015>
- 2500 M.H. Barbuiya, P.A. Cassak, Phys. Plasmas, **29**, 122308 (2022).
2501 <https://doi.org/10.1063/5.0125256>
- 2502 M.H. Barbuiya, P.A. Cassak, M.A. Shay, et al., Journal of Geophysical Research: Space
2503 Physics, **127**, e2022JA030610 (2022). <https://doi.org/10.1029/2022JA030610>
- 2504 N. Bessho, L.-J. Chen, M. Hesse, Geophysical Research Letters, **43**(5), 1828–1836 (2016).
2505 <https://doi.org/10.1002/2016gl067886>
- 2506 N. Bessho, L.-J. Chen, S. Wang, M. Hesse, Geophysical Research Letters, **45**, 12142–
2507 12152 (2018). <https://doi.org/10.1029/2018GL081216>
- 2508 L. Boltzmann, Wiener Berichte, **76**, 373–435 (1877).
- 2509 J.E. Borovsky, and K. Yakymenko, Journal of Geophysical Research: Space Physics,
2510 **122**(3), 2973-2998 (2017). <https://doi.org/10.1002/2016JA023625>
- 2511 T. Broeren, K.G. Klein, J.M. TenBarge, I. Dors, O.W. Roberts, D. Verscharen, Front.
2512 Astron. Space Sci., **8**, 727076 (2021). <https://doi.org/10.3389/fspas.2021.727076>

- 2513 I. Brown, C. Mues, Expert Systems with Applications, **39**, 3446-3453 (2012).
 2514 <https://doi.org/10.1016/j.eswa.2011.09.033>
- 2515 M. Buhmann, Radial Basis Functions: Theory and Implementations, Cambridge Univ.
 2516 Press, Cambridge, U. K. (2003).
- 2517 J.L. Burch, T.E. Moore, R.B. Torbert, B.L. Giles, Space Sci. Rev., **199**(1–4), 5-21 (2016a).
 2518 <https://doi.org/10.1007/s11214-015-0164-9>
- 2519 J.L. Burch, R.B. Torbert, T.D. Phan, et al., Science, **352**(6290), aaf2939 (2016b).
 2520 <https://doi.org/10.1126/science.aaf2939>
- 2521 J.L. Burch, J.M. Webster, M. Hesse, et al., Geophysical Research Letters, **47**,
 2522 e2020GL089082 (2020). <https://doi.org/10.1029/2020GL089082>
- 2523 F. Califano, G. Manfredi, F. Valentini, J. Plasma Phys., **82**, 701820603 (2016).
 2524 <https://doi.org/10.1017/S002237781600115X>
- 2525 P.A. Cassak, M.H. Barbhuiya, Phys. Plasmas, **29**, 122306 (2022).
 2526 <https://doi.org/10.1063/5.0125248>
- 2527 P.A. Cassak, M.H. Barbhuiya, H. Liang, M.R. Argall, Phys. Rev. Lett., **130**, 085201
 2528 (2023). <https://doi.org/10.1103/PhysRevLett.130.085201>
- 2529 S.S. Cerri, Plasma turbulence in the dissipation range-theory and simulations (Universität
 2530 Ulm) (2016). <http://dx.doi.org/10.18725/OPARU-3355>
- 2531 H. Che, J.F. Drake, M. Swisdak, Nature, **474**, 184-187 (2011).
 2532 <https://doi.org/10.1038/nature10091>
- 2533 G.-W. Chen, L.-N. Hau, Journal of Geophysical
 2534 Research: Space Physics, **123**, 7358-7369 (2018).
<https://doi.org/10.1029/2018JA025842>
- 2535 L.-J. Chen, N. Bessho, B. Lefebvre, et al., Journal of Geophysical Research, **113**, A12213
 2536 (2008). <https://doi.org/10.1029/2008JA013385>
- 2537 L.-J. Chen, M. Hesse, S. Wang, N. Bessho, W. Daughton, Geophysical Research Letters,
 2538 **43**, 452–461 (2016). <https://doi.org/10.1002/2016GL068243>
- 2539 W. Chen, X. Wang, N.A. Tsyganenko, V.A. Andreeva, V.S. Semenov, Journal of
 2540 Geophysical Research: Space Physics, **124**, 10141-10152 (2019).
 2541 <https://doi.org/10.1029/2019JA027078>
- 2542 Y. Chen, G. Tóth, H. Hietala, et al., Earth and Space Science, **7**, e2020EA001331
 2543 (2020). <https://doi.org/10.1029/2020EA001331>
- 2544 I.K. Cheng, N. Achilleos, A. Smith, Front. Astron. Space Sci., **9**, 1016453 (2022).
 2545 <https://doi.org/10.3389/fspas.2022.1016453>
- 2546 D.C. Chin, Opt. Eng., **38**, 606–611 (1999). <https://doi.org/10.1117/1.602104>
- 2547 F. De Hoffmann, and E. Teller, Phys. Rev., **80**(4), 692–703 (1950).
 2548 <https://doi.org/10.1103/physrev.80.692>

- 2549 R.E. Denton, B.U.Ö. Sonnerup, H. Hasegawa, et al., Geophys. Res. Lett., **43**, 5589-5596
2550 (2016). <https://doi.org/10.1002/2016GL069214>
- 2551 R.E. Denton, B.U.Ö. Sonnerup, C.T. Russell, et al., Journal of Geophysical Research: Space
2552 Physics, **123**, 2274-2295 (2018). <https://doi.org/10.1002/2017JA024619>
- 2553 R.E. Denton, R.B. Torbert, H. Hasegawa, et al., Journal of Geophysical Research: Space
2554 Physics, **125**, e2019JA027481 (2020). <https://doi.org/10.1029/2019JA027481>
- 2555 R.E. Denton, R.B. Torbert, H. Hasegawa, et al., J. Geophys. Res. Space Physics, **126**,
2556 e2020JA028705 (2021). <https://doi.org/10.1029/2020JA028705>
- 2557 R.E. Denton, Y.-H. Liu, H. Hasegawa, R.B. Torbert, W. Li, S.A. Fuselier, J.L. Burch, J.
2558 Geophys. Res. Space Physics, **127**, e2022JA030512
2559 (<https://doi.org/10.1029/2022JA030512>)
- 2560 M.W. Dunlop, T.I. Woodward, Multi-spacecraft discontinuity analysis: Orientation and
2561 motion. in *Analysis methods for multi-spacecraft data*, edited by G. Paschmann & P.
2562 Daly, pp. 271–306, Switzerland: International Space Science Institute, SR-001 (1998).
- 2563 M.W. Dunlop, D.J. Southwood, K.-H. Glassmeier, and F.M. Neubauer, Advances in Space
2564 Research, **8**, 273-277 (1988). [https://doi.org/10.1016/0273-1177\(88\)90141-X](https://doi.org/10.1016/0273-1177(88)90141-X)
- 2565 M.W. Dunlop, A. Balogh, K.-H. Glassmeier, P. Robert, J. Geophys. Res., **107**, 1384
2566 (<https://doi.org/10.1029/2001JA005088>)
- 2567 M.W. Dunlop, Q.-H. Zhang, Y.V. Bogdanova, et al., Ann. Geophys., **29**, 1683-1697 (2011).
2568 (<https://doi.org/10.5194/angeo-29-1683-2011>)
- 2569 J. Egedal, A. Lê, Y. Zhu, et al., Geophysical Research Letters, **37**, L10102 (2010a).
2570 (<https://doi.org/10.1029/2010GL043487>)
- 2571 J. Egedal, A. Lê, N. Katz, L.-J. Chen, B. Lefebvre, W. Daughton, A. Fazakerley, Journal
2572 of Geophysical Research: Space Physics, **115**, A03214 (2010b).
2573 (<https://doi.org/10.1029/2009JA014650>)
- 2574 J. Egedal, A. Le, W. Daughton, et al., Phys. Rev. Lett., **117**, 185101 (2016).
2575 (<https://doi.org/10.1103/PhysRevLett.117.185101>)
- 2576 J. Egedal, J. Ng, A Le, et al., Phys. Rev. Lett., **123**, 225101 (2019).
2577 (<https://doi.org/10.1103/PhysRevLett.123.225101>)
- 2578 S. Ekawati, D. Cai, Journal of Geophysical Research: Space Physics, **128**,
2579 e2021JA029571 (2023). (<https://doi.org/10.1029/2021JA029571>)
- 2580 R.E. Ergun, S. Tucker, J. Westfall, et al., Space Science Reviews, **199**(1-4), 167–188
2581 (2016). (<https://doi.org/10.1007/s11214-014-0115-x>)
- 2582 E. Eriksson, A. Vaivads, D.B. Graham, et al., Geophys. Res. Lett., **45**, 8081– 8090 (2018)
2583 (<https://doi.org/10.1029/2018GL078660>)

- 2584 C.P. Escoubet, R. Schmidt, M.L. Goldstein, Space Science Reviews, **79**, 11-32 (1997).
2585 https://doi.org/10.1007/978-94-011-5666-0_1
- 2586 S. Fadanelli, B. Lavraud, F. Califano, et al., Journal of Geophysical Research: Space
2587 Physics, **124**, 6850-6868 (2019). <https://doi.org/10.1029/2019JA026747>
- 2588 S. Fadanelli, B. Lavraud, F. Califano, et al., Journal of Geophysical Research: Space
2589 Physics, **125**, e2020JA028333 (2020). <https://doi.org/10.1029/2020JA028333>
- 2590 J.H. Friedman, Ann. Statist., **29**(5), 1189-1232 (2001).
2591 <https://doi.org/10.1214/aos/1013203451>
- 2592 H.S. Fu, A. Vaivads, Y.V. Khotyaintsev, V. Olshevsky, M. André, J.B. Cao, S.Y. Huang,
2593 A. Retinò, G. Lapenta, J. Geophys. Res. Space Physics, **120**, 3758-3782 (2015),
2594 <https://doi.org/10.1002/2015JA021082>
- 2595 S.A. Fuselier, S.M. Petrinec, K.J. Trattner, Geophysical Research Letters, **27**, 473-476
2596 (2000). <https://doi.org/10.1029/1999GL003706>
- 2597 S.A. Fuselier, H.U. Frey, K.J. Trattner, S.B. Mende, J.L. Burch, Journal of Geophysical
2598 Research, **107**(A7), 1111 (2002). <https://doi.org/10.1029/2001JA900165>
- 2599 S.A. Fuselier, W.S. Lewis, C. Schiff, et al., Space Science Reviews, **199**(1–4), 77–103
2600 (2016). <https://doi.org/10.1007/s11214-014-0087-x>
- 2601 K.J. Genestreti, T.K.M. Nakamura, R. Nakamura, et al., Journal of Geophysical Research:
2602 Space Physics, **123**, 9130–9149 (2018). <https://doi.org/10.1029/2018JA025711>
- 2603 K.J. Genestreti, X. Li, Y.-H. Liu, et al., Phys. Plasmas, **29**, 082107 (2022).
2604 <https://doi.org/10.1063/5.0090275>
- 2605 D.J. Gershman, A. F-Viñas, J.C. Dorelli, et al., Wave-particle energy exchange directly
2606 observed in a kinetic Alfvén-branch wave. Nature Communications, **8**, 14719 (2017).
2607 doi:10.1038/ncomms14719.
- 2608 J.W. Gjerloev, Journal of Geophysical Research: Space Physics, **117**, A09213 (2012).
2609 <https://doi.org/10.1029/2012JA017683>
- 2610 J.T. Gosling, M.F. Thomsen, S.J. Bame, R.C. Elphic, C.T. Russell, Journal of
2611 Geophysical Research, **95**, 8073 (1990). <https://doi.org/10.1029/JA095iA06p08073>
- 2612 D.B. Graham, Y.V. Khotyaintsev, M. André, et al., Journal of Geophysical Research:
2613 Space Physics, **126**, e2021JA029260 (2021). <https://doi.org/10.1029/2021JA029260>
- 2614 D.B. Graham, Y.V. Khotyaintsev, M. André, et al., Nature Communications, **13**(2954)
2615 (2022). <https://doi.org/10.1038/s41467-022-30561-8>
- 2616 A. Greco, P. Chuychai, W.H. Matthaeus, S. Servidio, P. Dmitruk, Geophysical Research
2617 Letters, **35**, L19111 (2008). <https://doi.org/10.1029/2008GL035454>
- 2618 A. Greco, F. Valentini, S. Servidio, W.H. Matthaeus, Physical Review E, **86**(6), 066405
2619 (2012). <https://doi.org/10.1103/PhysRevE.86.066405>

- 2620 R. Guo, Z. Pu, X. Wang, C. Xiao, J. He, Journal of Geophysical Research: Space Physics,
2621 **127**, e2021JA030248 (2022). <https://doi.org/10.1029/2021JA030248>
- 2622 H. Hasegawa, Monogr. Environ. Earth Planets, **1**(2), 71-119 (2012).
2623 doi:10.5047/meep.2012.00102.0071
- 2624 H. Hasegawa, B.U.Ö. Sonnerup, M.W. Dunlop, et al., Ann. Geophys., **22**, 1251-1266
2625 (2004). <https://doi.org/10.5194/angeo-22-1251-2004>
- 2626 H. Hasegawa, B.U.Ö. Sonnerup, R.E. Denton, et al., Geophys. Res. Lett., **44**, 4566-4574
2627 (2017). <https://doi.org/10.1002/2017GL073163>
- 2628 H. Hasegawa, R.E. Denton, R. Nakamura, et al., Journal of Geophysical Research: Space
2629 Physics, **124**, 122-138 (2019). <https://doi.org/10.1029/2018JA026051>
- 2630 H. Hasegawa, T.K.M. Nakamura, R.E. Denton, Journal of Geophysical Research: Space
2631 Physics, **126**, e2021JA029841 (2021). <https://doi.org/10.1029/2021JA029841>
- 2632 H. Hasegawa, R.E. Denton, K. Dokgo, et al., Journal of Geophysical Research: Space
2633 Physics, **128**, e2022JA031092 (2023). <https://doi.org/10.1029/2022JA031092>
- 2634 L.-N. Hau, C.-K. Chang, G.-W. Chen, Astrophys. J., **900**, 97 (2020).
2635 <https://doi.org/10.3847/1538-4357/aba2d0>
- 2636 L.-N. Hau, T.-D. Phan, B.U.Ö. Sonnerup, G. Paschmann, Geophys. Res. Lett., **20**, 2255-
2637 2258 (1993). <https://doi.org/10.1029/93GL02491>
- 2638 M. Hesse, K. Schindler, J. Birn, M. Kuznetsova, Phys. Plasmas, **6**, 1781–1795 (1999).
2639 <https://doi.org/10.1063/1.873436>
- 2640 M. Hesse, T. Neukirch, K. Schindler, M. Kuznetsova, S. Zenitani, Space Sci. Rev., **160**,
2641 3-23 (2011). <https://doi.org/10.1007/s11214-010-9740-1>
- 2642 M. Hesse, N. Aunai, D.G. Sibeck, J. Birn, Geophys. Res. Lett., **41**, 8673–8680 (2014).
2643 doi:10.1002/2014GL061586
- 2644 S.V. Heuer, K.J. Genestreti, T.K.M. Nakamura, R.B. Torbert, J.L. Burch, R. Nakamura,
2645 Geophysical Research Letters, **49**,
2646 e2022GL100652. <https://doi.org/10.1029/2022GL100652>
- 2647 M. Hoshino, T. Mukai, T. Terasawa, I. Shinohara, Journal of Geophysical Research: Space
2648 Physics, **106**, 25979–25997 (2001). <https://doi.org/10.1029/2001JA900052>
- 2649 Q. Hu, B.U.Ö. Sonnerup, J. Geophys. Res., **107**(A7), (2002).
2650 <https://doi.org/10.1029/2001JA000293>
- 2651 K.-J. Hwang, E. Choi, K. Dokgo, et al., Geophysical Research Letters, **46**, 6287-6296
2652 (2019). <https://doi.org/10.1029/2019GL082710>
- 2653 K.-J. Hwang, R. Nakamura, J.P. Eastwood, J.P. et al., Space Sci Rev, **219**, 71 (2023).
2654 <https://doi.org/10.1007/s11214-023-01010-9>
- 2655 L.K. Jian, C.T. Russell, J.G. Luhmann, D. Curtis, P. Schroeder, AIP Conference

- 2656 Proceedings, **1539**, 195–198 (2013). <https://doi.org/10.1063/1.4811021>
- 2657 H. Karimabadi, W. Daughton, J. Scudder, Geophys. Res. Lett., **34**, L13104 (2007).
<https://doi.org/10.1029/2007GL030306>
- 2659 R.L. Kaufmann, W.R. Paterson, Journal of Geophysical Research: Space Physics, **114**,
2660 A00D04 (2009). <https://doi.org/10.1029/2008JA014030>
- 2661 A.V. Khrabrov, B.U.Ö. Sonnerup, DeHoffmann-Teller Analysis. in *Analysis methods for*
2662 *multi-spacecraft data*, edited by G. Paschmann & P. Daly, pp. 221–248, Bern,
2663 Switzerland: International Space Science Institute, SR-001 (1998).
- 2664 A.S. Kingsep, K.V. Chukbar, V.V. Yan'kov, in *Reviews of Plasma Physics*, edited by
2665 B.B. Kadomtsev, **16**, 243–288, Consultants Bureau, New York (1990).
- 2666 E. Kobel, E.O. Flückiger, Journal of Geophysical Research, **99**, 23617-23622 (1994).
<https://doi.org/10.1029/94JA01778>
- 2668 D.B. Korovinskiy, A.V. Divin, V.S. Semenov, N.V. Erkaev, S.A. Kiehas, I.V. Kubyshkin,
2669 Phys. Plasmas, **27**, 082905 (2020). <https://doi.org/10.1063/5.0015240>
- 2670 D.B. Korovinskiy, S.A. Kiehas, E.V. Panov, V.S. Semenov, N.V. Erkaev, A.V. Divin,
2671 I.V. Kubyshkin, Journal of Geophysical Research: Space Physics, **126**, e2020JA029045
2672 (2021). <https://doi.org/10.1029/2020JA029045>
- 2673 D. Korovinskiy, E. Panov, R. Nakamura, S. Kiehas, M. Hosner, D. Schmid, I. Ivanov,
2674 Front. Astron. Space Sci., **10**, 1069888 (2023).
<https://doi.org/10.3389/fspas.2023.1069888>
- 2676 A. Laiti, Y.V. Khotyaintsev, A.P. Dimmock, A. Johlander, D.B. Graham, V. Olshevsky,
2677 Journal of Geophysical Research: Space Physics, **127**, e2022JA030454 (2022).
<https://doi.org/10.1029/2022JA030454>
- 2679 A. Le, W. Daughton, L.-J. Chen, J. Egedal, Geophys. Res. Lett., **44**, 2096–2104 (2017).
<https://doi.org/10.1002/2017GL072522>
- 2681 A. Le, W. Daughton, O. Ohia, L.-J. Chen, Y.-H. Liu, S. Wang, W.D. Nystrom, R. Bird,
2682 Physics of Plasmas, **25**, 062103 (2018). <https://doi.org/10.1063/1.5027086>
- 2683 Y. Lecun, L. Bottou, Y. Bengio, P. Haffner, in Proceedings of the IEEE, 86(11), 2278–
2684 2324 (1998). <https://doi.org/10.1109/5.726791>
- 2685 Q. Lenouvel, V. Génot, P. Garnier, et al., Earth and Space Science, **8**, e2020EA001530
2686 (2021). <https://doi.org/10.1029/2020EA001530>
- 2687 Q. Lenouvel, Identification by machine learning and analysis of electron diffusion regions
2688 at the Earth's magnetopause observed by MMS, PhD thesis (2022).
<https://theses.hal.science/tel-04075287v1>
- 2690 T.C. Li, Y.-H. Liu, M. Hesse, Y. Zou, J. Geophys. Res., **125**, e2019JA027094 (2020).
2691 <https://doi.org/10.1029/2019JA027094>

- 2692 T.C. Li, Y.-H. Liu, Y. Qi, *Astrophysical Journal Letters*, **909**, L28 (2021).
<https://doi.org/10.3847/2041-8213/abea0b>
- 2693 T.C. Li, Y.-H. Liu, Y. Qi, M. Zhou, *Phys. Rev. Lett.*, **131**, 085201 (2023).
<https://doi.org/10.1103/PhysRevLett.131.085201>
- 2694 H. Liang, P.A. Cassak, S. Servidio, et al., *Physics of Plasmas*, **26**, 082903 (2019).
<https://doi.org/10.1063/1.5098888>
- 2695 H. Liang, M.H. Barbhuiya, P.A. Cassak, O. Pezzi, S. Servidio, F. Valentini, G.P. Zank, *Journal of Plasma Physics*, **86**, 825860502 (2020).
<https://doi.org/10.1017/S0022377820001270>
- 2696 M. Lindberg, A. Vaivads, S. Raptis, P.-A. Lindqvist, B.L. Giles, D.J. Gershman, *Entropy*, **24**, 745 (2022). <https://doi.org/10.3390/e24060745>
- 2697 P.-A. Lindqvist, G. Olsson, R.B. Torbert, et al., *Space Science Reviews*, **199**(1-4), 137–165 (2016). <https://doi.org/10.1007/s11214-014-0116-9>
- 2698 Y.-H. Liu, M. Hesse, *Phys. Plasmas*, **23**, 060704 (2016).
<https://doi.org/10.1063/1.4954818>
- 2699 Y.-H. Liu, M. Hesse, F. Guo, W. Daughton, H. Li, P.A. Cassak, M.A. Shay, *Physical Review Letters*, **118**(8), 085101 (2017).
<https://doi.org/10.1103/PhysRevLett.118.085101>
- 2700 Y.-H. Liu, M. Hesse, F. Guo, H. Li, and T. K. M. Nakamura, *Physics of Plasmas*, **25**, 080701 (2018a). <https://doi.org/10.1063/1.5042539>
- 2701 Y.-H. Liu, M. Hesse, T.C. Li, M. Kuznetsova, A. Le, *J. Geophys. Res.*, **123**, 4908 (2018b). <https://doi.org/10.1029/2018JA025410>
- 2702 Y.-H. Liu, T.C. Li, M. Hesse, W.J. Sun, J. Liu, J.L. Burch, J.A. Slavin, K. Huang, *J. Geophys. Res.*, **124**, 2819 (2019). <https://doi.org/10.1029/2019JA026539>
- 2703 J.G. Lyon, J.A. Fedder, C.M. Mobarry, *J. Atmos. Sol. Terr. Phys.*, **66**, 1333–1350 (2004).
<https://doi.org/10.1016/j.jastp.2004.03.020>
- 2704 A.T. Marshall, J.L. Burch, P.H. Reiff, J.M. Webster, R.B. Torbert, R.E. Ergun, et al., *J. Geophys. Res.: Space Physics*, **125**, e2019JA027296 (2020).
<https://doi.org/10.1029/2019JA027296>
- 2705 A.T. Marshall, J.L. Burch, P.H. Reiff, et al., *Physics of Plasmas*, **29**, 012905 (2022).
<https://doi.org/10.1063/5.0071159>
- 2706 D. Maturana, S. Scherer, in *IEEE/RSJ International Conference on Intelligent Robots and Systems (IROS)*, 922–928 (2015).
<https://doi.org/10.1109/IROS.2015.7353481>
- 2707 D.J. McComas, M. A. Dayeh, H. O. Funsten, et al., *J. Geophys. Res.*, **116**, A02211 (2011).
doi:10.1029/2010JA016138, 2011

- 2727 R.L. McPherron, C.T. Russell, M.P. Aubry, J. Geophys. Res., **78**(16), 3131-3149 (1973).
2728 <https://doi.org/10.1029/JA078i016p03131>
- 2729 B. Michotte de Welle, N. Aunai, G. Nguyen, B. Lavraud, V. Génot, A. Jeandet, R. Smets,
2730 Journal of Geophysical Research: Space Physics, **127**, e2022JA030996
2731 (2022). <https://doi.org/10.1029/2022JA030996>
- 2732 D. Moseev, M. Salewski, Physics of Plasmas, **26**, 020901 (2019).
2733 <https://doi.org/10.1063/1.5085429>
- 2734 C. Mouhot, C. Villani, Acta Math., **207**, 29–201 (2011). <https://doi.org/10.1007/s11511-011-0068-9>
- 2735 T. Nagai, I. Shinohara, M. Fujimoto, A. Matsuoka, Y. Saito, T. Mukai, J. Geophys. Res.,
2736 **116**, A04222 (2011), <https://doi.org/10.1029/2010JA016283>
- 2737 T. Nagai, S. Zenitani, I. Shinohara, R. Nakamura, M. Fujimoto, Y. Saito, T. Mukai, Journal
2738 of Geophysical Research: Space Physics, **118**, 7703–7713 (2013).
2739 <https://doi.org/10.1002/2013JA019135>
- 2740 R. Nakamura, T. Nagai, J. Birn, V.A. Sergeev, O. Le Contel, V. Varsani, A., et al., Earth
2741 Planets Space, **69**(1), 129 (2017). <https://doi.org/10.1186/s40623-017-0707-2>
- 2742 T.K.M. Nakamura, R. Nakamura, A. Varsani, K.J. Genestreti, W. Baumjohann, and Y.-
2743 H. Liu, Geophysical Research Letters, **45**, 3829–3837 (2018a).
2744 <https://doi.org/10.1029/2018GL078340>
- 2745 T.K.M. Nakamura, K.J. Genestreti, Y.-H. Liu, et al., Journal of Geophysical Research:
2746 Space Physics, **123**, 9150–9168 (2018b). <https://doi.org/10.1029/2018JA025713>
- 2747 Y. Narita, Nonlin. Processes Geophys., **24**, 203–214 (2017). <https://doi.org/10.5194/npg-24-203-2017>
- 2748 J. Ng, J. Egedal, A. Le, W. Daughton, L.-J. Chen, Phys. Rev. Lett., **106**, 065002 (2011).
2749 <https://doi.org/10.1103/PhysRevLett.106.065002>
- 2750 J. Ng, L.-J. Chen, N. Bessho, J. Shuster, B. Burkholder, J. Yoo, Geophys. Res. Lett., **49**,
2751 e2022GL099544 (2022). <https://doi.org/10.1029/2022GL099544>
- 2752 G. Nguyen, N. Aunai, B. Michotte de Welle, A. Jeandet, B. Lavraud, D. Fontaine, Journal
2753 of Geophysical Research: Space Physics, **127**, e2021JA029773 (2022a).
2754 <https://doi.org/10.1029/2021JA029773>
- 2755 G. Nguyen, N. Aunai, B. Michotte de Welle, A. Jeandet, B. Lavraud, D. Fontaine, Journal
2756 of Geophysical Research: Space Physics, **127**, e2021JA029774 (2022b).
2757 <https://doi.org/10.1029/2021JA029774>
- 2758 G. Nguyen, N. Aunai, B. Michotte de Welle, A. Jeandet, B. Lavraud, D. Fontaine, Journal
2759 of Geophysical Research: Space Physics, **127**, e2021JA030112 (2022c).
2760 <https://doi.org/10.1029/2021JA030112>

- 2763 G. Nguyen, N. Aunai, B. Michotte de Welle, A. Jeandet, B. Lavraud, D. Fontaine, Journal
2764 of Geophysical Research: Space Physics, **127**, e2021JA029776 (2022d).
2765 <https://doi.org/10.1029/2021JA029776>
- 2766 D.R. Nicholson, Introduction to Plasma Theory. New York: Wiley (1983).
- 2767 M. Oka, T.-D. Phan, M. Øieroset, V. Angelopoulos, Journal of Geophysical Research:
2768 Space Physics, **121**, 1955–1968 (2016). <https://doi.org/10.1002/2015JA022040>
- 2769 M. Oka, J. Birn, J. Egedal, et al., Space Sci. Rev., **219**, 75 (2023).
2770 <https://doi.org/10.1007/s11214-023-01011-8>
- 2771 V. Olshevsky, D.I. Pontin, B. Williams, et al., Astron. Astrophys., **644**, A150 (2020).
2772 <https://doi.org/10.1051/0004-6361/202039182>
- 2773 V. Olshevsky, Y.V. Khotyaintsev, A. Lalti, et al., Journal of Geophysical Research: Space
2774 Physics, **126**, e2021JA029620 (2021). <https://doi.org/10.1029/2021JA029620>
- 2775 T.G. Onsager, M.F. Thomsen, J.T. Gosling, S.J. Bame, Geophysical Research Letters,
2776 **17**(11), 1837–1840 (1990). <https://doi.org/10.1029/GL017i011p01837>
- 2777 T.G. Onsager, M.F. Thomsen, R.C. Elphic, J.T. Gosling, Journal of Geophysical Research,
2778 **96**, 20999-21011 (1991). <https://doi.org/10.1029/91JA01983>
- 2779 G. Paschmann, P.W. Daly, Analysis methods for multi-spacecraft data. ISSI Scientific
2780 Report SR-001, ESA Publ. Div., Noordwijk, Netherlands (1998)
- 2781 G. Paschmann, P.W. Daly, Multi-Spacecraft Analysis Methods Revisited. ISSI Scientific
2782 Report SR-008, ESA Publ. Div., Noordwijk, Netherlands (2008)
- 2783 G. Paschmann, B.U.Ö. Sonnerup, in *Multi-Spacecraft Analysis Methods Revisited*, edited
2784 by G. Paschmann and P.W. Daly, ISSI SR-008, pp.65-74, ESA Publ. Div. (2008)
- 2785 G. Paschmann, S. Schwartz, C.P. Escoubet, S. Haaland, Outer magnetospheric
2786 boundaries: Cluster results, Space Sciences Series of ISSI, **20**, Springer (2005).
- 2787 G. Paschmann, M. Øieroset, T.D. Phan, Space Sci. Rev., **47**, 309-341 (2013).
2788 https://doi.org/10.1007/978-1-4899-7413-6_12
- 2789 D.S. Payne, C.J. Farrugia, R.B. Torbert, K. Germaschewski, A.R. Rogers, M.R. Argall,
2790 Phys. Plasmas, **28**, 112901 (2021). <https://doi.org/10.1063/5.0068317>
- 2791 T.D. Phan, C.P. Escoubet, L. Rezeau, et al., Space Sci. Rev., **118**, 367-424 (2005).
2792 <https://doi.org/10.1007/s11214-005-3836-z>
- 2793 T.D. Phan, H. Hasegawa, M. Fujimoto, M. Øieroset, T. Mukai, R.P. Lin, W. Paterson,
2794 Geophysical Research Letters, **33**, L09104 (2006).
2795 <https://doi.org/10.1029/2006GL025756>
- 2796 T.D. Phan, M.A. Shay, J.P. Eastwood, V. Angelopoulos, M. Øieroset, M. Oka, M.
2797 Fujimoto, Space Science Reviews, **199**, 631–650 (2015).
2798 <https://doi.org/10.1007/s11214-015-0150-2>

- 2799 T.D. Phan, J.P. Eastwood, P.A. Cassak, et al., Geophysical Research Letters, **43**(12),
2800 6060–6069 (2016). <https://doi.org/10.1002/2016GL069212>
- 2801 T.D. Phan, J.P. Eastwood, M.A. Shay, et al., Nature, **557**, 202-206 (2018).
2802 <https://doi.org/10.1038/s41586-018-0091-5>
- 2803 C. Pollock, T.E. Moore, A. Jacques, et al., Space Science Reviews, **199**(1-4), 331–406
2804 (2016). <https://doi.org/10.1007/s11214-016-0245-4>
- 2805 D.I. Pontin, E.R. Priest, Living Rev. Sol. Phys., **19**, 1 (2022).
2806 <https://doi.org/10.1007/s41116-022-00032-9>
- 2807 L. Price, M. Swisdak, J.F. Drake, P.A. Cassak, J.T. Dahlin, and R.E. Ergun, Geophys.
2808 Res. Lett. **43**, 6020–6027 (2016). <https://doi.org/10.1002/2016GL069578>
- 2809 L. Price, M. Swisdak, J.F. Drake, and D.B. Graham, Journal of Geophysical Research:
2810 Space Physics, **125**(4) (2020). <https://doi.org/10.1029/2019JA027498>
- 2811 P.L. Pritchett, J. Geophys. Res., **106**, 3783-3798 (2001).
2812 <https://doi.org/10.1029/1999JA001006>
- 2813 Y. Qi, T.C. Li, C.T. Russell, R.E. Ergun, Y.-D. Jia, M. Hubbert, Astrophysical Journal
2814 Letters, **926**, L34 (2022). <https://doi.org/10.3847/2041-8213/ac5181>
- 2815 J. Raeder, W.D. Cramer, K. Germaschewski, J. Jensen, Space Science Reviews, **206**, 601-
2816 620 (2017). <https://doi.org/10.1007/s11214-016-0304-x>
- 2817 A.C. Rager, J.C. Dorelli, D.J. Gershman, et al., Geophysical Research Letters, **45**, 578–
2818 584 (2018). <https://doi.org/10.1002/2017GL076260>
- 2819 P.H. Reiff, T.W. Hill, J.L. Burch, Journal of Geophysical Research, **82**, 479–491 (1977).
2820 doi:[10.1029/JA082i004p00479](https://doi.org/10.1029/JA082i004p00479)
- 2821 P.H. Reiff, A.G. Daou, S.Y. Sazykin et al., Geophys. Res. Lett., **43**, 7311–7318 (2016).
2822 <https://doi.org/10.1002/2016GL069154>
- 2823 P.H. Reiff, J.M. Webster, A.G. Daou, et al., CCMC Modeling of Magnetic Reconnection
2824 in Electron Diffusion Regions. in *Space Weather of the Heliosphere: Processes and*
2825 *Forecasts*, Proceedings IAU Symposium No. 335, p. 142-146, Eds. C. Foullon and O.
2826 Malandraki (2017). <https://doi.org/10.1017/S1743921317010845>
- 2827 P.H. Reiff, A. Marshall, J. Webster, S. Sazykin, C.T. Russell, L. Rastaetter, MMS
2828 observations and CCMC modeling of field line stretching at separator lines. Fall AGU
2829 e-Lightning poster (2018). <https://agu2018fallmeeting.agu.ipostersessions.com/default.aspx?s=B2-10-20-70-BD-2D-A2-4E-35-27-A4-FE-DC-C0-6D-DA>, doi: 10.1002/essoar.10502075.1
- 2832 P.I. Reyes, V.A. Pinto, P. S. Moya, Space Weather, **19**(9), e2021SW002766 (2021).
2833 <https://doi.org/10.1029/2021SW002766>

- 2834 L. Rezeau, G. Belmont, R. Manuzzo, N. Aunai, J. Dargent, J. Geophys. Res. Space Phys.
2835 **123**(1), 227–241 (2018). <https://doi.org/10.1002/2017ja024526>
- 2836 C.T. Russell, B.J. Anderson, W. Baumjohann, et al., Space Science Reviews, **199**(1-4),
2837 189–256 (2016). <https://doi.org/10.1007/s11214-014-0057-3>
- 2838 H. Rosenbauer, H. Grünwaldt, M.D. Montgomery, G. Paschmann, N. Sckopke, Journal
2839 of Geophysical Research, **80**, 2723-2737 (1975). doi:[10.1029/JA080i019p02723](https://doi.org/10.1029/JA080i019p02723)
- 2840 D. Rumelhart, G. Hinton, R. Williams, Nature, **323**, 533-536 (1986).
2841 <https://doi.org/10.1038/323533a0>
- 2842 J. Safrankova, Z. Nemecek, S. Dusik, L. Prech, D.G. Sibeck, N.N. Borodkova, Annales
2843 Geophysicae, **20**, 301-309 (2002). <https://doi.org/10.5194/angeo-20-301-2002>
- 2844 H. Schlichting, Boundary Layer Theory, McGraw-Hill, p.817 (1979).
- 2845 J.M. Schroeder, J. Egedal, G. Cozzani, Y.V. Khotyaintsev, W. Daughton, R.E. Denton,
2846 J.L. Burch, Geophysical Research Letters, **49**, e2022GL100384 (2022).
2847 <https://doi.org/10.1029/2022GL100384>
- 2848 J. Scudder, W. Daughton, J. Geophys. Res., **113**, A06222 (2008).
2849 <https://doi.org/10.1029/2008JA013035>
- 2850 J. Scudder, W. Daughton, Journal of Geophysical Research: Space Physics, **113**, 1–16
2851 (2008). <https://doi.org/10.1029/2008JA013035>
- 2852 J.D. Scudder, R.D. Holdaway, W.S. Daughton, H. Karimabadi, V. Roytershteyn, C.T.
2853 Russell, J.Y. Lopez, Physical Review Letters, **108**, 225005 (2012).
2854 <https://doi.org/10.1103/PhysRevLett.108.225005>
- 2855 V. Sergeev, V. Angelopoulos, M. Kubyshkina, et al., Journal of Geophysical Research:
2856 Space Physics, **116**, A00I26 (2011). <https://doi.org/10.1029/2010JA015689>
- 2857 S. Servidio, A. Chasapis, W.H. Matthaeus, et al., Phys. Rev. Lett., **119**, 205101 (2017).
2858 <https://doi.org/10.1103/PhysRevLett.119.205101>
- 2859 A. Settino, Y.V. Khotyaintsev, D.B. Graham, D. Perrone, F. Valentini, Journal of
2860 Geophysical Research: Space Physics, **127**, e2021JA029758 (2022).
2861 <https://doi.org/10.1029/2021JA029758>
- 2862 M.A. Shay, J.F. Drake, M. Swisdak, Phys. Rev. Lett., **99**, 155002 (2007).
2863 <https://doi.org/10.1103/PhysRevLett.99.155002>
- 2864 E.G. Shelley, A.G. Ghielmetti, H. Balsiger, et al., Space Sci. Rev., **71**, 497–530 (1995).
2865 <https://doi.org/10.1007/BF00751339>
- 2866 C. Shen, X. Li, M. Dunlop, Q.Q. Shi, Z.X. Liu, E. Lucek, Z.Q. Chen, J. Geophys. Res.,
2867 **112**, A06211 (2007). <https://doi.org/10.1029/2005JA011584>
- 2868 Q.Q. Shi, C. Shen, Z.Y. Pu, et al., Geophys. Res. Lett., **32**, L12105 (2005).
2869 <https://doi.org/10.1029/2005GL022454>

- 2870 Q.Q. Shi, C. Shen, M.W. Dunlop, et al., Geophys. Res. Lett. **33**, L08109 (2006).
2871 <https://doi.org/10.1029/2005GL025073>
- 2872 Q.Q. Shi, A.M. Tian, S.C. Bai, et al., Space Science Reviews, **215**(4), 35 (2019).
2873 <https://doi.org/10.1007/s11214-019-0601-2>
- 2874 J.R. Shuster, L.-J. Chen, W. Daughton, et al., Geophysical Research Letters, **41**, 5389–
2875 5395 (2014). <https://doi.org/10.1002/2014GL060608>
- 2876 J.R. Shuster, L.-J. Chen, M. Hesse, M.R. Argall, W. Daughton, R.B. Torbert, N. Bessho,
2877 Geophysical Research Letters, **42**, 2586–2593 (2015).
2878 <https://doi.org/10.1002/2015GL063601>
- 2879 J.R. Shuster, M.R. Argall, R.B. Torbert, et al., Geophysical Research Letters, **44**, 1625–
2880 1633 (2017). <https://doi.org/10.1002/2017GL072570>
- 2881 J.R. Shuster, D.J. Gershman, L.-J. Chen, et al., Geophysical Research Letters, **46**, 7862–
2882 7872 (2019). <https://doi.org/10.1029/2019GL083549>
- 2883 J.R. Shuster, D.J. Gershman, J.C. Dorelli, et al., Nat. Phys. **17**, 1056–1065 (2021a).
2884 <https://doi.org/10.1038/s41567-021-01280-6>
- 2885 J.R. Shuster, N. Bessho, S. Wang, J. Ng, Phys. Plasmas, **28**, 122902 (2021b).
2886 <https://doi.org/10.1063/5.0069559>
- 2887 J.R. Shuster, D.J. Gershman, B.L. Giles, et al., Journal of Geophysical Research: Space
2888 Physics, **128**, e2022JA030949 (2023). <https://doi.org/10.1029/2022JA030949>
- 2889 D.G. Sibeck, R.E. Lopez, E.C. Roelof, Journal of Geophysical Research, **96**, 5489–5495
2890 (1991). doi:[10.1029/90JA02464](https://doi.org/10.1029/90JA02464)
- 2891 M.I. Sitnov, A.S. Sharma, K. Papadopoulos, D. Vassiliadis, Phys. Rev. E, **65**, 016116
2892 (2001). <https://doi.org/10.1103/PhysRevE.65.016116>
- 2893 M.I. Sitnov, N.A. Tsyganenko, A.Y. Ukhorskiy, P.C. Brandt, Journal of Geophysical
2894 Research: Space Physics, **113**(A7), A07218 (2008).
2895 <https://doi.org/10.1029/2007JA013003>
- 2896 M.I. Sitnov, G.K. Stephens, N.A. Tsyganenko, A.Y. Ukhorskiy, S. Wing, H. Korth, B.J.
2897 Anderson, Spatial structure and asymmetries of magnetospheric currents inferred from
2898 high-resolution empirical geomagnetic field models. In *Dawn-dusk asymmetries in*
2899 *planetary plasma environments*, edited by S. Haaland, A. Runov and C. Forsyth, p. 199–
2900 212, American Geophysical Union (AGU) (2017).
2901 <https://doi.org/10.1002/9781119216346.ch15>
- 2902 M.I. Sitnov, G.K. Stephens, N.A. Tsyganenko, et al., Journal of Geophysical Research:
2903 Space Physics, **124**(11), 8427–8456 (2019). <https://doi.org/10.1029/2019JA027037>
- 2904 M.I. Sitnov, G.K. Stephens, N.A. Tsyganenko, et al., Space Weather, **18**,
2905 e2020SW002561 (2020). <https://doi.org/10.1029/2020SW002561>

- 2906 M. Sitnov, G. Stephens, T. Motoba, M. Swisdak, Frontiers in Physics, **9** (2021).
2907 <https://doi.org/10.3389/fphy.2021.644884>
- 2908 B.U.Ö. Sonnerup, L.J. Cahill Jr., J. Geophys. Res., **72**(1), 171–183 (1967).
2909 doi:[10.1029/JZ072i001p00171](https://doi.org/10.1029/JZ072i001p00171)
- 2910 B.U.Ö. Sonnerup, M. Guo, Geophys. Res. Lett., **23**(25) 3679-3682 (1996)
- 2911 B.U.Ö. Sonnerup, M. Scheible, Minimum and maximum variance analysis. in *Analysis*
2912 *methods for multi-spacecraft data*, edited by G. Paschmann and P.W. Daly, ISSI. Sci.
2913 Rep. SR-001 (pp. 185–220). Noordwijk, Netherlands: ESA Publ. (1998)
- 2914 B.U.Ö. Sonnerup, W.-L. Teh, J. Geophys. Res., **113**(A5), A05202 (2008).
2915 <https://doi.org/10.1029/2007JA012718>
- 2916 B.U.Ö. Sonnerup, W.-L. Teh, J. Geophys. Res., **114**, A04206 (2009).
2917 <https://doi.org/10.1029/2008JA013897>
- 2918 B.U.Ö. Sonnerup, G. Paschmann, T.-D. Phan, Fluid aspects of reconnection at the
2919 magnetopause: In situ observations. in *Physics of the magnetopause*, Geophys. Monogr.
2920 Ser., vol. **90**, eds. P. Song, B.U.Ö. Sonnerup, and M.F. Thomsen, pp. 167-180, AGU,
2921 Washington, D. C. (1995)
- 2922 B.U.Ö. Sonnerup, S. Haaland, G. Paschmann, M.W. Dunlop, H. Rème, A. Balogh, J.
2923 Geophys. Res., **111**, A05203 (2006a). <https://doi.org/10.1029/2005JA011538>
- 2924 B.U.Ö. Sonnerup, H. Hasegawa, W.-L. Teh, L.-N. Hau, J. Geophys. Res. Space Physics,
2925 **111**, A09204 (2006b). <https://doi.org/10.1029/2006JA011717>
- 2926 B.U.Ö. Sonnerup, W.-L. Teh, H. Hasegawa, Grad-Shafranov and MHD reconstructions.
2927 in *Multi-spacecraft analysis methods revisited*, edited by G. Paschmann and P.W. Daly,
2928 ISSI SR-008, pp. 81-90, ESA Publications Division (2008)
- 2929 B.U.Ö. Sonnerup, H. Hasegawa, R.E. Denton, T.K.M. Nakamura, J. Geophys. Res. Space
2930 Physics, **121**(5), 4279–4290 (2016). <https://doi.org/10.1002/2016ja022430>
- 2931 J.C. Spall, Johns Hopkins APL Tech. Dig., **19**, 482–492 (1998).
- 2932 J.C. Spall, Introduction to Stochastic Search and Optimization: Estimation, Simulation,
2933 and Control. New York: John Wiley & Sons, 595 (2003).
- 2934 G.K. Stephens, M.I. Sitnov, Frontiers in Physics, **9**, 653111 (2021).
2935 <https://doi.org/10.3389/fphy.2021.653111>
- 2936 G.K. Stephens, M.I. Sitnov, H. Korth, N.A. Tsyganenko, S. Ohtani, M. Gkioulidou, A.Y.
2937 Ukhorskiy, Journal of Geophysical Research: Space Physics, **124**(2), 1085-1110 (2019).
2938 <https://doi.org/10.1029/2018JA025843>
- 2939 G.K. Stephens, S.T. Bingham, M.I. Sitnov, et al., Space Weather, **18**(12),
2940 e2020SW002583 (2020). <https://doi.org/10.1029/2020SW002583>

- 2941 G.K. Stephens, M.I. Sitnov, R.S. Weigel, et al., Journal of Geophysical Research: Space
2942 Physics, **128**, e2022JA031066 (2023). <https://doi.org/10.1029/2022JA031066>
- 2943 D.P. Stern, Reviews of Geophysics and Space Physics, **14**(2), 200 (1976).
2944 <https://doi.org/10.1029/RG014i002p00199>
- 2945 I. Svenningsson, E. Yodradnova, Y.V. Khotyaintsev, M. André, G. Cozzani, EGU
2946 General Assembly 2023, EGU23-8664 (2023). <https://doi.org/10.5194/egusphere-egu23-8664>
- 2947 M. Swisdak, Geophys. Res. Lett., **43**, 43-49 (2016).
2948 <https://doi.org/10.1002/2015GL066980>
- 2950 B.-B. Tang, W.Y. Li, D.B. Graham, et al., Geophysical Research Letters, **46**, 3024-3032
2951 (2019). <https://doi.org/10.1029/2019GL082231>
- 2952 X. Tang, C. Cattell, J. Dombeck, et al., Geophysical Research Letters, **40**, 2884–2890
2953 (2013). <https://doi.org/10.1002/grl.50565>
- 2954 W.-L. Teh, Journal of Geophysical Research: Space Physics, **124**, 1644–1650 (2019).
2955 <https://doi.org/10.1029/2018JA026416>
- 2956 W.-L. Teh, S. Zenitani, Earth and Space Science, **7**, e2020EA001449 (2020).
2957 <https://doi.org/10.1029/2020EA001449>
- 2958 T. Terasawa, H. Kawano, I. Shinohara, et al., J. Geomagn. Geoelectr., **48**(5–6), 603–614
2959 (1996)
- 2960 A.M. Tian, K. Xiao, A.W. Degeling, Q.Q. Shi, J.-S. Park, M. Nowada, T. Pitkanen,
2961 Astrophys. J., **889**, 35 (2020). <https://doi.org/10.3847/1538-4357/ab6296>
- 2962 S. Toledo-Redondo, M. André, Y.V. Khotyaintsev, et al., Geophysical Research Letters,
2963 **43**(13), 6759–6767 (2016). <https://doi.org/10.1002/2016gl069877>
- 2964 R.B. Torbert, C.T. Russell, W. Magnes, et al., Space Science Reviews, **199**(1-4), 105–
2965 135 (2016a). <https://doi.org/10.1007/s11214-014-0109-8>
- 2966 R.B. Torbert, H. Vaith, M. Granoff, et al., Space Sci. Rev., **199**, 285-305 (2016b).
2967 <https://doi.org/10.1007/s11214-015-0182-7>
- 2968 R.B. Torbert, J.L. Burch, M.R. Argall, et al., J. Geophys. Res.: Space Physics,
2969 **122**, 11901–11916 (2017). <https://doi.org/10.1002/2017JA024579>
- 2970 R.B. Torbert, J.L. Burch, T.D. Phan, et al., Science, **362**(6421), 1391–1395 (2018).
2971 <https://doi.org/10.1126/science.aat2998>
- 2972 R.B. Torbert, I. Dors, M.R. Argall, et al., Geophysical Research Letters, **47**,
2973 e2019GL085542 (2020). <https://doi.org/10.1029/2019GL085542>
- 2974 G. Tóth, I.V. Sokolov, T. Gombosi, et al., J. Geophys. Res., **110**, A12226 (2005).
2975 doi:[10.1029/2005JA011126](https://doi.org/10.1029/2005JA011126)
- 2976 K.J. Trattner, S.A. Fuselier, S.M. Petrinec, T.K. Yeoman, C. Mouikis, H. Kucharek, H.

- 2977 Rème, Journal of Geophysical Research, **110**, A04207 (2005).
<https://doi.org/10.1029/2004JA010722>
- 2979 K.J. Trattner J.S. Mulcock, S.M. Petrinec, S.A. Fuselier, Journal of Geophysical Research, **112**, A08210 (2007). <https://doi.org/10.1029/2007JA012270>
- 2981 K.J. Trattner, S.M. Petrinec, S.A. Fuselier, N. Omidi, D.G. Sibeck, Journal of Geophysical Research, **117**, A01213 (2012). <https://doi.org/10.1029/2011JA017080>
- 2983 K.J. Trattner, J.L. Burch, R.E. Ergun, et al., Journal of Geophysical Research, **122**, 11991– 12005 (2017). <https://doi.org/10.1002/2017JA024488>
- 2985 K.J. Trattner, J.L. Burch, R.E. Ergun, et al., Journal of Geophysical Research, Space Physics, **123**, 10177– 10188 (2018). <https://doi.org/10.1029/2018JA026081>
- 2987 K.J. Trattner, S.M. Petrinec, S.A. Fuselier, Space Science Review, **217**, 41 (2021).
<https://doi.org/10.1007/s11214-021-00817-8>
- 2989 L. Trenchi, M.F. Marcucci, G. Pallocchia, et al., Journal of Geophysical Research, **113**, A07S10 (2008). <https://doi.org/10.1029/2007JA012774>
- 2991 L. Trenchi, M.F. Marcucci, G. Pallocchia, et al., Mem. Soc. Astron. Ital., **80**, 287 (2009)
- 2992 N. A. Tsyganenko, Journal of Geophysical Research, **100**, 5599-5612 (1995)
- 2993 N. Tsyganenko, Planetary and Space Science, **39**(4), 641–654 (1991).
[http://dx.doi.org/10.1016/0032-0633\(91\)90058-I](http://dx.doi.org/10.1016/0032-0633(91)90058-I)
- 2995 N.A. Tsyganenko, M.I. Sitnov, Journal of Geophysical Research: Space Physics, **110**, A03208 (2005). <https://doi.org/10.1029/2004JA010798>
- 2997 N.A. Tsyganenko, M.I. Sitnov, Journal of Geophysical Research: Space Physics, **112**, A06225 (2007). <https://doi.org/10.1029/2007JA012260>
- 2999 N.A. Tsyganenko, V.A. Andreeva, Journal of Geophysical Research: Space Physics, **121**, 10,786–10,802 (2016). <https://doi.org/10.1002/2016JA023217>
- 3001 A. Varsani, R. Nakamura, V.A. Sergeev, et al., Journal of Geophysical Research: Space Physics, **122**, 10891–10909 (2017). <https://doi.org/10.1002/2017JA024547>
- 3003 V.M. Vasiliunas, Rev. Geophys., **13**, 303-336 (1975).
<https://doi.org/10.1029/RG013i001p00303>
- 3005 J.M. Webster, J.L. Burch, P.H. Reiff, et al., Journal of Geophysical Research: Space Physics, **123**(6), 4858–4878 (2018). <https://doi.org/10.1029/2018JA025245>
- 3007 S. Wellenzohn, R Nakamura, T.K.M. Nakamura, et al., Journal of Geophysical Research: Space Physics, **126**, e2020JA028917 (2021). <https://doi.org/10.1029/2020JA028917>
- 3009 D. Wettschereck, D.W. Aha, T. Mohri, Artificial Intelligence Review, **11**(1), 273-314 (1997). <https://doi.org/10.1023/A:1006593614256>
- 3011 F.D. Wilder, R.E. Ergun, J.L. Burch, et al., Journal of Geophysical Research: Space Physics, **123**, 6533-6547 (2018). <https://doi.org/10.1029/2018JA025529>

- 3013 Y. Yang, W.H. Matthaeus, T.N. Parashar, et al., Phys. Rev. E, **95**, 061201(R) (2017).
3014 <https://doi.org/10.1103/PhysRevE.95.061201>
- 3015 S. Zenitani, M. Hesse, A. Klimas, M. Kuznetsova, Phys. Rev. Lett., **106**, 195003 (2011).
3016 <https://doi.org/10.1103/PhysRevLett.106.195003>
- 3017 S. Zenitani, M. Hesse, A. Klimas, C. Black, M. Kuznetsova, Phys. Plasmas, **18**, 122108
3018 (2011). <https://doi.org/10.1063/1.3662430>
- 3019 S. Zenitani, I. Shinohara, T. Nagai, Geophys. Res. Lett., **39**, L11102 (2012).
3020 <https://doi.org/10.1029/2012GL051938>
- 3021 X. Zhu, J.C. Spall, Int. J. Adapt. Control. Signal. Process., **16**, 397–409 (2002).
3022 doi:10.1002/acs.715
- 3023 X. Zhu, I.J. Cohen, B.H. Mauk, R. Nikoukar, D.L. Turner, R.B. Torbert, Front. Astron.
3024 Space Sci., **9**, 878403 (2022). doi:10.3389/fspas.2022.878403
- 3025

1 **Appendix B Tables Summarizing Methods Reviewed in the Paper**

2

3 **Table 1** Methods for region and current sheet identification

Method	# of spacecraft (SC) needed	Underlying theory, concept, or name of machine learning method	Input	Output	Assumptions	Spatial or temporal scale of interest	Other requirements if any	References
ML-based region identification ¹	1	Gradient boosting/machine learning	\mathbf{B} , ion moments (n , \mathbf{u}_i , T_i)	Near-Earth region	None	MHD ² and larger	N/A	Nguyen et al. (2022a)
Region classification using 3D particle distributions	1	Convolutional Neural Network/supervised machine learning	3D velocity distributions	Near-Earth region	None	MHD and larger	N/A	Olshevsky et al. (2021)

4 ¹The code is available at github (https://github.com/gautiernguyen/in-situ_Events_lists).

5

6 ²Magnetohydrodynamics

7 **Table 2** Methods for large-scale context

Method	# of spacecraft (SC) needed	Underlying theory, concept, or name of data mining method	Input	Output	Assumptions	Spatial or temporal scale of interest	Other requirements if any	References
--------	-----------------------------	-----------------------------------------------------------	-------	--------	-------------	---------------------------------------	---------------------------	------------

Maximum magnetic shear model	1-SC solar wind	in Time-of-flight analysis	ion moments (n , \mathbf{u}_i), \mathbf{B} in solar wind	Magnetopause plot; dayside reconnection location	Entire magnetopause	T96 & IMF draping models	Trattner et al. (2007); Kobel and Flückiger (1994); Tsyganenko (1995)
Global MHD model ¹	1-SC solar wind	in MHD equations	MHD parameters in solar wind	MHD quantities everywhere in space and time	MHD	MHD	Tóth et al. (2005); see the CCMC website ¹ for other codes
Data mining (DM) reconstruction ₂	Multi-mission	DM using distance weighted kNN method and basis function magnetic field architectures	Magnetometer archives; Solar wind $u_{sw}B_z$; geomagnetic indices SML, SMR & their time derivatives	3D magnetic field parametrized by $\sim 10^3$ parameters derived from data	Magnetostatic	$>1 R_E$ and >5 min	Global activity indices availability
Global in situ data reconstruction	Multi-mission	kNN statistical method	Solar wind parameters	3D global SW propagation from outer magnetopause and bow shock models	Dayside L1, magnetotail here, magnetotop		Michotte et Welle et al. (2022)

8 ¹The code can be run at CCMC (<https://ccmc.gsfc.nasa.gov/>).

9 ² u_{sw} : solar wind speed; B_z : north-south component of the interplanetary magnetic field in geocentric solar magnetospheric (GSM) coordinates

10

11 **Table 3** Methods for coordinate systems, frame velocity, and spacecraft trajectory estimation

Method	# of spacecraft (SC) needed	Underlying theory, concept	Input	Output	Assumptions	Spatial or temporal scale of interest	References
MVAB	1	$\nabla \cdot \mathbf{B} = 0$	\mathbf{B}	Variance directions; normal direction; LMN coordinates	1D structure to get a good estimate for the normal (\mathbf{e}_N) direction	N/A	Sonnerup and Scheible (1998)
MVAve	1	None	\mathbf{u}_e	Variance directions	Presence of electron outflow jets	Sub-ion scale	Genestreti et al. (2018)
MDDB	4	None	\mathbf{B} , SC position	Gradient directions; LMN coordinates	Steady structure	>SC separation	Shi et al. (2019)
Dimensionality	4	MDDB	MDDB eigenvalues	Dimensionality indices	Steady structure	>SC separation	Rezeau et al. (2018)
Hybrid method	4	MDDB + MVAB	\mathbf{B} , SC	LMN coordinates	Large maximum	>SC separation	Denton et al. (2018);

		or MVAve \mathbf{u}_e)	position (and \mathbf{u}_e)	eigenvalues	Heuer et al. (2022)
HT analysis	1	$\partial \mathbf{B} / \partial t = 0$	\mathbf{B}, \mathbf{u} (or \mathbf{E}) velocity	Not in diffusion regions	deHoffmann and Teller (1950); Khrabrov and Sonnerup (1998)
MFR	1	Faraday's law, $\partial \mathbf{B} / \partial t = 0$	\mathbf{E} (or \mathbf{u}), \mathbf{B} Normal direction and velocity	1D structure, $d/dt = 0$, constant velocity	>SC separation Dunlop and Woodward (1998)
4SC timing	4	None	Various and velocity	1D structure, $d/dt = 0$, constant velocity	>SC separation Dunlop and Woodward (1998)
STD	4	\mathbf{B} changes from convection	$\mathbf{B}(t)$, SC position	Partial time derivative=0	>SC separation Shi et al. (2006, 2019)
Reconstructed X-line motion	4	$\nabla \cdot \mathbf{B} = 0$; Ampère's law	\mathbf{B} , \mathbf{j} , SC position	Various depending on model	Spacecraft spacing Denton et al. (2021)
Comparison with simulation	1 or more	PIC code applicable	Various simulation domain	Simulation through realistic	Simulation scale Shuster et al. (2017); Schroeder et al. (2022)
MCA	4	None	\mathbf{B} , SC position	Steady structure	>SC separation Fadanelli et al. (2019)

Table 4 Methods for reconstructing 2D/3D structures

Method	# of spacecraft (SC) needed	Underlying theory, concept	Input	Output	Assumptions	Spatial or temporal scale of interest	Other requirements if any	References
3D B-field quadratic reconstruction	4	Maxwell equations	\mathbf{B}, \mathbf{j} at 4 SC locations	Full 3D vector B-field near tetrahedron	No quadratic terms in minimum variance direction	Spacecraft spacing		Torbert et al. (2020)
3D polynomial reconstruction ¹	4	$\nabla \cdot \mathbf{B} = 0$; Ampère's law	\mathbf{B}, \mathbf{j} at 4 SC locations	Full 3D vector B-field near tetrahedron	Various depending on model	Spacecraft spacing		Denton et al. (2020)
3D Polynomial Reconstruction with multiple input times ²	4	$\nabla \cdot \mathbf{B} = 0$; Ampère's law	\mathbf{B}, \mathbf{j} at 4 SC locations	Full 3D vector B-field near tetrahedron	Various depending on model	Spacecraft spacing		Denton et al. (2022)
3D empirical reconstruction using stochastic optimization method	4	Simultaneous perturbation stochastic approximation	\mathbf{B}, \mathbf{j} at 4 SC locations	Full 3D vector B-field near tetrahedron	$\nabla \cdot \mathbf{B} = 0$; Ampère's law	Spacecraft spacing		Zhu et al. (2022)
Simulation-assisted 2D reconstruction of SC	Multi-SC	Comparison with kinetic	Various	2D fields of all fluid quantities	Simulation is realistic	Ion skin depth		Schroeder et al. (2022)

an EDR		simulation						
Grad-Shafranov reconstruction	1	Static magnetic field, $\nabla \cdot \mathbf{B} = 0$, Ampère's law	\mathbf{B} , pressure	2D maps of \mathbf{B} & pressure	2D, equilibrium	MHD scale	Predefin ed structure velocity	Sonnerup et al. (2006)
MHD reconstruction	1	MHD equations	MHD parameters (occasionally incl. P -anisotropy)	2D maps of MHD quantities depending on model	2D, steady structure; various scale	MHD	Predefin ed structure velocity	Sonnerup et al. (2006); Chen and Hau (2018); Teh (2019); Tian et al. (2020)
EMHD reconstruction ³	1	EMHD equations	\mathbf{B} , \mathbf{E} , electron moments (n , \mathbf{u}_e , T_e)	2D maps of B, E, electron and moments	2D, steady structure; various scale	Electron	Predefin ed structure velocity	Sonnerup et al. (2016); Hasegawa et al. (2021); Korovinskiy et al. (2021, 2023)
3D RBF-based reconstruction	Multi-SC	Euler potentials expressed by modified radial basis functions	\mathbf{B}	Full 3D vector B-field near tetrahedron	Steady structure; $\nabla \cdot \mathbf{B} = 0$	Spacecraft spacing		Chen et al. (2019)

¹The code is available at Zenodo (<https://doi.org/10.5281/zenodo.3906853>).

²The code is available at Zenodo (<https://doi.org/10.5281/zenodo.6395044>).

³The code is available at Zenodo (<https://doi.org/10.5281/zenodo.514478>).

Table 5 Methods for diffusion region identification

Method	# of spacecr aft (SC) needed	Underlying concept, or name of machine learning method	Input	Output	Assumption	Spatial scale of interest	Other requirements if any	References
Electron-frame dissipation measure ¹	1	$\mathbf{j} \cdot (\mathbf{E} + \mathbf{u}_e \times \mathbf{B}) - \rho_c (\mathbf{u}_e \cdot \mathbf{E})$	$\mathbf{j}, \mathbf{E}, \mathbf{B}, \mathbf{u}_e [\rho_c]$	Scalar in units of $[\text{W/m}^3]$	Maxwell's equations			Zenitani et al. (2011)
Agyrotropy	1	Particle distribution function	$\mathbf{P}, \hat{\mathbf{b}}$	Scalar	None	Diffusion region		Swisdak (2016)
Pressure strain	4	$-(\mathbf{P} \cdot \nabla) \cdot \mathbf{u}$	\mathbf{P}, \mathbf{u}	Ion and electron dissipation rate in scalar	Differentiable velocity; curlometer			Yang et al. (2017); Bandyopadhyay et al. (2021)
Electron vorticity	4	$\Omega_e \sim \omega_{ce}$ (electron gyrofrequency) defines the characteristic frequency of the EDR	\mathbf{v}_e	Electron vorticity ($\boldsymbol{\Omega}_e = \nabla \times \mathbf{u}_e$)	None	EDR		Hwang et al. (2019)
Magnetic transport (MFT) ²	1 or 4	$\partial_t \psi + \mathbf{U}_\psi \cdot \nabla_\perp \psi = 0$ (Advection equation of magnetic flux)	$\mathbf{B}, \mathbf{E}, \mathbf{SC}$ position	MFT velocity (\mathbf{U}_ψ) or its divergence ($\nabla \cdot \mathbf{n}$)	Quasi-2D reconnectio	Diffusion region	Predefined LMN coordinates	Li et al. (2021); Qi et al. (2022)

		\mathbf{U}_ψ	k_\perp ; no magnetic field diffusion or generation	tes and frame velocity	
Machine learning 1 to classify regions	1	feed-forward multilayer perceptron	Plasma and 4 classes (IDR, EDR, boundary layers, magnetosphere)	IDR, EDR, boundary layers, magnetosphere	Lenouvel et al. (2021)
Machine learning 2 to identify EDRs	1	Convolutional Neural Network	Electron distribution functions	Diffusion regions	Lenouvel (2022)

¹ ρ_c : electric charge density

² k_M : wave number corresponding to the scale of the spatial variation in the direction of the reconnection X-line; k_\perp : wave number corresponding to the scale of the spatial variation in the plane transverse to the X-line

Table 6 Methods for analyzing the electron diffusion region

Method	# of spacecraft (SC)	Underlying theory, concept	Input	Output	Assumptions	Spatial temporal scale	or Other requirements if any	References

	needed				interest	
Anomalous transport terms estimation from lower hybrid waves ¹	4	Fluid equations, wave-particle interactions	\mathbf{B}, \mathbf{E} , particle moments (n , transport terms \mathbf{u}, \mathbf{P})	Anomalous transport terms	None Sub-ion scales	Particle moments that resolve the waves
Computing $\partial f_e / \partial t$ in the spacecraft frame	1	Electron Vlasov equation	Electron distribution function f_e at multiple times	$\partial f_e / \partial t$ (sometimes an approximation for $\partial f_e / \partial N$)	Cadence of electron measurements is sufficient for $\partial f_e / \partial t$ estimation	Consult with the FPI team for EDR proper implementation
Computing the spatial gradient $\mathbf{v} \cdot \nabla f_e$ term	4	Electron Vlasov equation	f_e , velocity-space coordinates for f_e , SC position	∇f_e and $\mathbf{v} \cdot \nabla f_e$	SC separation is sufficient for estimating ∇f_e	Consult with the FPI team for EDR proper implementation
Computing the $\mathbf{F} \cdot \nabla v f_e$ term in the spacecraft frame	1	Electron Vlasov equation	f_e , velocity-space coordinates for $f_e, \mathbf{E}, \mathbf{B}$	$\nabla_v f_e$ and each of the 3rd term of the Vlasov equation	Velocity-space resolution is sufficient for estimating $\nabla_v f_e$	Consult with the FPI team for EDR proper implementation
Non-	1	Particle	\mathbf{B} , particle	Scalar	non-None Kinetic scale	None Greco et al.

Maxwellianity ²	distribution function	distribution particle moments	Maxwellianity value	of particles of interest	(2012; Servidio et al. (2017); Graham et al. (2021))
Kinetic entropy	1	Boltzmann's entropy theory	Particle distribution, scalar densities, scalar non-Maxwellianity value	None	Kinetic scale of particles of interest

¹The scripts and data required to reproduce the figures in Graham et al. (2022) can be found at doi:10.5281/zenodo.6370048, and the routines require the irf-

24 matlab software package: <https://github.com/irfu/irfu-matlab>.

25 ²The routines to compute non-Maxwellianity can be found at <https://github.com/irfu/irfu-matlab>.

26 **Table 7** Methods for reconnection electric field (E_M) estimation

Method	# of spacecraft (SC) needed	Underlying theory or concept	Input	Output	Assumptions	Spatial temporal scale of interest	or	Other scale requirements if any	References
Direct measurement	1	Faraday's law	\mathbf{E}	E_M	2D, steady	N/A	Accurate LMN	Genestreti et al. (2018); Burch et al. (2020)	

Inflow velocity	1	$\mathbf{u}_e, n, \mathbf{B}$	Inflow velocity; normalized reconnectio n rate	2D, steady	EDR	Accurate LMN	Burch et al. (2020)
Multi-crescent VDF ¹	1	Equations of motion	$B_L, E_N, N,$ E_M u_{eM}	$B_L = bN, E_N = -kN,$ No guide field	Electron scale	$N=0$ crossing	Bessho et al. (2018)
Remote sensing at separatrix	More than 2	Magnetic flux conservation	Timing velocity at separatrix, \mathbf{E}, \mathbf{B}	2D, reconnection rate, uniform field between multi-probes	Ion to MHD scale	Separatrix identification	Nakamura et al. (2018a)
Separatrix angle	1 or 4 (depending on how separatrix is detected)	Flux and force balance along inflow and outflow direction	B_N, B_M (or B_z, B_x for tail)	Normalized reconnectio n rate	2-D, low beta, separatrix angle=exhaust opening angle	Electron to ion scale	Separatrix identification on Liu et al. (2017); Nakamura et al. (2018b)

¹ N : distance in the normal (N) direction from the current sheet center ($B_L=0$) plane; see section 4.3.1 for the definitions of b and k .